Modeling and Control of the Cooperative Automated Fiber Placement System

Xiaoming Zhang

A Thesis

In the Department

of

Mechanical, Industrial and Aerospace Engineering

Presented in Partial Fulfillment of the Requirements

For the Degree of

Doctor of Philosophy (Mechanical Engineering) at

Concordia University

Montreal, Quebec, Canada

November 2017

Concordia University

School of Graduate Studies

This is to certify that the thesis prepared

By: Xiaoming Zhang

Entitled: Modeling and Control of the Cooperative Automated Fiber Placement System

and submitted in partial fulfillment of the requirements for the degree of

Doctor of Philosophy (Mechanical Engineering)

complies with the regulations of the University and meets the accepted standards with respect to originality and quality.

Signed by the final Examining Committee:

Dr. Saifur Rahaman	Chair
Dr. Guangjun Liu	External Examiner
Dr. Krzysztof Skonieczny	External to Program
Dr. Henry Hong	Examiner
Dr. Youmin Zhang	Examiner
Dr. Wenfang Xie	Co-Supervisor
Dr. Suong Van Hoa	Co-Supervisor

Approved by _____

Dr. Ali Dolatabadi, Graduate Program Director

December 14, 2017 _____

Dr. Amir Asif, Dean

Faculty of Engineering and Computer Science

ABSTRACT

Modeling and Control of the Cooperative Automated Fiber Placement System

Xiaoming Zhang, Ph.D.

Concordia University, 2017

The Automated Fiber Placement (AFP) machines have brought significant improvement on composite manufacturing. However, the current AFP machines are designed for the manufacture of simple structures like shallow shells or tubes, and not capable of handling some applications with more complex shapes.

A cooperative AFP system is proposed to manufacture more complex composite components which pose high demand for trajectory planning than those by the current APF system. The system consists of a 6 degree-of-freedom (DOF) serial robot holding the fiber placement head, a 6-DOF revolute-spherical-spherical (RSS) parallel robot on which a 1-DOF mandrel holder is installed and an eye-to-hand photogrammetry sensor, i.e. C-track, to detect the poses of both end-effectors of parallel robot and serial robot.

Kinematic models of the parallel robot and the serial robot are built. The analysis of constraints and singularities is conducted for the cooperative AFP system. The definitions of the tool frames for the serial robot and the parallel robot are illustrated. Some kinematic parameters of the parallel robot are calibrated using the photogrammetry sensor.

Although, the cooperative AFP system increases the flexibility of composite manufacturing by adding more DOF, there might not be a feasible path for laying up the fiber in some cases due to the requirement of free from collisions and singularities. To meet the challenge, an innovative semi-offline trajectory synchronized algorithm is proposed to incorporate the on-line robot control in following the paths generated off-line especially when the generated paths are infeasible for the current multiple robots to realize. By adding correction to the path of the robots at the points where the collision and singularity occur, the fiber can be laid up continuously without interruption. The correction is calculated based on the pose tracking data of the parallel robot detected by the photogrammetry sensor on-line. Due to the flexibility of the 6-DOF parallel robot, the optimized offsets with varying movements are generated based on the different singularities and constraints. Experimental results demonstrate the successful avoidance of singularities and joint limits, and the designed cooperative AFP system can fulfill the movement needed for manufacturing a composite structure with Y-shape.

ACKNOWLEDGMENTS

I would like to express my deepest gratitude to my supervisors Prof. W.F. Xie and Prof. S.V. Hoa for their continuous support during my research. Their help, patience and encouragement enabled me to complete this thesis. I benefited greatly from their guidance during the study in Concordia University.

I wish to acknowledge the financial assistance funded by The Natural Science and Engineering Research Council (NSERC) Industrial Research Chair in Automated Composites Manufacturing and the Fonds de recherche du Québec – Natrue et technologies (FRQ-NT).

I am deeply thankful to Tingting Shu, Pengcheng Li, Rui Zeng, and Clement Hely for their help in our research group.

Additionally, I would like to thank all of my friends who have been supporting me go through the recent years.

Last but not least, I sincerely thank my family for their support and understanding.

CONTENTS

LIST OF FIGURES

LIST OF TABLES

LIST OF SYMBOLS

A_i	Six vertices of the base platform of the parallel robot
A_i^b	Coordinates of the six vertices of the base platform in terms of the base frame of the parallel robot
a	The side lengths of the top semi-regular hexagon of the parallel robot
$\boldsymbol{a}_i$	Vectors along line OA_i
$\boldsymbol{A}$	Jacobian matrix of parallel robot
B_i	Connected points of the distal links and the proximal links of the parallel robot
b	The side lengths of the base semi-regular hexagon of the parallel robot
$\boldsymbol{b}_i$	Vectors along line OB_i in terms of the base frame of the parallel robot
$\boldsymbol{B}$	Jacobian matrix of parallel robot
B_j	Camera matrix
c	The side lengths of the top semi-regular hexagon of the parallel robot
$\boldsymbol{c}$	Vector along the line OO' of the parallel robot
C	Intersection point of the wrist axes of the serial robot

$\dot{\boldsymbol{c}}$	Linear velocity vector of the intersection point of the wrist axes with respect to the base frame of the serial robot
$C_{\_D}$	Planned path of the serial robot
$\boldsymbol{c}_s^d(t)$	Desired compensation pose trajectory of the tool frame of the serial robot F_t^S with respect to the base frame F_b
$c\theta$	Cosine of angle θ
d	The side lengths of the base semi-regular hexagon of the parallel robot
$\boldsymbol{d}_i$	Vectors along lines OT_i of the parallel robot
$\boldsymbol{d}$	Vector that tangent to the surface at the current point on the trajectory
Δd_{min}	Threshold of minimum distance between the sixth frame attached on the joint 6 and the first frame attached on the joint 1 along x and y direction of the first frame
Δd	Distance of translation movement of the serial robot
Δd_3	Offset distance along the y axis of the frame attached on the joint 3
$d(\theta_i)$	Direction indicator of joint i
$\boldsymbol{e}_i$	Direction vectors of the i^{th} joint axes with respect to the base frame of the serial robot
$\boldsymbol{e}_i(t)$	Pose error of i^{th} robot

$\boldsymbol{e}_s(t)$	Pose errors of the serial robot
$\boldsymbol{e}_p(t)$	Pose errors of the parallel robot
$\boldsymbol{e}_1$	Unit vector tangent to the curve
$\boldsymbol{e}_2$	Normal unit vector which is perpendicular to the mold surface
$\boldsymbol{e}_3$	Bi-normal unit vector which is the offset direction
$\boldsymbol{e}_s^c(t)$	Compensation error of the serial robot
F_s	Sensor frame
F_O	Object frame
F_b	Base frame of the parallel robot
F_t^p	Tool frame of the parallel robot
F_t^S	Tool frame of the serial robot
$f(\boldsymbol{p})$	Inverse kinematic equations
$f\big(\boldsymbol{p}_1(t), \boldsymbol{p}_2(t), \dots, \boldsymbol{p}_n(t)\big)$	Synchronization function of n robots
$\boldsymbol{I}_{\boldsymbol{p}\boldsymbol{w}_s}$	Inverse kinematic function of the serial robot
$\boldsymbol{J}_s$	Joint space constraints of the serial robot
$\boldsymbol{J}$	Jacobian matrix of the serial robot
$det(\boldsymbol{J})$	Determinant of the Jacobian matrix
$\boldsymbol{K}$	Major axis of trajectory planning
L	Distance of the distal link of the parallel robot

$L_{B_iT_i}$	Distances between B_i and T_i
$L_{A_iB_i}$	Distances between A_i and B_i
$L_{T_iT_{i+1}}$	Lines by connecting the revolute joints of the parallel robot in sequence
$L_{A_iA_{i+1}}$	Lines by connecting the spherical joints attached on the base platform of the parallel robot in sequence
L_z	Lengths from the center points of the spherical joints attached on the proximal links to the top surface of the proximal links of the parallel robot
l_{12}	Length from the axis 2 to the surface of the base of the Denso robot
l_3	Length between axis 2 and axis 3 of the Denso robot
l_{3z}	Length between axis 3 and axis 4 of the Denso robot
l_{45}	Length from the axis 3 to the axis 5 of the Denso robot
l_{67}	Length from the end point of the end-effector to the axis 5 of the Denso robot
$M(i,1)$	Elements in the rotation matrix of the upper platform with respect to the base frame of the parallel robot
M	Actuator parameter space
${}^{C}_{j}M$	The projection matrix of each camera
$\boldsymbol{n}$	Normal unit vector which is perpendicular to the mold surface
$\boldsymbol{n}_i$	The unit vector along distal links *L*

O	Origin of the base frame of the parallel robot
O'	Origin of the upper frame of the parallel robot
O_i	Spherical centers of the six clusters of the sphere in workspace analysis of the parallel robot
O_{Oi}	Center points of the circles in workspace analysis of the parallel robot
$O_{\_P}$	Origin of the parallel robot's end-effector
$O_{\_P'}$	Origin of the parallel robot's end-effector after translation movement
$O_{\_P''}$	Origin of the parallel robot's end-effector after orientation movement
$O_{\_D}$	Origin of the serial robot's end-effector
$O_{\_D'}$	Origin of the serial robot's end-effector after translation movement
$O_{\_D''}$	Origin of the serial robot's end-effector after orientation movement
$\boldsymbol{p}$	Initial pose of the upper platform with respect of the base frame of the parallel robot
$\Delta\boldsymbol{p}$	Pose correction
p_x	x coordinate of the end-effector of the Denso robot
p_y	y coordinate of the end-effector of the Denso robot
p_z	z coordinate of the end-effector of the Denso robot

$\boldsymbol{P}_w$	Coordinates in Cartesian system
$\boldsymbol{p}_i^o$	Homogenous coordinates of the n targets on the object with respect to the object frame
$\boldsymbol{p}_c(t)$	The current pose of the object frame F_O with respect to the sensor frame F_s
${}_i^S P$	The homogenous coordinates of each target with respect to the sensor frame F_s
${}_{ij}^C P$	The projection coordinates of each target on the image plane of the j^{th} camera
$\boldsymbol{p}_i(t)$	Pose of i^{th} robot
$\boldsymbol{p}_i^d(t)$	Desired poses of i^{th} robot
$\boldsymbol{p}_s(t)$	Pose trajectories of the serial robot in reference to the base frame F_b
$\boldsymbol{p}_p(t)$	Pose trajectories of the parallel robot in reference to the base frame F_b
$\boldsymbol{P}$	Projection of the major axis
$\boldsymbol{P}_i$	Current point of the trajectory
$\boldsymbol{P}_j^i$	translation matrix of ${}_j^i\boldsymbol{T}$
$\boldsymbol{p}_p^c$	Current pose of the parallel robot
$\boldsymbol{P}_F$	Intermediate point computed by translating $\boldsymbol{P}_i$ along $\boldsymbol{t}$ of a small distance

$\boldsymbol{P}_{i+1}$	Point of the path generated by projecting $\boldsymbol{P}_F$ onto the mold surface along $-\boldsymbol{n}$
$P_{\_O}$	Initial point of the serial robot's tool coordinate frame
$\Delta \boldsymbol{p}_{\boldsymbol{p}}^{\boldsymbol{o}}$	Offset of the parallel robot
$\boldsymbol{p}_s^c$	Current pose of the serial robot
$\Delta \boldsymbol{p}'^{\boldsymbol{o}}_{\boldsymbol{p}}$	Full offset of the parallel robot
$\boldsymbol{p}_s^c(t)$	Current pose of the tool frame of the serial robot F_t^S with respect to the base frame F_b
$P(x_s^d(k), y_s^d(k), z_s^d(k))$	Three position variables of the desired compensation pose $\boldsymbol{c}_s^d(t)$ at $\mathrm{t} = k$
$P\left(x_p^o(k), y_p^o(k), z_p^o(k)\right)$	Three position variables of the current pose of the parallel robot with offset inputs $\boldsymbol{p}_p^o(t)$ at $\mathrm{t} = k$
$\boldsymbol{p}'^d_s(t)$	Offline trajectory planning pose of serial robot without compensation inputs
$\boldsymbol{p}_p^o(t)$	Current pose of the parallel robot with offset inputs
$\boldsymbol{p}'^c_s$	Current pose of the serial robot without compensation inputs relative to the base frame F_b
$\boldsymbol{p}_s^c(k-1)$	The former step pose of serial robot
$\boldsymbol{p}_p^c$	Current pose of the parallel robot without offset inputs
$\boldsymbol{q}$	Joint vector of robot
$\dot{\boldsymbol{q}}$	Velocity of robot joint

$\ddot{\boldsymbol{q}}$	Acceleration of robot joint
$\boldsymbol{q}_{min}$	Minimum joint limit of the serial robot
$\boldsymbol{q}_{max}$	Maximum joint limit of the serial robot
r	Length of the proximal link of the parallel robot
$\boldsymbol{r}$	Vector along the proximal link of the parallel robot
$\boldsymbol{R}$	The orientation matrix of the upper platform with respect to the base frame of the parallel robot
r_{ij}	The ij element in the pose matrix of the end-effector of the Denso robot
$\boldsymbol{r}_i$	Position vectors of the intersection point with respect to the origin of the coordinate frame attached on the i^{th} joint axis of the serial robot
$R(\alpha_c, \beta_c, \gamma_c)$	Rotation matrix from the object frame F_O to the sensor frame F_s
R	Radius of the bowl
$\boldsymbol{R}_j^i$	orientation matrix of ${}_j^i\boldsymbol{T}$
$\boldsymbol{R}(z, \Delta)$	Orientation matrix of the frame attached on the joint 5 about z axis by Δ
$R(\alpha_s^d(k), \beta_s^d(k), \gamma_s^d(k))$	Three orientation variables of the desired compensation pose $\boldsymbol{c}_s^d(t)$ at $\mathrm{t} = k$
$R\left(\alpha_p^o(k), \beta_p^o(k), \gamma_p^o(k)\right)$	Three orientation variables of the current pose of the parallel robot with offset inputs $\boldsymbol{p}_p^o(t)$ at $\mathrm{t} = k$

$[R_w \quad \theta_w \quad \alpha_w]^T$	Coordinates in polar system
$S(u,v)$	Mold surface
$s\theta$	Sine of angle θ
T_i	Six vertices of the upper platform of the parallel robot
T_i^p	Coordinates of the six vertices of the upper platform with respect to the upper frame of the parallel robot
T_i^b	Coordinates of the vertices of the upper platform with respect to the base frame of the parallel robot
$\boldsymbol{t}_i$	Vectors along line $O'T_i$ with respect to the upper frame of the parallel robot
$\boldsymbol{t}_{bi}$	Vectors along line $O'T_i$ with respect to the base frame of the parallel robot
${}_S^C T_i$	Homogenous transformation matrix from the sensor frame F_s to the j^{th} camera frame
${}_o^s \boldsymbol{T}$	Homogenous transformation matrix from the object frame F_O to the sensor frame F_s
${}_p^b T$	Homogenous transformation matrix from the upper frame to the base frame of the parallel robot
$\boldsymbol{t}$	Vector computed by rotating $\boldsymbol{d}$ around the surface normal vector $\boldsymbol{n}$ by the selected placement angle ψ
t_1	Producing processes of planar surface
t_2	producing processes of curved surface

${}^{b}_{s}\boldsymbol{T}$	Homogenous transformation matrix of the current pose of the serial robot with respect to the base frame
${}^{i}_{j}\boldsymbol{T}$	Homogeneous transformation associated with the frames that are attached to the joint j and i
${}^{i}_{s}\boldsymbol{T}$	Homogeneous transformation between the tool frame of serial robot and the frame attached on joint i
${}^{b}_{p}\boldsymbol{T}$	Homogenous transformation matrix of the current pose of the parallel robot relative to the base frame
${}^{b}_{s}\boldsymbol{T}$	Homogenous transformation matrix of the current pose of the serial robot relative to the base frame
${}^{p}_{3}\boldsymbol{T}$	Homogenous transformation matrix of the frame attached on the joint 3 with respect to the tool frame of parallel robot
${}^{b}_{cs}\boldsymbol{T}$	Homogenous transformation matrix of the desired compensation pose with respect to the base frame F_b
${}^{b}_{op}\boldsymbol{T}$	Homogenous transformation matrix of the current pose of the parallel robot with offset inputs at $\mathrm{t} = k$ relative to the base frame F_b
${}^{op}_{cs}\boldsymbol{T}$	Homogenous transformation matrix from the tool frame of the serial robot F_t^S to the tool frame of the parallel robot F_t^P with offset inputs
${}^{b}_{p}\boldsymbol{T}$	Homogenous transformation matrix of the current pose of the parallel robot without offset inputs relative to the base frame F_b

${}^{p}_{s}\boldsymbol{T}$	Homogenous transformation matrix from the tool frame of the serial robot F_t^S to the tool frame of the parallel robot F_t^P without offset inputs
$\boldsymbol{\Delta T}$	Change of kinematic relationships between the two end-effector
${}^{b}_{s}\boldsymbol{T}$	Homogenous transformation matrix of the current pose of the serial robot without compensation inputs relative to the base frame F_b at $\mathrm{t} = k - 1$
$\boldsymbol{W}_s$	Workspace constraints of the serial robot
X_{A_i}	The x coordinate of the i^{th} vertex of the base platform in terms of the base frame of the parallel robot
x_{T_i}	The x coordinate of the i^{th} vertex of the upper platform with respect to the upper frame of the parallel robot
X_{T_i}	The x coordinate of the i^{th} vertex of the upper platform with respect to the base frame of the parallel robot
x_c, y_c, z_c	The three origin position variables of the object frame F_O with respect to the sensor frame F_s
Y_{A_i}	The y coordinate of the i^{th} vertex of the base platform in terms of the base frame of the parallel robot
y_{T_i}	The y coordinate of the i^{th} vertex of the upper platform with respect to the upper frame of the parallel robot
Y_{T_i}	The y coordinate of the i^{th} vertex of the upper platform with respect to the base frame of the parallel robot

Z_{A_i}	The z coordinate of the i^{th} vertex of the base platform in terms of the base frame of the parallel robot
z_{T_i}	The z coordinate of the i^{th} vertex of the upper platform with respect to the upper frame of the parallel robot
Z_{T_i}	The z coordinate of the i^{th} vertex of the upper platform with respect to the base frame of the parallel robot
$Z_{\_D}$	Direction Z of the tool frame of the serial robot
$\alpha_c, \beta_c, \gamma_c$	The three orientation variables of the object frame F_O with respect to the sensor frame F_s
α	Orientation of between the two robots' end-effectors
β	Orientation of the parallel robot's end-effector
ω	Orientation of the serial robot's end-effector
$\boldsymbol{\omega}$	Angular velocity of the end-effector
θ_i	Actuators angles
$\Delta\theta_{imin}$	Threshold of the joint i closed to 0°
$\theta_i(k)$	Current angle of the joint i
$\theta_i(k-1)$	Former step angle of the joint i
$\Delta\theta_i$	Offset movement of joint i of the serial robot
θ_{imax}	Maximum limit of joint i of the serial robot
θ_{imin}	Minimum limit of joint i of the serial robot
θ_{ni}	n solution of the inverse kinematic calculation

$\dot{\boldsymbol{\theta}}$	Vector of actuator joint rates
$\boldsymbol{\varepsilon}(t)$	Synchronization error
ε_c	Condition coefficient
ε_p	Penalty coefficient
$\| \ \|_*$	Norms in corresponding parameter space
$\Phi(\boldsymbol{p}_i(t))$	The higher order terms in the Taylor series expansion of the synchronization function
ϕ	Targeted placement angle
$\boldsymbol{\rho}$	Constant difference between the tool frame of the serial robot F_t^S and the tool frame of the parallel robot F_t^P
$\boldsymbol{\psi}_s(t)$	Relative kinematic relationship of the tool frame of the serial robot F_t^S with respect to the tool frame of the parallel robot F_t^P
ψ	Selected placement angle
$\delta_i(t)$	Diagonal coupling parameter regarding the first-order error $\boldsymbol{e}_i(t)$
$\Delta_{p_1}^A$	Cauchy index of matrix $\boldsymbol{A}$ in the point p_1
$\Delta_s^d(t)$	Compensation pose of the serial robot

LIST OF ABBREVIATIONS

AFP	Automated Fiber Placement
API	application programming interface
ATL	Automated Tape Laying
D-H	Denavit–Hartenberg
DOF	degree-of-freedom
DPM	Dynamic path modification
FTP	file transfer protocol
PCDK	PC developer's kit
PD	Proportional-derivative
RSS	revolute-spherical-spherical
RTM	Resin Transfer Molding
SPS	spherical-prismatic-spherical
UPS	universal-prismatic-spherical
VB	Visual Basic

CHAPTER 1

1 INTRODUCTION

1.1 Overview

Composite materials are being used widely in many industry areas such as aerospace, automobiles, wind turbines, civil infrastructures, medical devices etc. [1]. These materials are generally lightweight, of good chemical and corrosion resistance, better impact characteristics, excellent mechanical properties, greater design flexibility, and offer attractive strength-to-weight and stiffness-to-weight ratios over the traditional structural materials, such as steel, aluminum or titanium alloys [2]. The aerospace industry is increasingly substituting traditional fuselage and wing component materials such as aluminum for composite materials, which can constitute up to 65% of empty aircraft weight [3]. About 30% of external structure of Boeing 767 consists of composites [4]. Boeing 787 Dreamliner with the capacity of 200-250 passengers uses 15-20% less fuel than any other airplanes. It is the first commercial jet to be made with most of its primary structure consisting of composite materials, which is about 57%. Similarly, aero engines such as GE's Aviation GEnx unit have fan cases and blades in cooler section of compressor made of carbon fiber composites, which provides 20% reduction in operational cost and 15% lower emissions. Furthermore, the composite fan cases have saved 180 kg compared with the aluminum option [5].

However, the traditional methods of producing composite components involve manual lay-up and tape-laying. These processes are time-consuming, labor intensive and hazardous, with high-material scrap rate and low repeatability [6]. The components are formed by manually cutting the tape to the required length and laying down to the desired paths layer by layer. Operators must be familiar with the materials that are used and maintain the stringent safety precautions. Furthermore, the defects can result in the loss of life, especially within the aerospace industry [7].

Alternative automated processes like Resin Transfer Molding (RTM), Automated Tape Laying (ATL) and AFP are developed in order to make composite components competitive compared to the milled parts [8]. The advent of those automated processes have brought significant improvement on the manufacturing of composite in terms of speed of material deposition, repeatability, good compaction, reduction of waste, and seamless transfer of files from design to manufacturing etc. [9]. RTM involves the injection of a composite matrix in liquid phase into a mold cavity with preformed fabric. Compared to the manual lay-up process, the main disadvantage of RTM is the relatively low fiber volume fraction [6]. ATL is employed to deliver wide prepreg tape onto a surface of the mold in direct contact using a composite tape lay-up end-effector mounted on a large robotic manipulator. Lay-up speed, tape temperature and tape tension can be controlled during lay-up [10]. The tape is designed for thermoset where a post lay-up autoclave is required [11] and thermoplastic where autoclave is not required [12]. The tow placement technology can achieve cost reductions as high as 50% and scrap reductions up to 75% in numerous military applications validated by tests made on a wide variety of large composite structures [13]. AFP is similar to ATL but laying a band of narrow prepreg composite tows simultaneously side-by-side on the mold surface instead of laying a single tape. The incidence of fiber wrinkling is reduced while a reasonable overall composite lay-up width is maintained when compared to ATL. The parts of Bell Helicopter, the fuselage of Boeing 787 and ABB electric motor with a thermoplastic overhang bandages [2] and components of many aircraft structures have been manufactured by AFP successfully. [6] presents that Bell realized 47% material savings and a production rate of 450% that of its traditional process with the specimens passing all performance tests.

1.2 Problems and Solutions

Even though the AFP machines have been employed in industry manufacturing processes successfully and achieved a great performance, most of the current AFP machines are designed for the manufacture of airframe components, which are usually shallow shells or tubes, as the machine (Automated Dynamics) in Concordia University shown in Figure 1.1, and are not capable of manufacturing more complex shapes, such as the bicycle frame with the closed loop which requires complex maneuvering, the fan blade of the jet engine with complex curvatures, tubes with

T shape or Y shape or tube with flanges having circular shape like exhaust ducts in jet engines as shown in Figure 1.2 and Figure 1.3. To be able to expand the manufacture capabilities of AFP machines in a simple and low cost way, it is necessary to increase the number of DOF of the robotic system.

Figure 1.1. AFP Machine

Figure 1.2. Structures with Complex Shapes

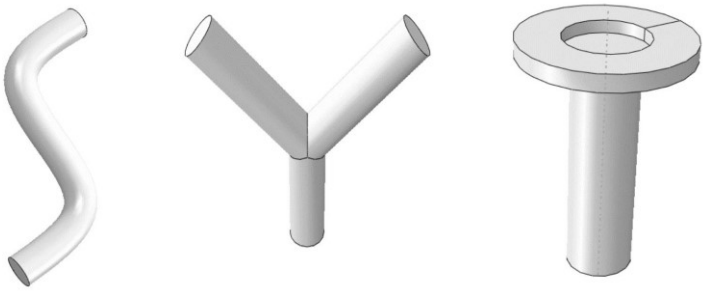

Figure 1.3. Frames with Complex Geometry

One solution is using another manipulator to hold the mandrel to be manufactured as shown in Figure 1.4. The advantages of the integrated AFP manufacturing workcell using two open-loop serial manipulators are the large workspace and the dexterity to lay the fiber to manufacture the more complex geometry like human arms. But the load carrying capacity and the precision positioning capability are rather poor due to the cantilever structure [14]. For the applications of AFP machine where high load carrying capacity and precise positioning are of paramount importance, an alternative to such serial manipulators manufacturing workcell is desirable.

Figure 1.4. Two Open-loop Serial Manipulators

Another solution is introducing the 6 DOF parallel robot to AFP machines due to its better stiffness and precise positioning capability [15], as shown in Figure 1.5. A cooperative AFP system consisting of a 6 DOF manipulator, a 6-RSS parallel robot, a spindle mounted on the platform to hold the mandrel is proposed in my previous paper [16].

Figure 1.5. One Parallel Robot and One Serial Manipulator

The accurate pose of end-effector of both robots should be measured on-line to achieve the precise positioning and control. Moreover, the complexity of trajectory planning for AFP machine using multiple robots increases in comparison with the traditional way.

1.3 Scope and Objectives

The purposes of this project are to manufacture composite material components with more complicated structures and to improve the production efficiency by adding DOF to the AFP machine. In order to fulfill those objectives, a cooperative AFP system is proposed. It includes a 6 DOF serial robot holding the fiber placement head, a 6-RSS parallel robot on which a one DOF mandrel holder is installed and a photogrammetry sensor to detect the poses of both end-effectors of parallel robot and serial robot.

The traditional way of trajectory planning is strictly subject to the constraints of the robot. Collision avoidance and singularity avoidance are also needed to be considered in the design phase. As to the trajectory planning of fiber placement, apart from the limitation of minimum turning radius and defects resulted from gaps and overlaps, more requirements need to be satisfied, such as multiple layers, continuous laying without cutting tows to keep the consistent stress[7, 9, 97]. The roller of the fiber process head should be perpendicular to the surface of the mandrel all the time [17, 104]. In the multiple robot machines, the trajectories should be generated for each robot. When the manufactured composite part is of intricate shape, the trajectory generation for both robots free from collision and singularities and meanwhile satisfying the above requirements becomes increasing difficult. In certain cases, no feasible trajectory can be generated for the continuous fiber placement. The traditional practice, namely, off-line generating path and inputting the generated path to robot controller for on-line fiber placement, cannot fulfil the task of manufacturing intricate composite components.

To meet the challenge, a semi-offline trajectory synchronized algorithm is proposed to incorporate the on-line robot control in following the paths generated off-line especially when the generated paths are infeasible for the current multiple robots to realize due to the constraints and singularities. By adding a correction to the paths of the robots at the points where the collision and singularity occur, the fiber can be laid up continuously without interruption. The correction is calculated based

on the pose tracking data of the parallel robot detected by the photogrammetry sensor on-line. Due to the flexibility of the 6 DOF of the parallel robot, the optimized offsets with varying orientation and translation movements are generated based on the different singularities and constraints. To my best knowledge, this is the first time to consider the manipulation of both robots in the path planning of AFP machine.

1.4 Contributions

The major contributions of the research work are listed as follows:

- The mathematical model of the cooperative AFP system including the forward and the inverse kinematics of the serial robot and the parallel robot is built.
- A comprehensive analysis on constraints and singularities of the cooperative AFP system is given. Kinematic constraint consists of the workspace constraint and the joints space constraint.
- The pose estimation using a photogrammetry sensor is introduced, and the processes of the frame definitions for both the parallel robot and the serial robot are presented. In order to refine the kinematic model and the CAD model of the 6-RSS parallel robot, some parameters in parallel robot's kinematic model are calibrated using the photogrammetry sensor, i.e. C-track.
- The semi-offline trajectory synchronized algorithm for the cooperative AFP system is developed to calculate the pose correction based on the measured poses and add the correction to the pre-planned trajectory for avoiding singularities, optimizing joint limits and expanding the workspace on-line.
- Simulation on the proposed cooperative AFP system including a 6-DOF RSS parallel and a 6-DOF Denso robot is conducted in SimMechanics for fiber placement of the bowl shape mandrel.
- Experimental tests of the cooperative AFP manufacturing process have been conducted on fiber placement of a Y-shape mandrel with joint limit and wrist singularity in the pre-planned trajectory.

1.5 Publications

The achieved research results have been demonstrated in the following journal papers, conference papers, and abstracts presented to symposium and invited talks.

Journal Papers:

1. Xiaoming Zhang, Wenfang Xie, Suong V. Hoa, Rui Zeng, "Design and Analysis of Collaborative Automated Fiber Placement Machine", International Journal of Advanced Robotics and Automation, 1-14, 2016.
2. Xiaoming Zhang, Wenfang Xie, Suong V. Hoa, "Semi-offline Trajectory Synchronized Algorithm of the Cooperative Automated Fiber Placement System", Robotics and Computer-Integrated Manufacturing, (51), 53-62, 2018.
3. Xiaoming Zhang, Wenfang Xie, "Operation of the Cooperative Automated Fiber Placement System", submitted to Journal of Visualized Experiments, 2017.

Conference Papers:

1. Xiaoming Zhang, Wenfang Xie, Suong V. Hoa, "Modeling and Workspace Analysis of Collaborative Advanced Fiber Placement Machine", Proceedings of the ASME 2014 International Mechanical Engineering Congress and Exposition 2014-38553, Nov.14-20, 2014.
2. Rui Zeng, Shulin Dai, Wenfang Xie, Xiaoming Zhang, "Determination of the proper motion range for the rotary actuators of 6-rss parallel robot", Canadian Committee for the Theory of Machines and Mechanisms, May 25-28, Ottawa, Canada, 2015.
3. Sahar, Alinia, Amir Hajilo, Wenfang Xie and Xiaoming Zhang, "Modeling and Pose Control of a 6-RSS Parallel Robot using Multi-Objective Optimization", Proceedings of The Canadian Society for Mechanical Engineering International Congress 2016, June 26-29, 2016.
4. Pengcheng Li, Rui Zeng, Xiaoming Zhang and Wen-Fang Xie, "Relative Posture-based Kinematic Calibration of a 6-RSS Parallel Robot by Using a Monocular Vision System", IEEE International Conference on Robotics and Biomimetics, 2017.

Abstracts:

1. Xiaoming Zhang, Wenfang Xie, Suong V. Hoa, “Design and Analysis of Collaborative Automated Fiber Placement Machine”, Collaborative Conference on Robotics, Phuket, Thailand, Nov. 4-6, 2016.
2. Xiaoming Zhang, Wenfang Xie, Suong V. Hoa, “Modeling of Cooperative AFP machine”, Proceedings of 1st International Symposium on Automated Composites Manufacturing, Montreal April 11-12, 2013.

1.6 Thesis Organization

This dissertation is consists of 8 Chapters. The outline of the thesis is given as follows.

- Chapter 1 summarizes the overview of composite material and AFP machine. The problems of the current AFP machine and solutions are introduced. The scope and objectives of the dissertation are subsequently given. And then, publications related to this project are listed.
- Chapter 2 presents the literature reviews on the current AFP machines, kinematic, workspace and singularities analysis of robots, multiple robots, trajectory planning and pose tracking.
- Chapter 3 builds the mathematical model of the cooperative AFP system including the forward and the inverse kinematics of the serial robot and the parallel robot. A numerical forward kinematic method, quasi-Gough forward kinematic algorithm, is presented to determine the uniqueness of forward kinematic solution of the 6-RSS parallel robot. The process of calculating the inverse kinematic of the serial robot based on Denso robot is given. To deal with the multiple solutions, the shortest distance rule is used to choose a solution closest to the current robot. The simulation using SimMechanics is conducted for fiber placement of the bowl shape mold.
- Chapter 4 analyses the constraints and singularities of the cooperative AFP system. Kinematic constraint consists of the workspace constraint and the joints space constraint.

Three types of singularities for the wrist-partitioned serial robot, which are elbow singularity, shoulder singularity and wrist singularity, are derived.

- Chapter 5 introduces the pose estimation of an object, and presents the processes of the frame definitions for both the parallel robot and the serial robot. In order to refine the kinematic model and the CAD model of the 6-RSS parallel robot, some kinematic parameters applied in parallel robot modelling are calibrated using C-track, the photogrammetry sensor.
- Chapter 6 develops a semi-offline trajectory synchronized algorithm to calculate the pose correction based on the measured poses and add the correction to the pre-planned trajectory for avoiding singularities, optimizing joint limits and expanding the workspace on-line. The off-line trajectory planning and the decomposition processes for the cooperative AFP system is illustrated. The generated offsets for the parallel robot are calculated based on different conditions including singularity avoidance and joints constraints avoidance.
- Chapter 7 introduces the experimental setup of the cooperative AFP system, which consists of one 6 RSS parallel robot, one 6 DOF serial robot, a fiber processing head, a spindle which is mounted on the platform. A photogrammetry sensor in an eye-to- hand configuration is adopt to obtain the pose measurement for feedback. The hardware setup of the cooperative AFP system is illustrated. Experimental tests demonstrate the cooperative AFP manufacturing process for Y-shape mandrel with joint limit and wrist singularity in the pre-planned trajectory using the proposed semi-offline trajectory synchronized algorithm.
- Chapter 8 summarizes the conclusions and contributions of the dissertation. And the further studies are recommended.

CHAPTER 2

2 LITERATURE REVIEW

A literature survey on the relevant studies regarding the current AFP machines, kinematic, workspace and singularities analysis of robots, multiple robots, trajectory planning for AFP machine, and pose tracking is conducted in this chapter.

2.1 AFP Machines

Many kinds of AFP machines exit in the current industrial market. The system shown in Figure 1.1 is designed for small part manufacturing. The grounded industrial robotic manipulator limits the motion of the robot and the maximum size of the manufacturing components [18].

In order to increase the size of the components, a bigger robotic manipulator can be applied in the AFP machine. In addition, the robotic manipulator can be attached to the rail. Figure 2.1 shows the example of AFP machine from Coriolis with a large robotic arm assembled on the rail [19].

Figure 2.1. AFP Machine Attached to the Rail [19]

The AFP machine employed rail can manufacture long components and also is capable of working on several different mold tools using one manipulator. An example of a single manipulator equipped with a rail and two mold tool positioners, including one vertical positioner and one horizontal positioner, from Coriolis is shown in Figure 2.2.

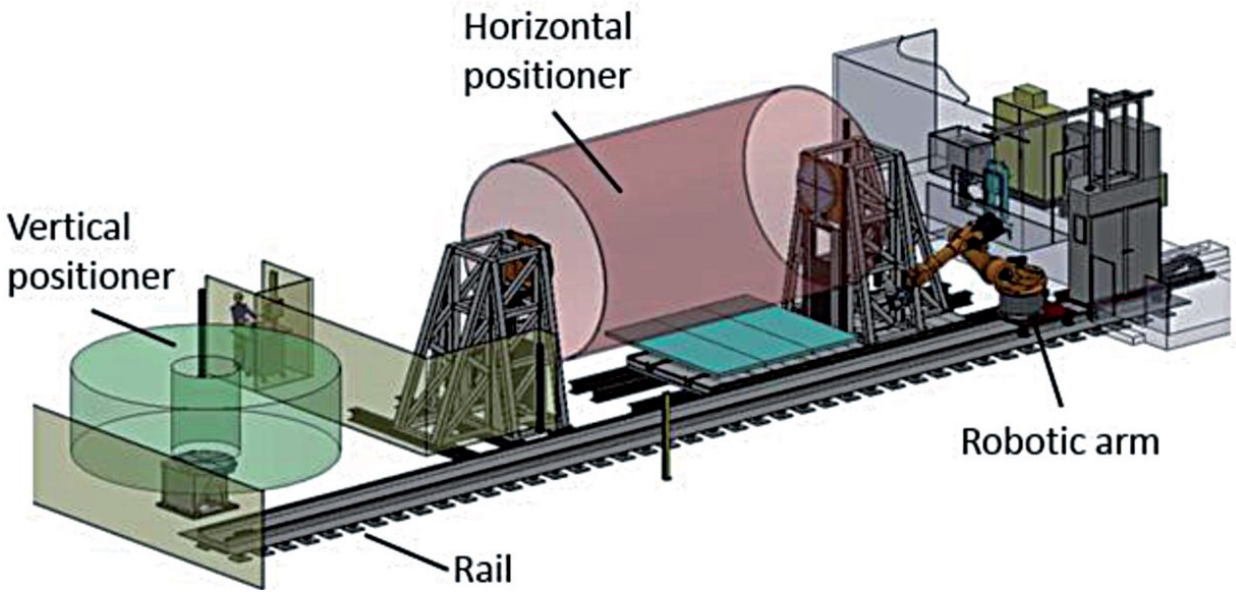

Figure 2.2. AFP Machine Equipped with Rail and Two Mold Tool Positioners [19]

For large components like wing covers or fuselages, gantry style AFP or ATL machines are used. Examples of large components manufactured by gantry style system is shown in Figure 2.3, where A is from Electroimpact [20], B is from MTorres [21], and C is from Ingersoll [22].

The above mentioned AFP machine has been designed to manufacture large size composite structures by adding a rail and tool positioners [19] or using a gantry style robot. The composite structure that they can manufacture are usually shallow shells or tubes. The main reason is that the degree of freedom of AFP machine has been increased to 8 and the manufacture flexibility of the intrinsic structure is thus limited. To manufacture more complex structure, an extra 6-DOF robot should be added to the system.

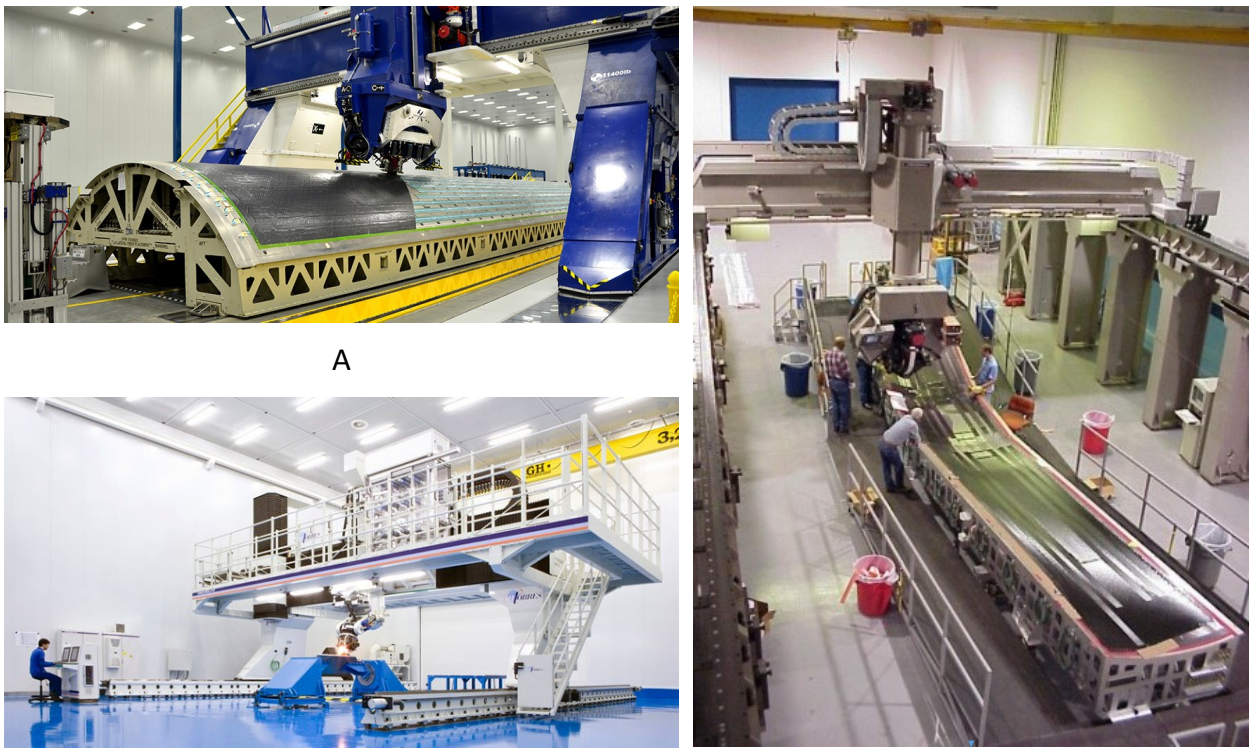

A

B

C

Figure 2.3. Gantry Style AFP Machine

2.2 Robots of the Cooperative AFP System

2.2.1 Introduction of Parallel Robot

The most celebrated parallel robot, known as Stewart platform, was proposed in 1965 and evolved into a popular research topic of robotics after the 1980s [14]. Such manipulating structure was originally designed by Stewart as a 6-DOF mechanism to simulate flight conditions by generating general motion in space [23]. It consisted of a triangular platform supported by ball joints over three legs of adjustable lengths and angular altitudes connected to the ground through two-axis joints. Gough suggested to make the platform manipulator a fully parallel-actuated mechanism by using six linear actuators all in parallel like the machine in [24].

Generally, the structure of Stewart platform consists of two rigid bodies which are referred to as the base and the platform connected through six extensible legs. The structure with spherical joints at both ends of each leg is referred to as 6-spherical-prismatic-spherical (SPS) Stewart platform,

as shown in Figure 2.4. The structure with spherical joint at the top and universal joint at the base of each leg is referred to as 6-universal-prismatic-spherical (UPS) Stewart platform as shown in Figure 2.5. Both the manipulating structures are actuated at the six prismatic joints of the legs and are identical to each other regarding all input-output relationships except that the 6-SPS structure possesses six passive DOF corresponding to the rotation of each leg about its axis [14].

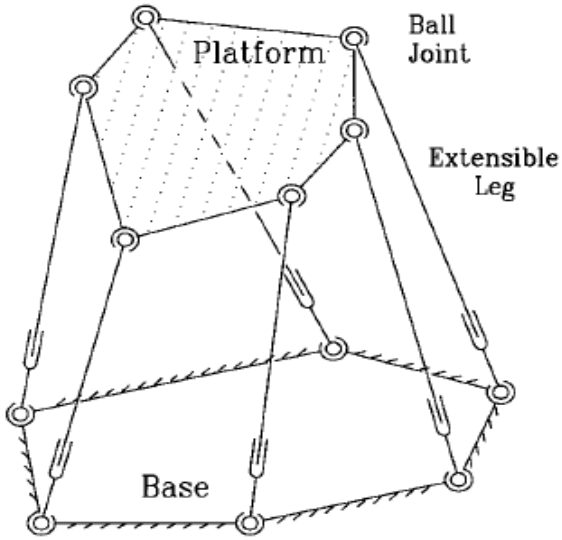

Figure 2.4. The 6-SPS Stewart Platform [14]

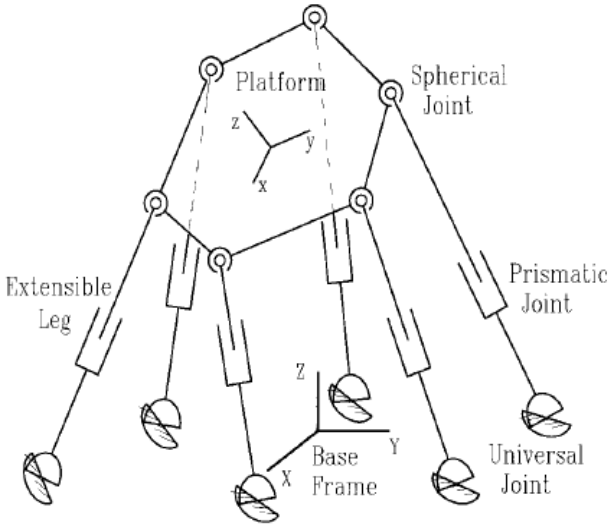

Figure 2.5. The 6-UPS Stewart Platform [14]

The advantages of the Stewart platform include higher stiffness, strong carrying capacity [25, 26], good dynamic capabilities and less accumulated errors of joints compared to serial robots [27, 28]. Additionally, the inverse kinematics of the parallel robot is simpler [29].

Due to the above features, the Stewart platform are widely used in industries application where the conventional serial robots have some limitations. In addition to the main application to flight simulators, the Stewart platform has been used for automotive, transportation, and machine tool technology, crane technology, underwater research, air-to-sea rescue, orthopedic surgery. It is also used for positioning of satellite communication dishes and telescopes and in applications such as shipbuilding and bridge construction [30]. In flight simulation, particularly in the so-called full flight simulator, all 6 degrees of freedom of the Stewart platform are required. In this role, the payload is a replica cockpit and a visual display system for showing the outside-world visual scene to the trained aircraft crew. The payload weights in the case of a full flight simulator for a large transport aircraft can be up to about 15,000 kilograms. The low impact docking system developed by NASA uses a Stewart platform to manipulate space vehicles during the docking process. The Taylor Spatial Frame, developed by Dr. J. Charles Taylor, is an external fixator used in orthopedic surgery for the correction of bone deformities and treatment of complex fractures. The RoboCrane is based on six cables and six winches configured as a Stewart platform. One version of the RoboCrane has been commercially developed for the Air Force to enable rapid paint stripping, inspection, and repainting of very large military aircraft such as the C-5 Galaxy. It has the capacity to lift and precisely manipulate heavy loads over large volumes with fine control in all six degrees of freedom [31].

However, there are some drawbacks of the parallel robot as well, such as small workspace, complex dynamic model, and complicated forward kinematic model [14, 32].

2.2.2 Kinematics of Parallel Robot

In general, the forward kinematics is relatively easy compared with the inverse kinematics in a serial-link manipulator. The situation is reversed in a parallel-link manipulator. It's very difficult to derive the forward kinematics of the parallel robot due to the structure of fully parallel mechanisms and closed-kinematic chains. Moreover, there might be multiple solutions to the forward kinematic equations [33, 34, 35]. On the other hand, its inverse kinematics is quite easy and has a unique solution.

[36] applies the conventional method of serial robots to the solution of inverse kinematics of parallel robots including the Stewart platform. [37] presents the inverse solutions of the parallel robots based on the screw theory. [38] proposes two inverse-kinematic solutions based on the damped least-squares method, where the first solution is derived using a velocity constraint, and the other uses a force constraint. [39] presents a straightforward inverse kinematic approach for a parallel robot with six translation movement legs.

The forward kinematics problem was the central topic in the research on the parallel robot during the late 1980s and early 1990s [14]. The main solutions to this problem are closed-form solutions of special cases, numerical schemes, and analytical approaches and so on. The closed-form solutions of special cases arise from the coalescence of some of the connection-points at the platform or the base or both in groups of two or three. [40] provides a decomposition method for the forward kinematics into two parts, one is a linear design-dependent part where particular geometries can be exploited and the other one is about the solution of certain nonlinear design-independent equations. The numerical schemes have computational advantages in most practical situations but are not suitable for a theoretical investigation to determine all the possible solutions. [41] presents a predictor-corrector algorithm using an efficient 3D search strategy for trapping the real solutions purely from geometrical considerations. As to analytical approaches, [42] reduces the kinematic equations into a univariate polynomial and established the upper bound of 40 solutions for the 6-6 Stewart platform with planar base and platform. [43] proposes a neural network solution for the forward kinematics of the parallel robot.

2.2.3 Workspace of Parallel Robot

The workspace, also called work volume or work envelope, is the volume of space which the end-effector of the robot can reach. The size and shape of the workspace depends on the coordinate geometry and the number of DOF of robots. The reachable workspace and the dexterous workspace are two important characteristics used in specifying the workspace of robots. The reachable workspace is the volume of the space in which the end-effector of the robot can reach in at least one orientation, while the dexterous workspace is the volume of space in which the end-effector of the robot can be arbitrarily oriented. Thus, the dexterous workspace is a subset of the reachable workspace [44].

One of the major disadvantages of parallel robot is the very limited and complicated workspace which is highly coupled entity. Hence, for the parallel robots with more than three DOF, there will be no possible graphical illustration of the robot workspace. In the academic community, different types of subsets of the complete workspace are usually determined and the most popular one is the constant-orientation workspace which is the three-dimensional volume that can be attained by a point of the upper platform while the platform is kept at a constant orientation [45, 46, 47]. Therefore, in order to get a good understanding of the parallel robot's complete workspace, a series of constant-orientation workspaces for various orientations have to be studied. As numerical methods, depending on the discretization step, give only an approximation of the shape of the workspace [32], the geometrical approaches are apparently more intuitive, fast and accurate to analyze the workspace of parallel robots. The constant-orientation workspace can be obtained by the intersection of six so-called vertex spaces and easily programmed in computer-aided design software such as Solidworks [48, 49, 50].

2.2.4 Singularities

A singularity occurs when the rank of the Jacobian drops below its maximum possible value, which is lesser than the number of variables of the robot. The Jacobian is the linear relation between the joint velocities and the end-effector velocity given by the matrix of partial derivatives, if variables in the robot are joint motions. When a robot passes near a singularity under Cartesian mode, speeds of some joints could suddenly become very large and the Cartesian velocity of the end-effector is significantly reduced. The movement might deviate from the desired path and result in an inability to track trajectories. Thus, singularities on the pre-planned trajectory which need to be avoided during the manufacturing process [51, 52].

Singularities analysis is one of the main concerns of designing parallel robots [53]. In order to avoid having the singularities inside the workspace, different algorithms were presented for the trajectory planning. [54] presents algorithms which enable to determine if there is any singularity within the 6 dimensions workspace of a Gough-type parallel robot expressed either in term of generalized coordinates or articular coordinates. [55] uses a variational approach to plan singularity-free paths for parallel robots based on a Lagrangian incorporating a kinetic energy term and a potential energy term. The kinetic energy term keeps the path short, and the potential energy term ensures that the obtained path is singularity-free and the actuator lengths remain within their

prescribed limits. [56] proposes three steps to perform an exhaustive determination of the singularity conditions of lower-mobility parallel manipulators with an articulated nacelle. Those steps are the acquisition of the twist graph and the wrench graph of the parallel manipulator, and the analysis of the superbracket to determine and interpret the parallel singularity conditions of the manipulator.

Research on singularities of the serial robot can date back to the 1960s at least. [57] identifies singularities as an obstruction to certain control algorithms requiring the construction of inverse kinematic solutions. [58] first describes singularities. [59] considers uncertainty configurations for single closed-loop mechanisms where the mechanism has an instantaneous increase in mobility. Subsequently, [60, 61, 62] link the idea to singular configurations of robot arms by considering a virtual rigid connection between the end-effector and the base. This idea was developed further in [63, 64, 65].

2.3 Cooperative Multiple Robots

With the development of the robotic technology, the modelling and control of cooperative multiple robots has been the subject of extensive research due to their versatility in the tasks as well as high productivity and potential of cost reduction in many industrial applications such as assembly, deburring, transportation, etc. These tasks might require dexterous manipulation, heavy load lifting or other technical demands, and sometimes are inadequate to be performed by a single robot [66, 67].

The motion of multiple robots can be divided into two types: unconstrained motion and constrained motion. The load of robots have no interaction with the environment in the unconstrained motion, which is usually referred to as motion in free space. The load is constrained by one or several constraint surfaces in the constrained motion [68]. The computed torque method is widely used to decouple the control loops corresponding to the position and the force in the unconstrained multiple robotic system [69, 70]. A set of nonlinear differential algebraic equations are normally used in the constrained multiple robotic system. Those equations describe both the positional information and the force developed between the constraint object and the end effectors of the robots.

A master-slave control scheme is proposed by [71]. The master arm is position controlled to follow a pre-planned trajectory while the slave arm is force controlled to keep a certain relative pose between the load and the master arm. [72] suggests the position control of each manipulator to follow a pre-planned object trajectory and manipulators are force controlled to exert forces on the object simultaneously so as to achieve a desired contact force. A master-slave scheme is developed based on linearized model of each robot by a nonlinear feedback in [73]. A weight matrix is introduced in a nonlinear feedback controller to guarantee the even distribution of the load among robots in [74]. Proportional-derivative (PD) feedback control law was applied in [75] at joint level, end-effector level, or the object's generalized coordinate level to control a dual-manipulator system. [76] presents a load distribution scheme for a dual-manipulator system to minimize either the energy consumption or the force exerted on the object. [77] derives the minimal constraints equations for a dual-manipulator system. The closed chain motion of manipulators and constraints are linearized around the rigid-body motion. The problem of two manipulators holding a complex load is discussed by [78]. A pseudo-velocity is introduced to reduce the order of the dynamics of the whole system based on the fact that the load and the manipulators form a closed kinematic chain. [79] proposes a nonlinear feedback control law and considered the influence of the constraint surface on the system dynamic model. The order of the system was reduced by introducing a pseudo-velocity which is defined as a linear combination of the joint velocities of the manipulators.

To deal with the uncertainties, several adaptive control approaches were proposed. For the free object controlling, [80] presents an adaptive control scheme for the multi-robot system to ensure the asymptotic convergence of the load position to the desired values and the boundedness of the internal forces. [81] proposes an adaptive controller for the coordinated motion control of two manipulators handling an object of unknown mass. [82] develops a model-based adaptive controller and a model-free neural-network-based adaptive controller to control the positions of the constrained object and the end effectors and guarantee the asymptotic tracking of the constraint object and the boundedness of the constraint force. [83] derives the adaptive control algorithms which approximate the system's dynamics using a continuous online estimation of a set of the plant's physical parameters through well-defined adaptation laws. [67] develops a hybrid knowledge-based adaptive tracking controller for a multi-robots system to manipulate a common

object. [84, 85] propose adaptive fuzzy logic systems which are theoretically capable of uniformly approximating any continuous real function to any degree of accuracy.

Apart from the benefits of multiple robots, challenges including trajectory planning, collision avoidance, simultaneous programming and other issues become more complex as the number of robots in the systems is increased [86]. Centralized algorithms are employed to plan the path for each robot in multiple mobile robotic system. [87] implements a single robot with collision avoidance support in troublesome scenarios using the nearness diagram navigation algorithm. Such collision avoidance strategies must rely on sensory information to compute the movement according to unforeseen circumstances. [88] applies a fuzzy reasoning based on a Step-Forward motion strategy to make decision on motion of multiple robots. [89] computes collision-free optimal trajectories by incorporating the computation of inter-object separation distances into the manipulator optimal control problem as minimization sub-problems through the use of Karush-Kuhn-Tucker multipliers. The multiple manipulators trajectory planning involved static and dynamic obstacles in which each robot acts as a dynamic obstacle that the other should avoid. [90] also presents a fuzzy genetic algorithm approach to tackle the problem of trajectory planning of two manipulators sharing a common workspace. [91] proposes an algorithm which is capable of generating dual-arm collision-free trajectories in real-time despite the fact that the initial configurations of two arms are not synchronized. [92] presents a collision-free approach for path planning of robot manipulators. The robot react to moving obstacles using a local and reactive algorithm restricted to a subset of its configuration space. The lack of a long-term view of local algorithms is solved by choosing the subset of the configuration space that maximizes the probability of finding collision-free paths on off-line pre-planning stage. However, few papers regarding the on-line collision avoidance with off-line pre-planned trajectories of multiple robots were found during literature review.

2.4 Trajectory Planning of AFP Machine

In addition to the problem of avoiding collisions in multiple robot systems mentioned above, robotic trajectory planning also involves solving joint motion and control profiles that maximize performance, subject to kinematic, dynamic and control constraints [80, 93]. Moreover, singularities need to be predicated and avoided during the trajectory planning process [94]. [95]

presents a singularity-robust trajectory generation algorithm that takes a specific path and a corresponding kinematic solution as input to produces a feasible trajectory in the presence of kinematic singularities. To plan the optimal trajectory, singularity avoidance is not the only criterion to be considered. [96] proposes an elitist non-dominated sorting genetic algorithm and differential evolution to optimal trajectory planning of an industrial robot manipulator by considering payload constraints. The multi-criterion cost function is a weighted balance of singularity avoidance, transfer time, total energy involved in the motion, joint jerks, and joint accelerations.

As to trajectory planning of fiber placement process, more requirements have to be taken into consideration to avoid unfeasible laminates. The minimum turning radius, namely the curvature constraint, is one of the major limitations. The tows at the inner radius might wrinkle if the turning radius is too small in the process of steering, which could cause a reduced quality of the laminate [97, 98, 99]. Moreover, certain defects, mainly gaps and/or overlaps, often appear in the final part that affecting the structural performance. Several papers investigated the effect of the area percentage of gaps and overlaps on the structural performance of components manufactured by AFP machine. [98] proposes defect layer method to characterize the change in properties of each layer in the composite laminates that results from the occurrence of gaps and overlaps. The results show that the buckling load improvement resulting from fiber steering reduces by 15% compared to the laminate where gaps are ignored. A maximum improvement of 71% in the buckling load over the quasi-isotropic laminates can be observed for a variable stiffness laminate built with a complete overlap strategy. [100] observes the strength reductions of 5-27% in laminates containing overlaps and gaps at least 0.03 inches wide. [101] shows the introducing gaps reduces the average strain. [102] works on the effect of four principal defect types, namely gap, overlap, half gap/overlap and twisted tow on the ultimate strengths. It presented that the overlaps can result in strength increasing of maximum 13% compared to a non-defective laminate. [103] investigates the influence of tow-drop areas on the strength and stiffness of variable-stiffness laminates. The effects of tow width, laminate thickness and staggering in combination with tow-drop areas are studied by making use of finite element simulations. It also presented a method to localize the tow-drop areas. [104] presents that laminates with curvilinear fiber topology, mainly the ones in which fiber tows are allowed to overlap, have up to 56% higher strength than straight fiber laminates and remarkable improvements on the retardation of damage initiation.

A number of trajectory planning methods for fiber placement have been developed. In [6], the surface-curve algorithm which formulates a set of paths on an open-contoured surface is developed. [7, 9] propose a recursive numerical algorithm for the creation of trajectories on an arbitrary B-spline surface. [97] presents the derivation of four theoretical fiber path definitions for generalized conical shell surfaces, namely a geodesic path, a constant angle path, a linearly varying angle path, and a constant curvature path. [105] proposes the Fast Marching Method to define equidistant courses over surfaces of general geometry. [106] introduces a level set method to optimize the continuously varying fiber paths for AFP machine. The paths of the fibers are defined by constant level set function values, describing a series of continuous equally spaced fiber paths. [107] presents a methodology for the optimum design of laminated composites with curved fiber courses. Layer thicknesses and fiber angles are represented by bicubic Bezier surfaces and cubic Bezier curves respectively. [108] optimizes the buckling load of a cylinder in pure bending by using a multiple-segment constant curvature fiber angle variation in circumferential direction, while taking into account manufacturing constraints. The approach in [109] is to consider a reference curve over the draping surface and to compute the set of points over the surface which are at a constant distance from the reference curve. However, to my best knowledge, no papers of trajectory planning for fiber placement which took the robot mounted with fiber process head into consideration are found.

2.5 Pose Tracking

Even though methods such as kinematics calibration are effective to improve the accuracy of robots, the kinematics model used in the robot controller cannot accurately describe the kinematics relation of the actual robot due to both the geometric and non-geometric errors, which will result in positioning inaccuracy. Moreover, the kinematics parameter errors in the calibration often change with the load or environment variation [110]. Therefore, the independent measurement of end-effector's poses of both robots in multiple robots system on-line is indispensable to achieve the precise positioning and controlling, as well as collision or singularity avoidance in some applications.

Recently, pose trackers have widely been implemented in robotic applications. Laser tracking systems that combine laser interferometry and photogrammetry is one approach to determine the

pose of a robot's end-effector with high accuracy [111, 112]. However, the laser-based methods require a large and open space, and the laser beam is easily sheltered during the motion [113]. Pure photogrammetric solution is able to track the robots pose accurately by using industrial standard cameras at low cost [114]. Compared to image-based photogrammetric techniques which are more computationally intensive, feature-based methods is easier to achieve real-time performance by using only a subset of the data [115]. [116, 117] use model-based techniques that rely on tracking features such as points and lines. [114] presents a 3D-model-based computer-vision method for tracking the full six DOF pose of a rigid body in real time via a combination of the textured model projection and the optical flow. [118] investigates the two fundamental photogrammetric algorithms: intersection and resection. The collinearity equation is used to measure the camera pose (exterior orientation) with respect to the target co-ordinate system directly in the first approach. The stereo-camera measures the position of the observed targets with respect to the camera coordinate system in the second approach.

Visual servoing is the main and effective approach. Generally, the visual servoing, based on the visual measurement feedback of the reference objects, can be classified into three main categories which are image-based visual servoing [119, 120, 121], position-based visual servoing [122, 123], and hybrid visual servoing [124, 125]. Errors between the initial and desired poses of the feature points on the image plane are calculated, and the feature points are controlled to move to the desired positions on the image plane in image-based visual servoing [121]. But, most of this schemes might fail to have a robotic manipulator perform positioning tasks with large displacements between the initial and desired poses. Moreover, image singularities and image local minima might be existed due to the form of image Jacobian [126]. However, image-based visual servoing is more suitable for preventing the feature points from leaving the field of view since the feature points are controlled directly on the image plane. And it is more robust with respect to the uncertainties in intrinsic and extrinsic parameters of the camera [127]. By contrast, errors between the initial and the desired poses in the three-dimensional workspace are computed for the positioning task of a robot in position-based visual servoing [123]. Therefore, position-based visual servoing is more suitable for position or velocity control in the joint space or in the three-dimensional workspace of the industrial robots [128]. Moreover, there are no control problems associated with image singularities, image local minima, large displacement between the initial and the desired poses, and unnatural camera motion in the three-dimensional workspace [122].

Hybrid visual servoing combines the first two approaches. [124] proposes a hybrid motion control strategy consists of a local switching control between the image-based and position-based visual servoing for direct avoidance of image singularities and image local minima. According to the location of the vision instrument, the configuration of visual seroving can be classified into eye-to-hand and eye-in-hand.

A set of photographs taken from different viewing angles are used to measure an object in three dimensions, which is known as bundle adjustment and is used in optical measuring applications in the early 1960s. The principle of bundle adjustment consists of accurately measuring a scene structure using a sequence of images acquired by a camera or a series of cameras [129].

The photogrammetry sensor using image-based triangulation are constituted of an optical tracking system equipped with video cameras. There are two categories, namely those based on matrix array cameras, which use retroreflective targets or LEDS as targets, and those with linear array cameras, which systematically use LEDs as targets. Retroreflective targets are used in C-track [129].

Photogrammetry employs three main calculation steps to implement their dynamic referencing and optical measurement functionalities:

- Image-processing step to accurately assess target image projections in the photogrammetry sensor images;
- Triangulation step to estimate the target coordinates ($x \quad y \quad z$) with respect to the sensor reference from their projections in the twin images of the photogrammetry sensor;
- The last step to estimate the pose of a modeled object using a set of points whose nominal coordinates are known and observed by the photogrammetry sensor.

The cameras can be modelled using perspective projections and other parameters that take into account geometric aberrations generated by the imager, commonly known as radial and tangential distortions. Identification of these so-called intrinsic parameters occurs during a previous calibration step. The approach used to calibrate the imagers is based on techniques used in photogrammetry [130].

To my best knowledge, no papers regarding on-line singularity avoidance for fiber placement using multiple robots are found.

2.6 Summary

In this chapter, different kinds of AFP machines in the current industrial market are introduced at first. Reviews regarding the kinematics, workspace and singularities of the parallel robot are presented. The kinematic analysis includes the inverse kinematic and the forward kinematic. Several numerical and geometrical approaches are used in the workspace analysis of the parallel robot, where constant-orientation workspaces are normally applied. Due to the fact that analysis of the serial robot is well studied, reviews on the serial robot are not focused in this dissertation. Then, the relevant studies of the multiple robots are given. Many control algorithms are proposed to cooperative control the multiple robots system. In addition to the collision avoidance and singularity avoidance, more requirements are needed to be considered for the trajectory planning of fiber placement, such as the minimum turning radius, gaps and/or overlaps, etc. At last, methods of pose tracking are introduced. The three main calculation steps employed by photogrammetry sensor to track pose are presented. However, no papers regarding the manipulation of both robots in the path planning of AFP machine are found.

CHAPTER 3

3 KINEMATICS ANALYSIS AND SIMULATION OF THE COOPERATIVE AFP SYSTEM

3.1 Introduction

Instead of using two open-loop serial manipulators, the cooperative AFP system with one 6-DOF serial robot and one 6-DOF parallel robot is proposed due to the requirements of heavy load bearing and the precise positioning capability. The mechanism of the parallel robot is built with closed-loop kinematic chains which consist of several links connected by joints.

In this chapter, the inverse kinematics of both parallel robot and serial robot included in the cooperative AFP system will be presented. And a numerical forward kinematic method, called quasi-Gough forward kinematic algorithm, will be given to determine the uniqueness of forward kinematic solution for the parallel robot. Then, simulation using SimMechanics is conducted for fiber placement of the bowl shape mandrel.

3.2 Kinematics of the Parallel Robot

3.2.1 Inverse Kinematics of the Parallel Robot

The structure of the parallel robot is 6-RSS mechanism as shown in Figure 3.1. The 6-RSS parallel robot contains six identical kinematic chains connecting the base and the moving platform. Each connecting chain is composed of one horizontal revolute joint mounted on the base and two spherical joints.

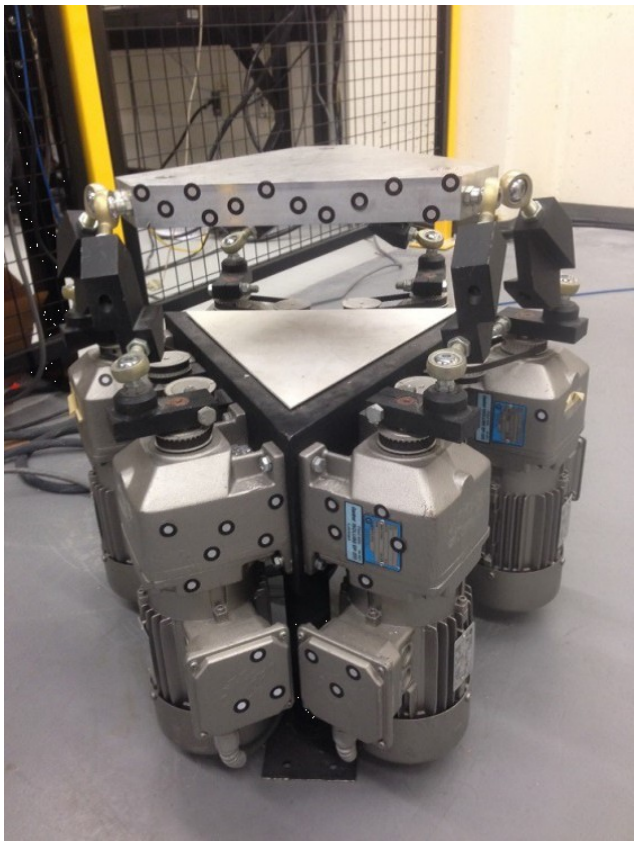

Figure 3.1. 6-RSS Parallel Robot

The inverse kinematics is commonly used for trajectory generation, as studied in [25, 29, 131]. The process of the inverse kinematics for the 6-RSS parallel robot is the mapping from the position and orientation of the end effect to the actuator angles, referring to the mechanism shown in Figure 3.2.

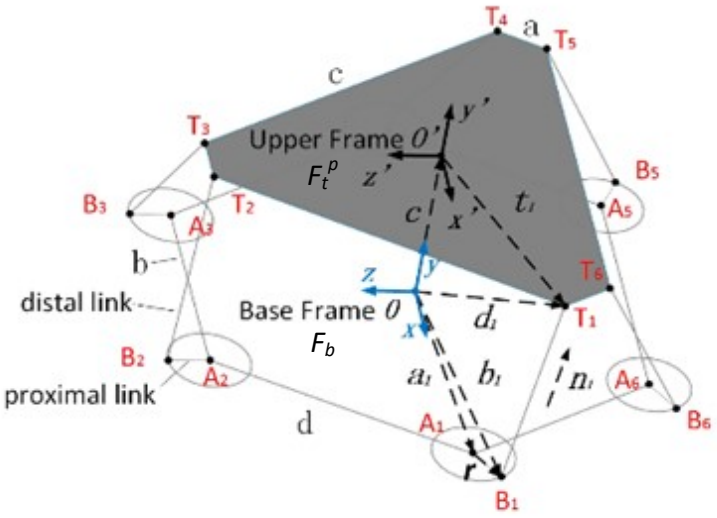

Figure 3.2. 6-RSS Parallel Robot Mechanism

The end of each proximal link in the identical kinematic chain is connected to one of the six vertices of the base, which is denoted as point A_i. The coordinates of these points $A_i^b(X_{A_i} \quad Y_{A_i} \quad Z_{A_i})$ in terms of the base frameF_b are fixed and the values are shown in Eq. (3-1).

$$\begin{cases} A_1^b(X_{A_1} \quad Y_{A_1} \quad Z_{A_1}) = [1/2(b+d) \quad 0 \quad -\sqrt{3}/6(b-d)] \\ A_2^b(X_{A_2} \quad Y_{A_2} \quad Z_{A_2}) = [1/2b \quad 0 \quad \sqrt{3}/6(b+2d)] \\ A_3^b(X_{A_3} \quad Y_{A_3} \quad Z_{A_3}) = [-1/2b \quad 0 \quad -\sqrt{3}/6(b+2d)] \\ A_4^b(X_{A_4} \quad Y_{A_4} \quad Z_{A_4}) = [-1/2(b+d) \quad 0 \quad -\sqrt{3}/6(b-d)] \\ A_5^b(X_{A_5} \quad Y_{A_5} \quad Z_{A_5}) = [-1/2d \quad 0 \quad \sqrt{3}/6(2b+d)] \\ A_6^b(X_{A_6} \quad Y_{A_6} \quad Z_{A_6}) = [1/2d \quad 0 \quad \sqrt{3}/6(2b+d)] \end{cases} \quad (3\text{-}1)$$

where b and d are the side lengths of the base semi-regular hexagon. The vectors along line OA_i are denoted as $\boldsymbol{a}_i$.

The lengths of all proximal links are equal and denoted by r and the vector $\boldsymbol{r}$ is defined as $\boldsymbol{r} = r[\cos\theta_i \quad 0 \quad \sin\theta_i]^T$. The connected points of the distal links and the proximal links are referred as B_i, as shown in the single RSS kinematic chain Figure 3.3.

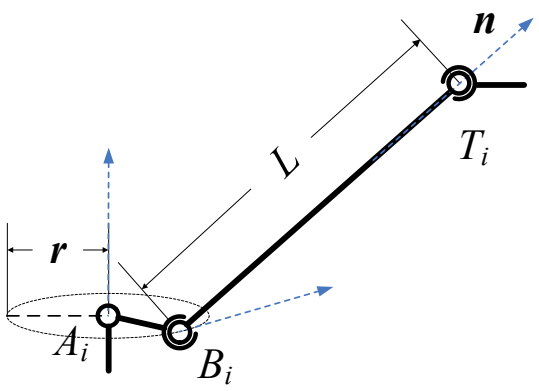

Figure 3.3. Single RSS Kinematic Chain of the Parallel Robot

The horizontal rotational angles θ_i are controlled by the motors at revolute joints. The vectors along line OB_i in terms of the base frame F_b are denoted by $\boldsymbol{b}_i$, shown in Eq. (3-2).

$$\boldsymbol{b}_i = \boldsymbol{a}_i + r[\cos\theta_i \quad 0 \quad \sin\theta_i]^T \tag{3-2}$$

Then the top ends of the distal links in the connecting chains are connected to the six vertices of the upper platform, which are denoted as points T_i . The coordinates of these points $T_i^p(x_{T_i} \quad y_{T_i} \quad z_{T_i})$ with respect to the upper frame F_t^p are fixed, shown in Eq. (3-3).

$$\begin{cases} T_1^p(x_{T_1} \quad y_{T_1} \quad z_{T_1}) = [1/2(a+c) \quad 0 \quad \sqrt{3}/6(a-c)] \\ T_2^p(x_{T_2} \quad y_{T_2} \quad z_{T_2}) = [1/2c \quad 0 \quad -\sqrt{3}/6(2a+c)] \\ T_3^p(x_{T_3} \quad y_{T_3} \quad z_{T_3}) = [-1/2c \quad 0 \quad -\sqrt{3}/6(2a+c)] \\ T_4^p(x_{T_4} \quad y_{T_4} \quad z_{T_4}) = [-1/2(a+c) \quad 0 \quad \sqrt{3}/6(a-c)] \\ T_5^p(x_{T_5} \quad y_{T_5} \quad z_{T_5}) = [-1/2a \quad 0 \quad \sqrt{3}/6(a+2c)] \\ T_6^p(x_{T_6} \quad y_{T_6} \quad z_{T_6}) = [1/2a \quad 0 \quad \sqrt{3}/6(a+2c)] \end{cases} \tag{3-3}$$

where a and c are the side lengths of the top semi-regular hexagon. The vectors along line $O'T_i$ are denoted as $\boldsymbol{t}_i$ with respect to the upper platform. These coordinates vary in terms of the base frame when the platform moves. The position of the upper platform with respect to the base frame is defined by vector $\boldsymbol{c}$, along the line OO'. The vectors along lines OT_i are denoted by $\boldsymbol{d}_i = \boldsymbol{c} + \boldsymbol{R}\boldsymbol{t}_i$, which are the coordinates of all vertices of the upper platform with reference to the base frame $T_i^b(X_{T_i} \quad Y_{T_i} \quad Z_{T_i})$. The transformation matrix $\boldsymbol{R}$, defined by three Euler angles, describes the orientation of the upper platform.

The unit vector along distal links L are denoted by $\boldsymbol{n}_i$, which is

$$L\boldsymbol{n}_i = \boldsymbol{c} + \boldsymbol{R}\boldsymbol{t}_i - \boldsymbol{a}_i - \boldsymbol{r} \quad (3\text{-}4)$$

By taking the square of both sides of Eq. (3-4), one has

$$L^2 = (\boldsymbol{c} + \boldsymbol{R}\boldsymbol{t}_i - \boldsymbol{a}_i - \boldsymbol{r})^T(\boldsymbol{c} + \boldsymbol{R}\boldsymbol{t}_i - \boldsymbol{a}_i - \boldsymbol{r}) \quad (3\text{-}5)$$

and

$$L^2 = \|\boldsymbol{d}_i - \boldsymbol{a}_i\|^2 + \mathrm{r}^2 - 2(\boldsymbol{d}_i - \boldsymbol{a}_i)^T\boldsymbol{r} \quad (3\text{-}6)$$

from the vector $\boldsymbol{r}$ and the vertices coordinates of points A_i and T_i with reference to the base frame, Eq. (3-6) reduces to

$$\left(X_{T_i} - X_{A_i}\right)\cos\theta_i + \left(Z_{T_i} - Z_{A_i}\right)\sin\theta_i = \frac{\|\boldsymbol{d}_i - \boldsymbol{a}_i\|^2 + \mathrm{r}^2 - L^2}{2} \quad (3\text{-}7)$$

and

$$\sin\theta_i = \frac{p_i z_i \pm x_i\sqrt{{x_i}^2 + {z_i}^2 - {p_i}^2}}{{x_i}^2 + {z_i}^2} = \gamma_i \quad (3\text{-}8)$$

$$\cos\theta_i = \frac{p_i x_i \mp z_i\sqrt{{x_i}^2 + {z_i}^2 - {p_i}^2}}{{x_i}^2 + {z_i}^2} = \rho_i \quad (3\text{-}9)$$

$$\theta_i = a\tan 2(\gamma_i, \rho_i) \quad (3\text{-}10)$$

where $x_i = X_{T_i} - X_{A_i}$, $z_i = Z_{T_i} - Z_{A_i}$, and $p_i = \frac{\|\boldsymbol{d}_i - \boldsymbol{a}_i\|^2 + \mathrm{r}^2 - L^2}{2r}$. The inequality ${x_i}^2 + {z_i}^2 - {p_i}^2 \geq 0$ holds. And $\theta_i \in [-\pi, \pi]$ is the solution to the inverse kinematics [25].

3.2.2 Forward Kinematics of the Parallel Robot

In this research, a quasi-Gough forward kinematic algorithm is presented to determine the uniqueness of forward kinematic solution of the 6-RSS parallel robot by numerical verification. Normally, numerical forward kinematic methods like Newton-Raphson method[132], Jacobi method[133] and Powell method[134] can achieve high accuracy in the parallel robot analysis with

small workspace, which means the initial pose is not far from the final result. For each group of the known actuator angles θ_i, the position of B_i are fixed. Then a quasi-Gough mechanism is obtained, which can be deformed into a general Gough platform by mechanism deformation. As the distance between B_i and T_i keep the same, the input leg lengths for the quasi-Gough mechanism are kept as $\boldsymbol{L}_{BT}$ $(L_{B_1T_1}, L_{B_2T_2}, \dots, L_{B_6T_6})$. The quasi-Gough forward kinematic algorithm is given as follows.

1) Input the desire actuators angles θ_i, and calculate the corresponding B_i $(i = 1, 2, \dots, 6)$ for the quasi-Gough platform. Then, choose the initial pose $\boldsymbol{p}$ based on initial status of the end-effector. Set the condition coefficient ε_c for the iterated result accuracy, set the penalty coefficient ε_p for position correction.

2) Calculate a pose correction $\Delta\boldsymbol{p}$ through multiple algorithms based on $\Delta\boldsymbol{L} = \boldsymbol{L}_{BT} - f(\boldsymbol{p})$, where $f(\boldsymbol{p})$ denotes the inverse kinematic equations.

3) If $\left\|f_p(\boldsymbol{p}, \Delta\boldsymbol{p})\right\|_* \leq \varepsilon_p$, then $\boldsymbol{p} = \boldsymbol{p} + \Delta\boldsymbol{p}$; else, back to 2 for a new $\Delta\boldsymbol{p}$.

4) If $\|f_c(\boldsymbol{p}, \boldsymbol{L}_{BT})\|_* \leq \varepsilon_c$, then output the present $\boldsymbol{p}$ as the result; else ,back to 2 for a new iteration.

where $\| \ \|_*$denotes norms in corresponding parameter space.

Figure 3.4 and Figure 3.5 show the procedures of the two kinds of forward kinematic method. The solid lines are the initial status of the 6-RSS parallel robot, and the dotted lines are the final status for the direct kinematic solutions. In Figure 3.4, the numerical iteration steps are limited by penalty coefficient ε_p (or the iteration may convergence into wrong solution), and all the sketches in the procedure can be realized by the real parallel robot. In Figure 3.5, the convergence is faster than the previous one, but the procedure cannot be realized by the real 6-RSS parallel robot because the "virtual lengths" B_iT_i are not equal to $L_{B_iT_i}$ [135].

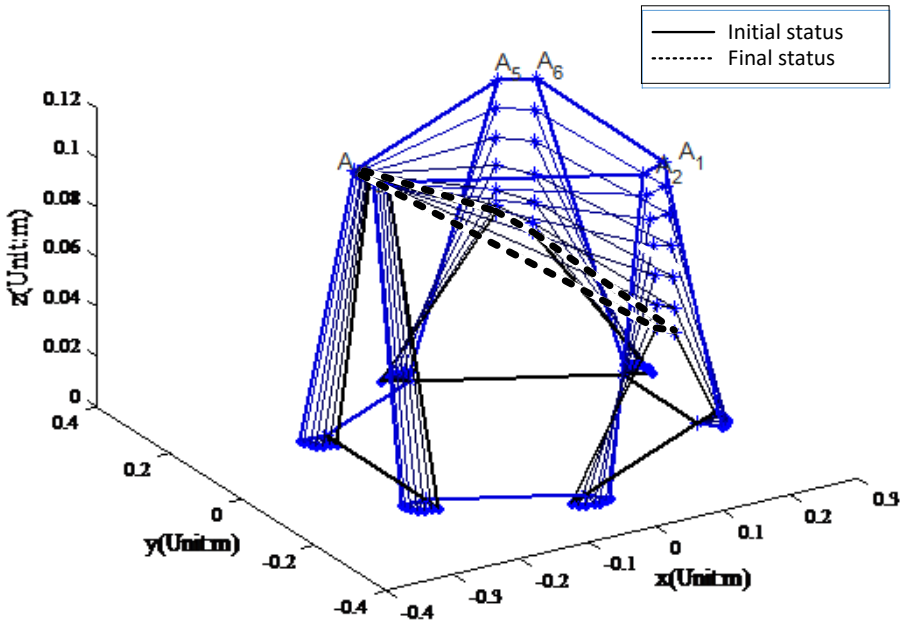

Figure 3.4. Procedure of the Normal Forward Kinematic Method

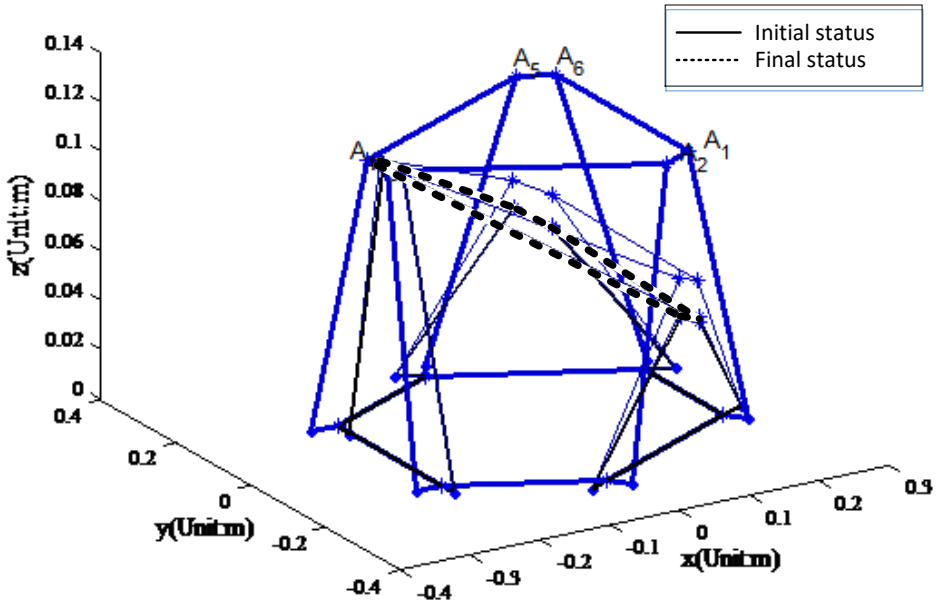

Figure 3.5. Procedure of the Quasi-Gough Method

3.3 Kinematics of the Serial Robot

Kinematical analysis of the serial robot has been well studied. Before operating experiments on real robots, simulation models are built for this project at first. The serial robot used in the simulation is Denso 6-Axis robot, model VP6242G, supplied with Quanser open-architecture control module which has all capabilities of an industrial system and is interfaced with QUARC. The reason of using Denso in the simulation as the serial robot is because there is no Fanuc robot in the lab at that time. The structure of the serial robot is shown in Figure 3.6.

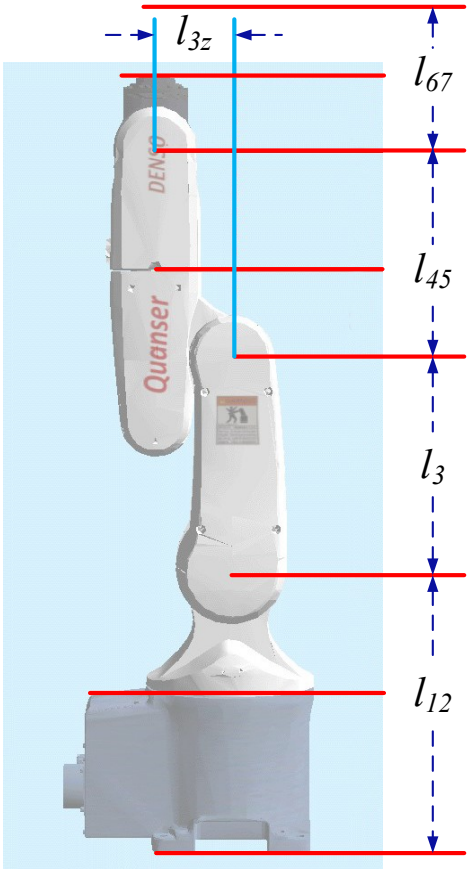

Figure 3.6. Structure of Denso Robot

where l_{12} represents the length from the axis 2 to the surface of the base; l_3 is the length between axis 2 and axis 3; l_{3z} is the distance between axis 3 and axis 4; l_{45} denotes the length from the axis 3 to the axis 5; l_{67} is the distance from the end point of the end-effector to the axis 5.

The Denavit–Hartenberg (D-H) table, which presents the four parameters associated with a particular convention for attaching reference frames to the links of robot manipulator, is shown as following.

Table 3-1. D-H Parameters of Denso

D-H	$\boldsymbol{\alpha_{i-1}}$	$\boldsymbol{a_{i-1}}$	$\boldsymbol{d_i}$	$\boldsymbol{\theta_i}$
1	0	0	0	θ_1
2	$-90°$	0	0	$\theta_2 - 90°$
3	0	l_3	0	θ_3
4	$-90°$	l_{3z}	l_{45}	θ_4
5	$90°$	0	0	θ_5
6	$-90°$	0	0	θ_6

where $l_{12} = 280\ mm$, $l_3 = 210\ mm$, $l_{3z} = 75\ mm$, $l_{45} = 210\ mm$, $l_{67} = 104\ mm$.

The inverse kinematic of the 6-DOF serial robot is the mapping from the pose of the end-effect to the six actuator angles, which means the pose of the end-effector $\begin{bmatrix} r_{11} & r_{12} & r_{13} & p_x \\ r_{21} & r_{22} & r_{23} & p_y \\ r_{31} & r_{32} & r_{33} & p_z \\ 0 & 0 & 0 & 1 \end{bmatrix}$ is given.

The process of the inverse kinematic for Denso robot is shown as follow.

1) The solution of the first angle θ_1 is,

$$\theta_1 = Atan2(p_y, p_x) \quad (3\text{-}11)$$

another solution is $\theta_1 = Atan2(-p_y, -p_x)$.

2) The solution of the third angle θ_3 is,

$$\theta_3 = Atan2(l_{3z}, l_{45}) - Atan2\left(K, \pm\sqrt{{l_{3z}}^2 + {l_{45}}^2 - K^2}\right) \quad (3\text{-}12)$$

where $K = \frac{{p_x}^2 + {p_y}^2 + {p_z}^2 - {l_3}^2 - {l_{3z}}^2 - {l_{45}}^2}{2 \times {l_3}^2}$.

3) Based on the results of the third angle θ_3, the solution of the second angle θ_2 can be derived as,

$$\theta_2 = Atan2\Big((-l_{3z} - l_3 \times c\theta_3) \times p_z - \big(c\theta_1 \times p_x + s\theta_1 \times p_y\big) \times (l_{45} - l_3 \times s\theta_3), (l_3 \times s\theta_3 - l_{45}) \times p_z + (l_{3z} + l_3 \times c\theta_3) \times \big(c\theta_1 \times p_x + s\theta_1 \times p_y\big)\Big) - \theta_3 \quad (3\text{-}13)$$

where $c\theta = \cos(\theta)$, $s\theta = \sin(\theta)$.

4) The solution of the fourth angle θ_4 can be obtained by,

$$\theta_4 = Atan2\big(-r_{13} \times s\theta_1 + r_{23} \times c\theta_1, -r_{13} \times c\theta_1 \times c(\theta_2 + \theta_3) - r_{23} \times s\theta_1 \times c(\theta_2 + \theta_3) + r_{33} \times s(\theta_2 + \theta_3)\big) \quad (3\text{-}14)$$

where $c(\theta_2 + \theta_3) = cos(\theta_2 + \theta_3)$ and $s(\theta_2 + \theta_3) = sin(\theta_2 + \theta_3)$.

5) The solution of the fifth angle θ_5 can be derived as follow,

$$s\theta_5 = r_{33} \times s(\theta_2 + \theta_3) \times c\theta_4 - r_{13} \times (c\theta_1 \times c(\theta_2 + \theta_3) \times c\theta_4 + s\theta_1 \times s\theta_4) - r_{23} \times (s\theta_1 \times c(\theta_2 + \theta_3) \times c\theta_4 - c\theta_1 \times s\theta_4) \quad (3\text{-}15)$$

$$c\theta_5 = r_{13} \times \big(-c\theta_1 \times s(\theta_2 + \theta_3)\big) + r_{23} \times \big(-s\theta_1 \times s(\theta_2 + \theta_3)\big) - r_{33} \times c(\theta_2 + \theta_3) \quad (3\text{-}16)$$

$$\theta_5 = Atan2(s\theta_5, c\theta_5) \quad (3\text{-}17)$$

6) The solution of the sixth angle θ_6 is,

$$s\theta_6 = r_{11} \times (c\theta_1 \times c(\theta_2 + \theta_3) \times s\theta_4 - s\theta_1 \times c\theta_4) - r_{21} \times (s\theta_1 \times c(\theta_2 + \theta_3) \times s\theta_4 + c\theta_1 \times c\theta_4) + r_{31} \times s(\theta_2 + \theta_3) \times s\theta_4 \quad (3\text{-}18)$$

$$
\begin{aligned}
c\theta_6 = r_{11} \times \big(& (c\theta_1 \times c(\theta_2+\theta_3) \times c\theta_4 + s\theta_1 \times s\theta_4) \times c\theta_5 - c\theta_1 \\
& \times s(\theta_2+\theta_3) \times s\theta_5 \big) + r_{21} \\
& \times \big((s\theta_1 \times c(\theta_2+\theta_3) \times c\theta_4 - c\theta_1 \times s\theta_4) \times c\theta_5 \\
& - s\theta_1 \times s(\theta_2+\theta_3) \times s\theta_5 \big) - r_{31} \\
& \times (s(\theta_2+\theta_3) \times c\theta_4 \times c\theta_5 + c(\theta_2+\theta_3) \times s\theta_5)
\end{aligned}
\tag{3-19}
$$

$$
\theta_6 = Atan2(s\theta_6, c\theta_6) \tag{3-20}
$$

There are multiple solutions to the inverse kinematics of a serial-link manipulator. The shortest distance rule is used to choose a solution closest to the current manipulator [136], shown in Eq. (3-21).

$$
\theta = min \sum_{i=1}^{6} \sqrt{(\theta_{ni} - \theta_i)^2}, \quad n=1,2,\ldots,8 \tag{3-21}
$$

where θ_i is the rotational angle of the i joint, θ_{ni} is the n solution.

With the desired pose of the serial robot, the angle of actuators can be calculated using the above equations and imported into the SimMechanics model under Matlab.

Similarly, the kinematic model of Fanuc M20-iA is obtained by using the D-H parameters. Its D-H parameters are shown in Table 3-2.

Table 3-2. D-H Parameters of Fanuc M20-iA

D-H	$\boldsymbol{\alpha_{i-1}}$	$\boldsymbol{a_{i-1}}$	$\boldsymbol{d_i}$	$\boldsymbol{\theta_i}$
1	0	0	525	θ_1
2	-90°	150	0	θ_2
3	0	790	0	θ_3
4	−90°	250	835	θ_4
5	90°	0	0	θ_5
6	−90°	0	100	θ_6

3.4 Simulation in SimMechanics

Before carrying out experiments using the cooperative AFP system, the simulation in SimMechanics (Simscape Multibody nowadays) is conducted at first. SimMechanics software is a block diagram modeling environment for the engineering design and simulation of rigid body machines and their motions, which interfaces seamlessly with Simulink and MATLAB. Multibody systems can be modelled using blocks representing bodies, joints, constraints, force elements and sensors. The visualization tools of SimMechanics software display and animate simplified standard geometries of 3 dimension machines, before and during simulation. CAD assemblies including all masses, inertias, joints, constraints and 3 dimension geometry can be imported into SimMechanics model directly [137]. Kinematics and dynamics simulation can be executed in SimMechanics without deducing mechanism model [138].

The serial robot used in this simulation is Denso 6-Axis robot, model VP6242G.

3.4.1 Modelling of the Cooperative AFP system in SimMechanics

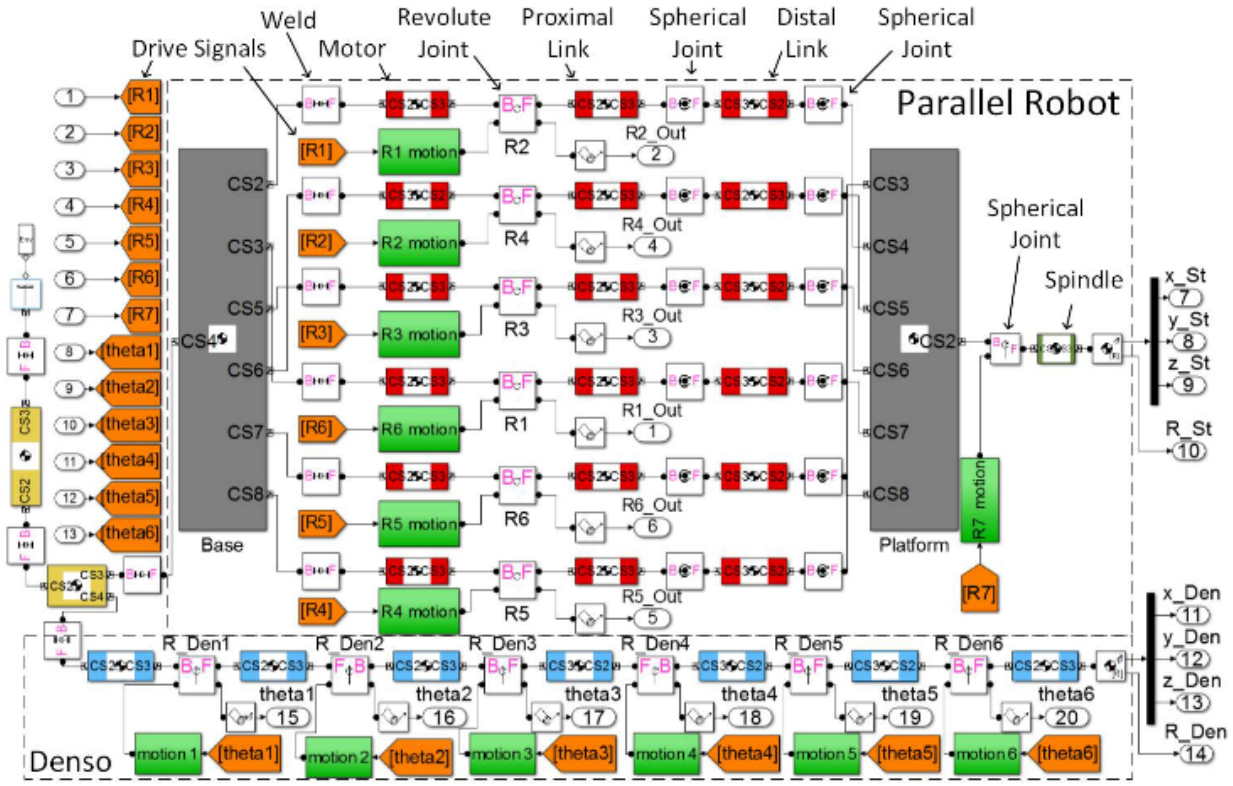

Figure 3.7. Modelling of the Cooperative AFP System in SimMechanics

Figure 3.7 shows the detail modelling of the cooperative AFP system in SimMechanics. The top part is the SimMechanics model of the parallel robot. The six identical kinematic chains connect the base and the moving platform. In each connecting chain, the proximal link is connected to the base by a revolute joint. The ends of the distal link are connected the proximal link and the moving platform by two spherical joints. Six drive signals are input to the actuator port of the six revolute joints. In addition, a spindle is mounted on the platform, connected by a revolute joint, to hold the mandrel. The bottom part of the figure shows the SimMechanics model of Denso Robot. Six revolute joints containing drive signals connect seven components including the end effector. The bases of the Stewart platform model and Denso Robot model are welded together. The positions and orientations of the two end effectors of the parallel platform and the serial robot are measured by the sensor, which is C-Track, and output for further simulation.

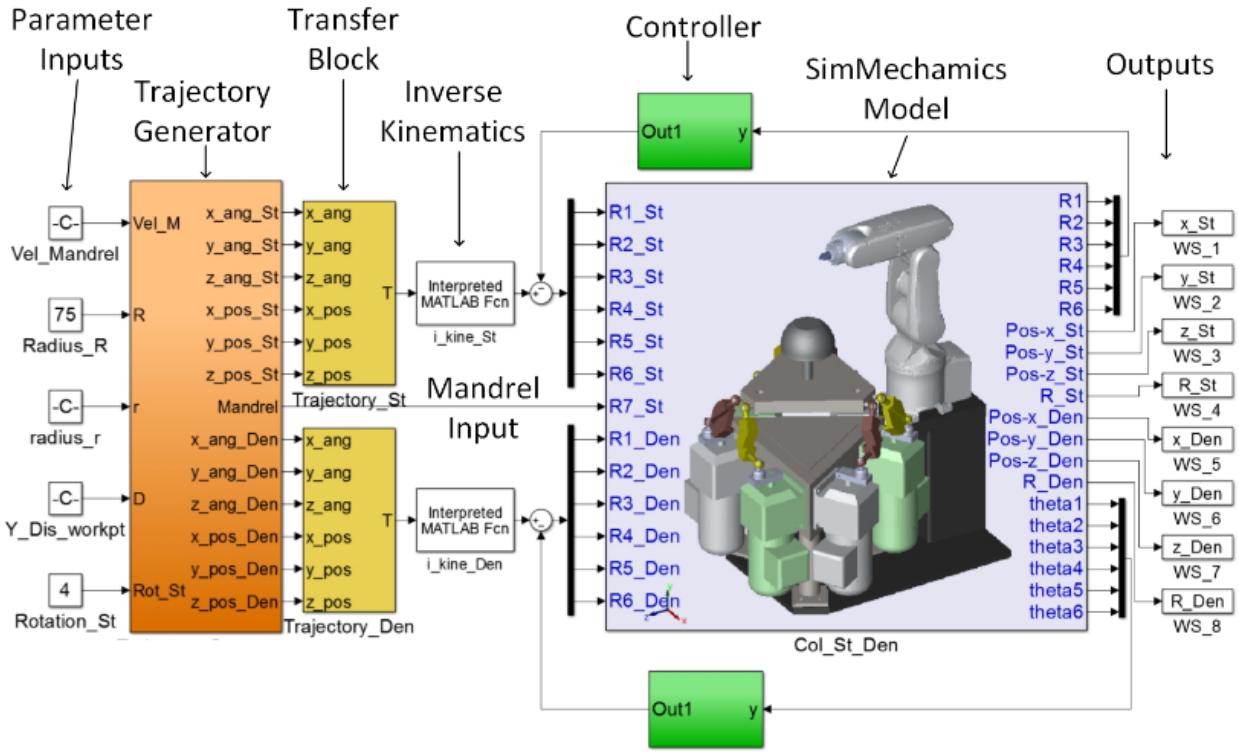

Figure 3.8. Simulation Model with Trajectory Planning

Figure 3.8 shows the simulation model with off-line trajectory planning in SimMechanics. At the left side of the diagram block, with the parameter inputs, the block “Trajectory Generator” generates the desired positions and orientations of the working frames for both parallel robot and

Denso robot, as well as the desired rotation of mandrel. Then, the desired positions and orientations are transferred to matrix. With the inputs of the matrices, the corresponding values for actuators of each leg and the rotary stage are calculated by the inverse kinematics blocks. And the movements in the SimMechanics is actuated based on such values. In the SimMechanics model, the positions and orientations of the tool frame for the two robots are measured by the sensors and the value of the motors' encoders are outputted as the feedback for the controller. The running simulation in SimMechanics is shown in Figure 3.9.

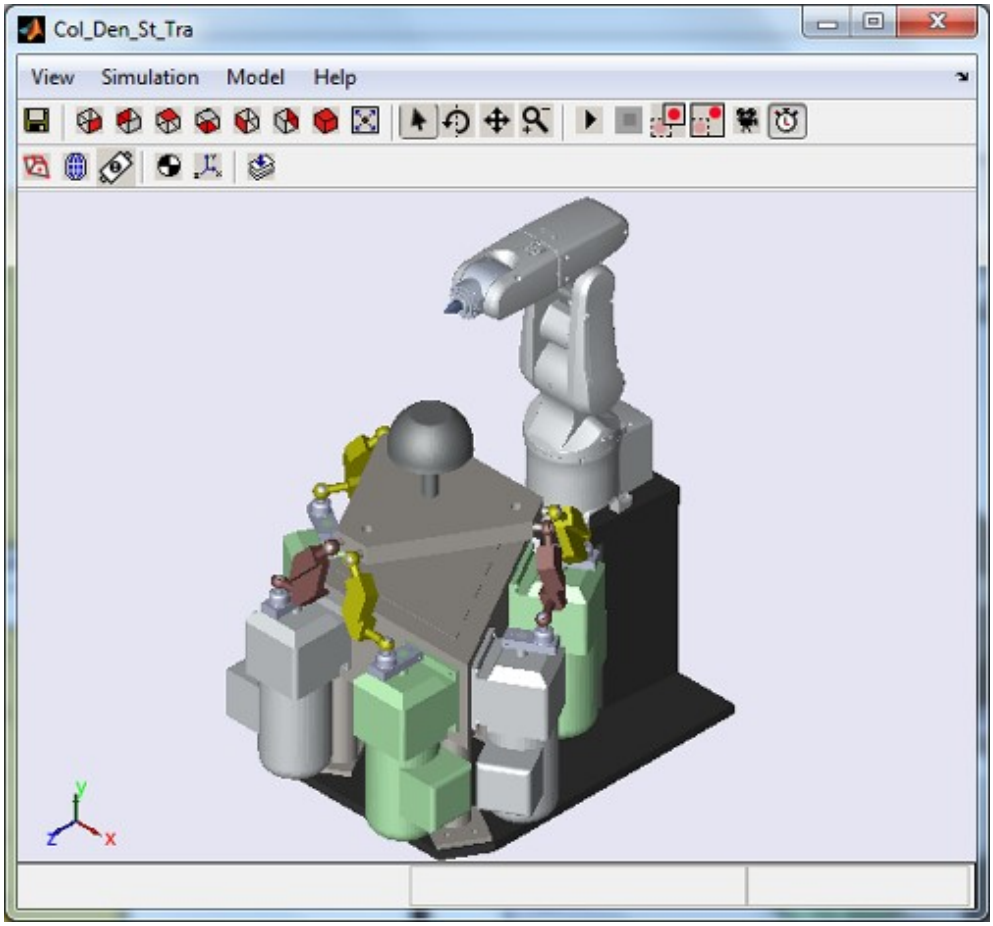

Figure 3.9. Simulation in SimMechanics

3.4.2 Simulation Results in SimMechanics for Bowl Manufacturing

The path planning equations are input into the "trajectory generator" block in SimMechanics to decompose the desired trajectory into control signals for the serial robot, the parallel robot and the rotary stage respectively. The poses of the end effectors of the serial robot and the parallel robot are acquired by the sensors in the SimMechanics mold. In real experiment, the sensor is C-track.

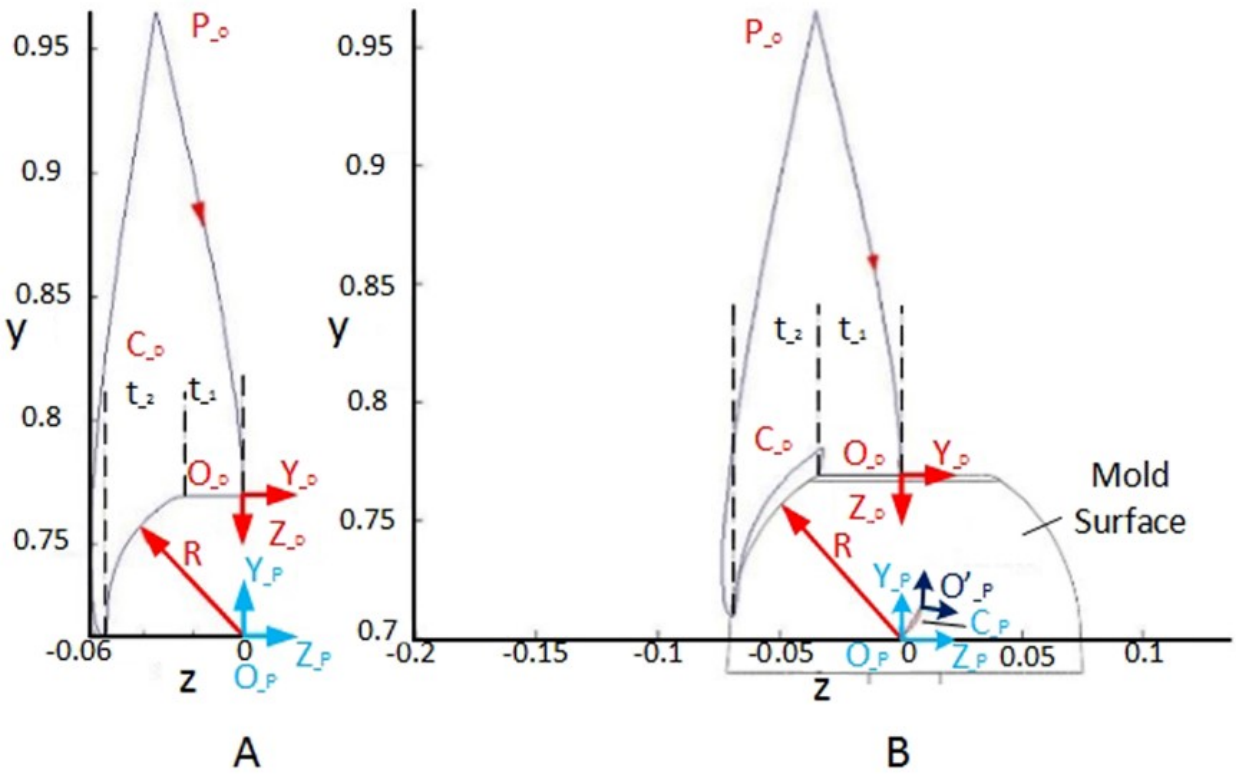

Figure 3.10. The Planning Path for the Bowl Shape Produce

The planned trajectory of the cooperative AFP system when the parallel robot remains still is shown in Figure 3.10 A, where $P_{\_O}$ represents the initial point of the serial robot's tool coordinate frame, $C_{\_D}$ is the planned path of the serial robot, $O_{\_P}$ is the tool frame of the parallel robot, $O_{\_D}$ is the tool frame of the serial robot, the direction $Z_{\_D}$ is always maintained normal to the mold surface, R denotes the radius of the bowl, $t_{\_1}, t_{\_2}$ indicate the two producing processes for planar surface and curved surface. Due to the limitation of the AFP system's workspace, the largest radius of the bowl the cooperative AFP system could manufacture is $R = 62\ mm$ in SimMechanics.

By adding the compensation of the parallel robot, the biggest radius is enlarged to $R = 75\ mm$, as shown in Figure 3.10 B. The tool frame $O'_{\_P}$ of the parallel robot is obtained by rotating the initial frame $O_{\_P}$ about X axis by 4°, and translating it by $13\ mm$ along y direction, $8\ mm$ in z direction. The simulation process of the cooperative AFP system in SimMechanics can be found in the following videos:

SimMechains simulation of the cooperative AFP system:

https://youtu.be/NuZEgudcjaM

https://youtu.be/bS9WXD6SRto

3.4.3 Simulation Result Analysis

The simulation result indicates that the cooperative AFP system could be able to enlarge the workspace to produce larger shape. Additionally, with more degree-of-freedom, the cooperative AFP system could simplify the trajectory planning. In the simulation for producing the curved surface, only a simple two dimension curve is needed for the planning path of the serial robot instead of more complicated space curve for the current AFP. For a more complicated curved surface such as the blade of engine, the planning path could be decomposed into two simpler curves operated by the parallel robot and the serial robot respectively in the cooperative AFP system. Furthermore, the proposed cooperative AFP system could manufacture both the planar surface and the curved surface without changing any equipment in the simulation process, which makes the producing process more flexible and enhances the production efficiency and process adaptivity. With more DOF, the cooperative AFP system can be adopted to more application such as the semi-offline trajectory synchronized algorithm to avoid collision points and singular points.

The position repeatability of Denso Robot is ± 0.02 mm . The accuracy of parallel robot determined from the actuator encoder accuracy is direction x: $\pm 1\ mm$, z: $\pm 1\ mm$, z: $\pm 0.7\ mm$, Roll: $\pm 0.0044\ rad$, pitch: $\pm 0.0046\ rad$, yaw: $\pm 0.0036\ rad$. The accuracy of the cooperative AFP system also depends on the accuracy C-track.

3.5 Summary

This chapter focuses on the kinematic analysis of the cooperative AFP system including the parallel robot and the serial robot. At first, the mechanism of the parallel robot in the lab is introduced. Based on the mechanism, the inverse kinematic of the 6-RSS parallel robot is derived. Then, a numerical forward kinematic method, quasi-Gough forward kinematic algorithm, is presented to determine the uniqueness of forward kinematic solution of the 6-RSS parallel robot. Furthermore, the process of calculating the inverse kinematic of the serial robot based on Denso robot is given. To deal with the multiple solutions, the shortest distance rule is used to choose a

solution closest to the current manipulator. Then, simulation using SimMechanics is conducted for fiber placement of the bowl shape mandrel.

The kinematics analysis, will be used for investigating the singularity and the constraints including the workspace and the joints of the cooperative AFP system, which will be discussed in next chapter.

CHAPTER 4

4 CONSTRAINTS AND SINGULARITIES ANALYSIS

4.1 Introduction

Traditionally, the robotic trajectory planning is strictly subject to kinematic constraints of the robot. Such constraints include the workspace constraint and the joints space constraint. The joints space constraint is defined as the limits of every joint in the robot.

In this chapter, the analysis of the workspace constraint of the 6-RSS parallel robot using geometrical approach with a constant orientation is conducted at first. The geometrical approach is more intuitive, fast and accurate. The constant-orientation workspace can be obtained by the intersection of six so-called vertex spaces. Secondly, the workspace of the serial robot is presented. A proper motion range of the actuator angles of the parallel robot which could cover the biggest available workspace, provide the unique solution for the kinematical calculation and singularity-free is given. And the joints space constraint of the serial robot is introduced. After that, the singularity analysis of the parallel robot is discussed. Finally, the derived processes of the three types of singularities for the wrist-partitioned serial robot is presented. The first two types of singularities can be easily avoided by restricting the workspace of a robot. However, the wrist singularity might happen virtually any place inside the reachable workspace, which requires a algorithm to avoid such singularity.

4.2 Workspace Constraint

4.2.1 Workspace of the Parallel Robot

In this dissertation, a geometrical approach with a constant orientation is used to analyze the workspace of the 6-RSS parallel robot. The three-dimensional workspace is attained by the reachable position of the center point $O'(x, y, z)$ of the upper platform kept at a constant orientation as shown in the structure of the parallel robot in Figure 3.1. The upper frame F_t^p is attached on the upper platform and its origin point locates at the center point of the platform. In order to get the position points of O' with respect to the base frame F_b, the homogenous transformation matrix ${}_p^bT$ from the upper frame F_t^p to the base frame F_b is defined as ${}_p^bT = \begin{bmatrix} & \boldsymbol{R} & & x \\ & & & y \\ & & & z \\ 0 & 0 & 0 & 1 \end{bmatrix}$, so the position of the six vertices of the upper platform $T_i^b(X_{T_i} \quad Y_{T_i} \quad Z_{T_i})$ in terms of the base frame F_b is obtained as

$$\begin{bmatrix} X_{T_i} \\ Y_{T_i} \\ Z_{T_i} \\ 1 \end{bmatrix} = \begin{bmatrix} & \boldsymbol{R} & & x \\ & & & y \\ & & & z \\ 0 & 0 & 0 & 1 \end{bmatrix} \begin{bmatrix} x_{T_i} \\ y_{T_i} \\ z_{T_i} \\ 1 \end{bmatrix} = \begin{bmatrix} M(1,1) + x \\ M(2,1) + y \\ M(3,1) + z \\ 1 \end{bmatrix} \quad (4\text{-}1)$$

where $[x \quad y \quad z]'$ is the position of center point O' in terms of the base frame F_b; $T_i^p(x_{T_i} \quad y_{T_i} \quad z_{T_i})$ denotes the coordinates of vertices of the upper platform with respect to the upper frame F_t^p, as mentioned in Section 3.2; the 3×3 matrix $\boldsymbol{R}$ is the orientation matrix between the upper frame F_t^p to the base frame F_b, which is constant in this case; $[M(1,1) \quad M(2,1) \quad M(3,1)]^T$ is determined by rotation matrix $\boldsymbol{R}$.

So, Eq. (3-5) could be rewritten as

$$(x - x_i)^2 + (y - y_i)^2 + (z - z_i)^2 = L^2 \quad (4\text{-}2)$$

In fact, the solution of Eq. (4-2) is six clusters of sphere, where the radius is L, the spherical center is $O_i(x_i \quad y_i \quad z_i)$, which varies with the change of actuator angles θ_i.

Take the spherical center O_1 for example, from Eq. (3-2) and (4-1),

$$x_1 = X_{B_1} - M(1,1) + r \times \cos\left(\frac{pi}{6} + \theta_1\right) \quad (4\text{-}3)$$

$$y_1 = Y_{B_1} - M(2,1) \quad (4\text{-}4)$$

$$z_1 = Z_{B_1} - M(3,1) - r \times sin\left(\frac{pi}{6} + \theta_1\right) \quad (4\text{-}5)$$

From Eq.(4-3) and (4-5), one has

$$\begin{aligned} r \times \cos\left(\frac{pi}{6} + \theta_1\right) &= x_1 - X_{B_1} + M(1,1) \\ r \times \sin\left(\frac{pi}{6} + \theta_1\right) &= z_1 - Z_{B_1} + M(3,1) \end{aligned} \quad (4\text{-}6)$$

As $\theta_i \in [-\pi, \pi]$, one has

$$(x_1 - x_{O1})^2 + (z_1 - z_{O1})^2 = r^2 \quad (4\text{-}7)$$

where

$$x_{O1} = X_{B_1} - M(1,1) \quad (4\text{-}8)$$

$$z_{O1} = Z_{B_1} - M(3,1) \quad (4\text{-}9)$$

x_{O1}, z_{O1} and y_1 are only dependent upon the orientation matrix of the upper platform $\boldsymbol{R}$, Eq. (4-7) represents a circle with the center point $O_{O1}(x_{O1} \quad z_{O1})$, the radius r on x-z plane and the height y_1 in the 3D Cartesian space. Therefore, for a given orientation $\boldsymbol{R}$, Eq. (4-2) represents six clusters of sphere whose center points $O_i(x_{\mathrm{i}} \quad y_{\mathrm{i}} \quad z_{\mathrm{i}})$ locate on the circles with the center points $O_{Oi}(x_{Oi} \quad z_{Oi})$, the radius r and the height y_1.

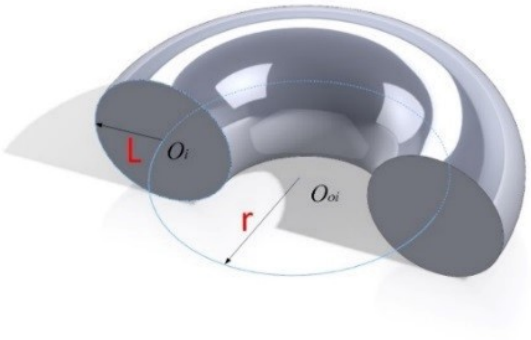

Figure 4.1. The Section View of Cluster of Spheres

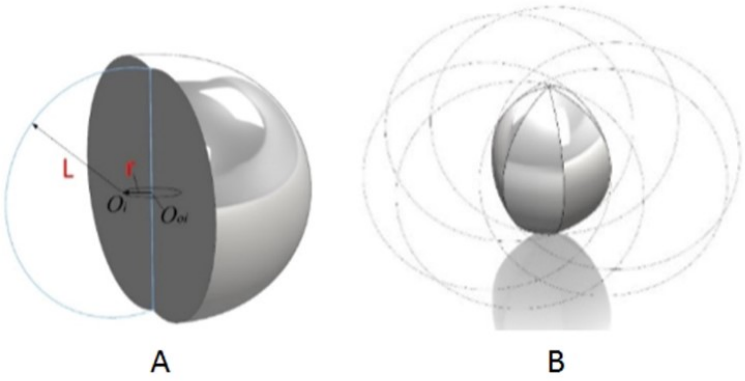

Figure 4.2. Workspace of Parallel Robot with Given Orientation

when $r \geq L$, one cluster of spheres defined by Eq. (4-2) is a torus shown in Figure 4.1. In this case where $r < L$, and $r = 40\ mm$, $L = 160\ mm$, one cluster of spheres could be represented as a vertex space shown in Figure 4.2 A. For a given orientation of the upper platform with Euler angles $[\emptyset \quad \theta \quad \varphi] = [0 \quad 0 \quad 0]$, the workspace of the parallel robot can be obtained as the intersection of the six vertex spaces shown in Figure 4.2 B.

4.2.2 Workspace of the Serial Robot

Traditionally, the planned trajectory is feasible only when it is inside the robot workspace at all time. The workspace of the serial robot is a part of sphere with the radius which is equal to the

length of the arms when they are aligned. The workspace constraints $\boldsymbol{W}_s$ could be formulated in a polar system as follows,

$$\boldsymbol{P}_w = \begin{bmatrix} R_w \cos\theta_w \cos\alpha_w \\ R_w \cos\theta_w \sin\alpha_w \\ R_w \sin\theta_w \end{bmatrix} \quad (4\text{-}10)$$

where, $\boldsymbol{P}_w$ and $[R_w \quad \theta_w \quad \alpha_w]^T$ denotes the coordinates in Cartesian and polar systems. $0 < R_w \leq R_{w_{max}}$, $\theta_{w_{min}} < \theta_w \leq \theta_{w_{max}}$, and $\alpha_{w_{min}} < \alpha_w \leq \alpha_{w_{max}}$, $R_{w_{max}}$ is the maximum possible length of the serial robot, $\theta_{w_{min}}$ and $\theta_{w_{max}}$ are the minimum and maximum angles of the serial robot about its base x axis, $\alpha_{w_{min}}$ and $\alpha_{w_{max}}$ are the minimum and maximum angles of the serial robot about its base z axis.

The serial robot in the lab is Fanuc M-20iA. The workspace of the serial robot is shown in Figure 4.3.

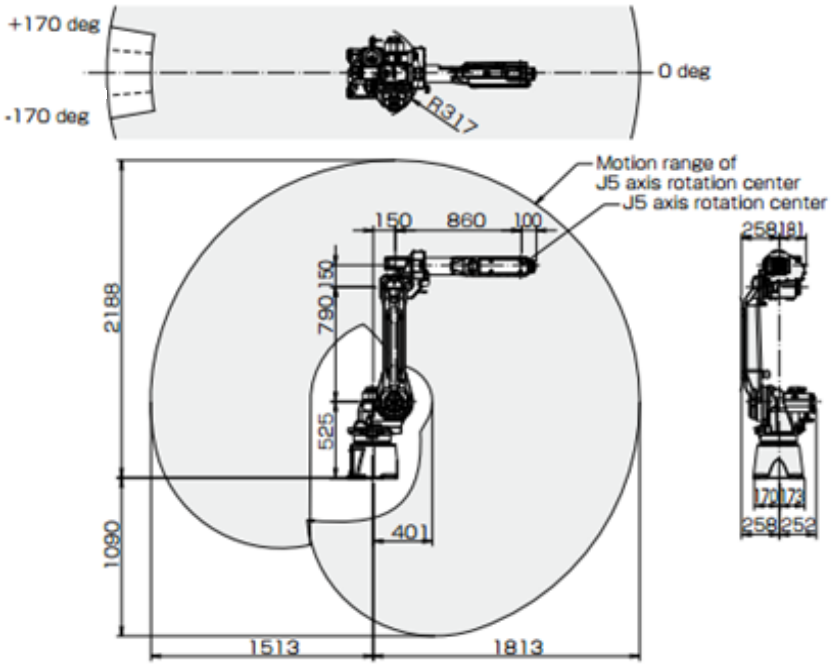

Figure 4.3. Workspace of Fanuc M-20iA

4.3 Joints Space Constraint

4.3.1 Joints Space Constraint of the Parallel Robot

The initial motion range for each rotary actuator is designed as $(-\pi, \pi]$. But limited by the workspace constraint, singularity constraint and the convergence requirement of kinematic solution, the real motion range for the actuators is narrower than the initial one. A proper motion range will be critical for the trajectory planning and collision avoidance work of the 6-RSS parallel robot, and it should satisfy the following requirements.

1. The ability to cover the biggest available workspace: The available workspace of robot is believed to be the union of all its constant-orientation workspaces [46, 49], and the boundary of available or reachable workspace can be used to determine the biggest proper motion range.
2. Singularity-free Requirement: For the safety of the 6-RSS parallel robot, it should be singularity-free in the proper motion range of actuators.
3. The uniqueness for the kinematic solution: In some research, the inverse kinematic mapping of the parallel robot is denoted as,

$$\boldsymbol{\theta} = f(\boldsymbol{p}) \tag{4-11}$$

where $\boldsymbol{p}$ denotes the pose of the end-effector of the parallel robot, $\boldsymbol{\theta}$ is the actuator angles. If f^{-1} exist, there may have 40 forward kinematic solutions for a determined $\boldsymbol{\theta}$ [139]. To avoid the numerical calculation processes of either inverse or forward kinematic to converge to the wrong solution, special motion domain and constraint conditions should be determined.

In the previous work, [135] presents the final motion range in which the 6- RSS parallel robot do not need to consider the singularity and bifurcation is $(-0.9948\text{rad}, 0.9948\text{rad})$.

4.3.2 Joints Space Constraint of the Serial Robot

Normally, it is necessary to make sure the serial robot respects its joint limits. The joints space constraints $\boldsymbol{J}_s$ can be given by,

$$\boldsymbol{q}_{min} \leq \boldsymbol{q} \leq \boldsymbol{q}_{max} \quad (4\text{-}12)$$

where $\boldsymbol{q}$ is the joint vector of the serial robot, $\boldsymbol{q}_{min}$ and $\boldsymbol{q}_{max}$ are defined as the joint limits of the serial robot. The joints limits of the serial robot Fanuc M20-iA are shown in Table 4-1.

Table 4-1. The Joints Limits

Joints	Minimum	Maximum
1	$-170°$	$170°$
2	$-100°$	$125°$
3	$-60°$	$250°$
4	$-200°$	$200°$
5	$-120°$	$120°$
6	$-270°$	$270°$

Using the inverse kinematic function, which can transform coordinates of the end-effector to joints, the workspace constraint $\boldsymbol{W}_s$ can be written as following,

$$\boldsymbol{q}_{min} \leq \boldsymbol{I}_{\boldsymbol{p}_{\boldsymbol{w}_s}} \leq \boldsymbol{q}_{max} \quad (4\text{-}13)$$

where $\boldsymbol{I}_{\boldsymbol{p}_{\boldsymbol{w}_s}}$ denotes the inverse kinematic function of the poses in $\boldsymbol{W}_s$ [140].

4.4 Singularities

4.4.1 Singularities Analysis of the Parallel Robot

Singularities analysis of the 6-RSS parallel robot is presented as follows.

Differentiating Eq.(3-5) with respect to time

$$L\boldsymbol{n}_i^T\left(\dot{\boldsymbol{c}} + \dot{\boldsymbol{R}}\boldsymbol{t}_i - r[-\sin\theta_i \quad 0 \quad \cos\theta_i]^T\dot{\theta}_i\right) = 0 \tag{4-14}$$

and substituting Eq.(3-4) to Eq.(4-14), one can obtain

$$L\boldsymbol{n}_i = \begin{bmatrix} X_{T_i} - X_{A_i} - r\cos\theta_i \\ Y_{T_i} - Y_{A_i} \\ Z_{T_i} - Z_{A_i} - r\sin\theta_i \end{bmatrix} = 0 \tag{4-15}$$

$$L[\boldsymbol{n}_i^T \quad (\boldsymbol{t}_{bi} \times \boldsymbol{n}_i)^T]\begin{bmatrix}\dot{\boldsymbol{c}} \\ \boldsymbol{\omega}\end{bmatrix} = r(z_i\cos\theta_i - x_i\sin\theta_i)\dot{\theta}_i \tag{4-16}$$

The above equation can be simplified and written in matrix form using Eq.(3-8) and Eq.(3-9)

$$L\begin{bmatrix}\boldsymbol{n}_1^T & (\boldsymbol{t}_{b1}\times\boldsymbol{n}_1)^T \\ \vdots & \vdots \\ \boldsymbol{n}_6^T & (\boldsymbol{t}_{b6}\times\boldsymbol{n}_6)^T\end{bmatrix}\boldsymbol{v} = r\begin{bmatrix}\mp\sqrt{x_1^2 + z_1^2 - p_1^2} & & 0 \\ & \ddots & \\ 0 & & \mp\sqrt{x_6^2 + z_6^2 - p_6^2}\end{bmatrix}\dot{\boldsymbol{\theta}} \tag{4-17}$$

where $\boldsymbol{\omega}$ denotes the angular velocity of the upper platform; $\boldsymbol{v} = [\dot{\boldsymbol{c}}^T \quad \boldsymbol{\omega}^T]^T$; $\dot{\boldsymbol{\theta}} = \begin{bmatrix}\dot{\theta}_1 & \dot{\theta}_2 & \dots & \dot{\theta}_6\end{bmatrix}^T$ denotes the vector of actuator joint rates; $\boldsymbol{t}_{bi}$ is $\boldsymbol{t}_i$ expressed in base frame F_b. Eq.(4-17) can be written as

$$\boldsymbol{A}\boldsymbol{v} = \boldsymbol{B}\dot{\boldsymbol{\theta}} \tag{4-18}$$

where two matrices $\boldsymbol{A}$ and $\boldsymbol{B}$ are referred to as Jacobian matrices. The first, second and third kinds of singularities occur when matrix $\boldsymbol{B}$ is singular, matric $\boldsymbol{A}$ is singular and matrices $\boldsymbol{A}$ and $\boldsymbol{B}$ are simultaneously singular respectively, which is clarified by Gosselin and Angeles first [141].

For the first kind of singularity, the determinant of matrix $\det(\boldsymbol{B}) = 0$ which means one (or some) of T_iB_i is perpendicular to the instantaneous velocity of B_i, or T_iB_i happens to projecting onto the A_iB_i in xoz plane, as shown in Figure 4.4 (a-b). With a geometric analysis, a sufficient condition for $\det(\boldsymbol{B}) = 0$ is "the ball with a center T_i tangents to the circle with a center A_i in the single point B_i ", shown in Figure 4.4 (c).

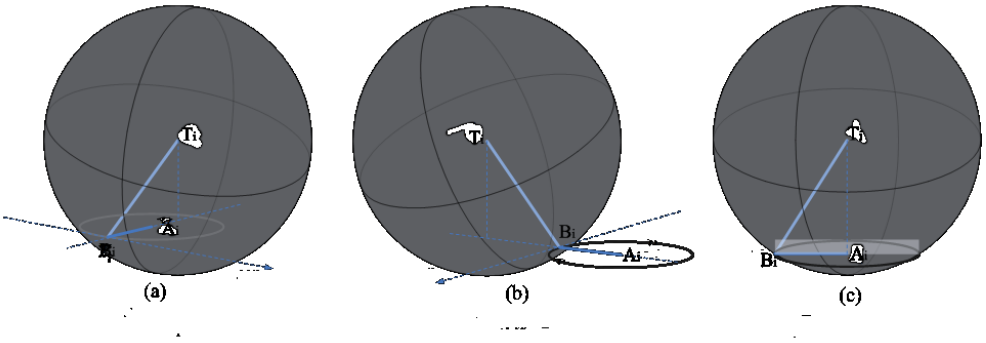

Figure 4.4. Geometric Relationship of Singularities

Based on line geometry [142], the robot singularity occurs when the orientation vector of the forces and torques acted on the end-effector are coupling to each other. In other word, real singularity for 6-RSS parallel robot occurs when $\det(\boldsymbol{A}) = 0$. To avoid the perturbation from degenerate singularity surface, the Cauchy Index of $\boldsymbol{A}$ can be used to determine the singularity based on the conclusion of [143]. Then for any two very closing points $p_1, p_2 \in M$, the singularity constraint condition is given as follows:

$\left|\Delta_{p_1}^{A} - \Delta_{p_2}^{A}\right| = 0$ line p_1p_2 still in a simple connected domain;

$\left|\Delta_{p_1}^{A} - \Delta_{p_2}^{A}\right| = 2$, line p_1p_2 cross a non-degenerate singularity surface;

$\left|\Delta_{p_1}^{A} - \Delta_{p_2}^{A}\right| > 2$,and in line p_1p_2, min $\det(\boldsymbol{A}) = 0$, line p_1p_2 cross a degenerate singularity surface.

where $\Delta_{p_1}^{A}$ is Cauchy index of matrix $\boldsymbol{A}$ in the point p_1; M is actuator parameter space (joint space) [135].

4.4.2 Singularities Analysis of the Serial Robot

The serial robot used in the cooperative AFP system is Fanuc M20-iA, which is a wrist-partitioned manipulator and whose wrist axes (the last three axes) intersect in a common point C. The structure of the serial robot is shown in Figure 4.5. The positioning and orienting problems can be considered separately due to the structure of this kind of serial robot, which is called partitioned or decoupled. The serial robots with such structure exhibit three types of singularities, which are elbow singularity, shoulder singularity and wrist singularity [144].

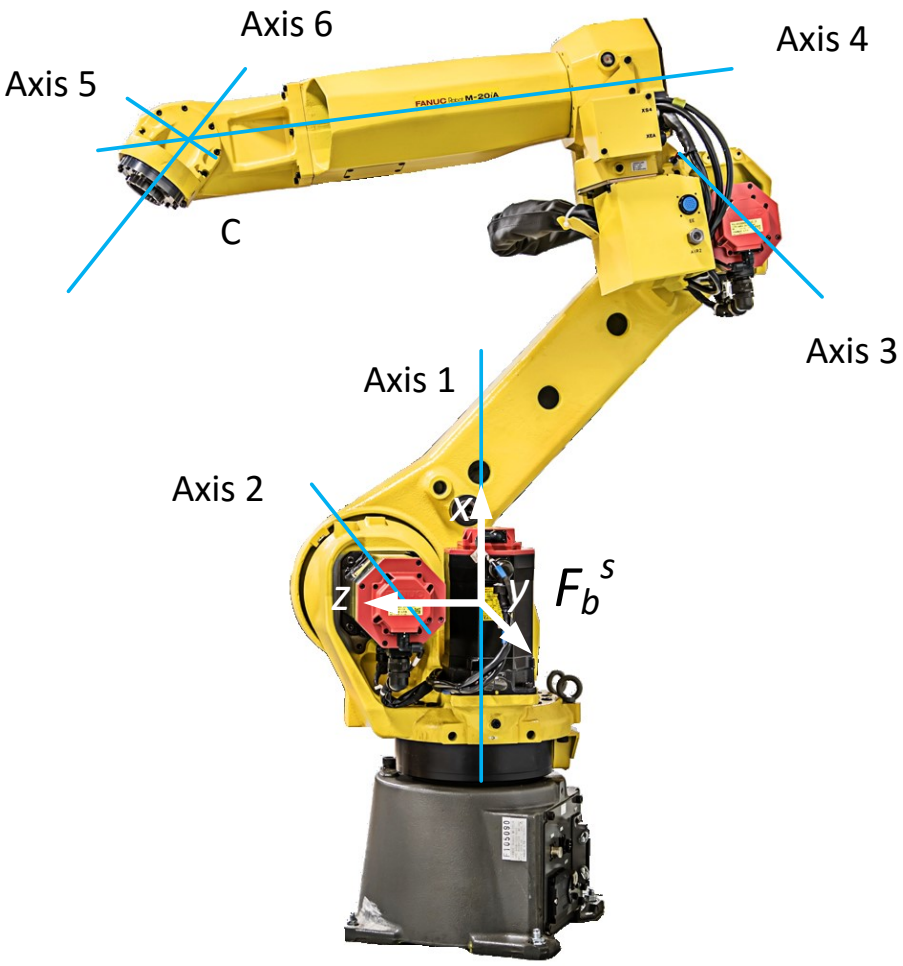

Figure 4.5. Structure of Fanuc M-20iA

Like the parallel robot mentioned in Section 4.4.1, the Jacobian is a time-varying linear transformation that relates the Cartesian velocities of the end-effector to the time rate of change of the joint angles, which can be expressed as,

$$\boldsymbol{v} = \boldsymbol{J}\dot{\boldsymbol{\theta}} \tag{4-19}$$

where $\dot{\boldsymbol{\theta}} = \begin{bmatrix}\dot{\theta}_1 & \dot{\theta}_2 & \dots & \dot{\theta}_6\end{bmatrix}^T$ denotes the six actuator joint rates.

The determinant of the Jacobian of a six-axis robot keeps the same by changing the end-effector reference point to the intersection point of the wrist axes C [145, 146].

The velocity vector of the end-effector is,

$$\boldsymbol{v} = \begin{bmatrix} \boldsymbol{\omega} \\ \dot{\boldsymbol{c}} \end{bmatrix} \quad (4\text{-}20)$$

where $\boldsymbol{\omega} = \begin{bmatrix} \omega_x \\ \omega_y \\ \omega_z \end{bmatrix}$ denotes the angular velocity vector of the end-effector reference frame, $\dot{\boldsymbol{c}} = \begin{bmatrix} \dot{c}_x \\ \dot{c}_y \\ \dot{c}_z \end{bmatrix}$ denotes the linear velocity vector of the intersection point of the wrist axes C with respect to the base frame of the serial robot F_b^S.

The linear velocity vector $\dot{\boldsymbol{c}}$ contributed by each angular joint velocity must be perpendicular to the planes spanned by corresponding pairs of vectors of angular joint velocities and $\boldsymbol{r}_i$ which is the position vectors of the intersection point C with respect to the origin of the coordinate frame attached on the i^{th} joint axis. It can be write as

$$\dot{\boldsymbol{c}} = \dot{\theta}_1 e_1 \times r_1 + \dot{\theta}_2 e_2 \times r_2 + \dot{\theta}_3 e_3 \times r_3 \quad (4\text{-}21)$$

where $\boldsymbol{e}_i$ denotes the direction vectors of the i^{th} joint axes with respect to the base frame of the serial robot F_b^S.

The angular velocity vector $\boldsymbol{\omega}$ of the frame attached on the end-effector with the origin on the intersection point of the wrist axes C can be expressed as the vector sum of the contributions of the angular velocities of the individual joints, shown as follows,

$$\boldsymbol{\omega} = \dot{\theta}_1 e_1 + \dot{\theta}_2 e_2 + \cdots + \dot{\theta}_6 e_6 \quad (4\text{-}22)$$

Based on Eq.(4-21) and Eq.(4-22), the Jacobian matrix can be given by,

$$\boldsymbol{J} = \begin{bmatrix} \boldsymbol{J}_{11} & \boldsymbol{J}_{12} \\ \boldsymbol{J}_{21} & \boldsymbol{J}_{22} \end{bmatrix} = \begin{bmatrix} e_1 & e_2 & e_3 & e_4 & e_5 & e_6 \\ e_1 \times r_1 & e_2 \times r_2 & e_3 \times r_3 & \multicolumn{3}{c}{\mathbf{0}_{3\times 3}} \end{bmatrix} \quad (4\text{-}23)$$

The six columns of $\boldsymbol{J}$ are the Plücker line ray-coordinates of the six axes, which means the first three elements in each column are the direction cosines of the corresponding axis and the last three are the components of the moment of the axis with respect to the intersection point C [61]. The moment components of the last three axes of the serial robot with respect to the point C are zero as those axes pass through the intersection point C, so one has $\boldsymbol{J}_{22} = \mathbf{0}_{3\times 3}$.

As shown in Figure 4.5, the first axis of the serial robot always points along the z-axis of the base frame F_b^s. Additionally, axis 2 and axis 3 are parallel to each other and the xy-plane of the base frame F_b^s, which means both perpendicular to the first axis. Thus, $e_2 = e_3$, and the Jacobian matrix can be rewritten as,

$$\boldsymbol{J} = \begin{bmatrix} 0 & e_{3_x} & e_{3_x} & e_{4_x} & e_{5_x} & e_{6_x} \\ 0 & e_{3_y} & e_{3_y} & e_{4_y} & e_{5_y} & e_{6_y} \\ e_{1_z} & 0 & 0 & e_{4_z} & e_{5_z} & e_{6_z} \\ -e_{1_z}r_{1_y} & e_{3_y}r_{2_z} & e_{3_y}r_{3_z} & 0 & 0 & 0 \\ -e_{1_z}r_{1_x} & -e_{3_x}r_{2_z} & -e_{3_x}r_{3_z} & 0 & 0 & 0 \\ 0 & e_{3_x}r_{2_y} - e_{3_y}r_{2_x} & e_{3_x}r_{3_y} - e_{3_y}r_{3_x} & 0 & 0 & 0 \end{bmatrix} \quad (4\text{-}24)$$

Thus, the determinant of the Jacobian matrix $\boldsymbol{J}$ ban be given by,

$$\begin{aligned} det(\boldsymbol{J}) = e_{1_z}\Big(& r_{2_z}e_{3_y}r_{3_x} - e_{3_x}r_{2_z}r_{3_y} + e_{3_x}r_{3_z}r_{2_y} \\ & - r_{3_z}e_{3_y}r_{2_x}\Big)\Big(r_{1_y}e_{3_x} - e_{3_y}r_{1_x}\Big)\Big(e_{4_x}e_{5_z}e_{6_y} \\ & - e_{4_x}e_{6_z}e_{5_y} + e_{4_y}e_{5_x}e_{6_z} - e_{4_y}e_{6_x}e_{5_z} + e_{4_z}e_{6_x}e_{5_y} \\ & - e_{4_z}e_{5_x}e_{6_y}\Big) \end{aligned} \quad (4\text{-}25)$$

The first factor of the determinant of the Jacobian matrix $det(\boldsymbol{J})$, e_{1_z}, denotes the direction of the first joint axis which $e_{1_z} = 1$.

A. The elbow singularity occurs when the second factor in Eq.(4-26) is equal to 0, which means,

$$r_{2_z}e_{3_y}r_{3_x} - e_{3_x}r_{2_z}r_{3_y} + e_{3_x}r_{3_z}r_{2_y} - r_{3_z}e_{3_y}r_{2_x} = 0 \quad (4\text{-}26)$$

Because Eq.(4-26) will not be affected by the parameter of the first actuator joint θ_1, it is assumed that $\theta_1 = 0°$, which means axis 2 and axis 3 are parallel to the xy-plane of the base frame F_b^s. Thus, $e_{3_x} = 0$, and $e_{3_y}$is the only component of the direction vector. As the result, Eq.(4-26) can be rewritten as,

$$r_{2_z}r_{3_x} = r_{3_z}r_{2_x} \quad (4\text{-}27)$$

which can be satisfied whenever $\boldsymbol{r}_2$ and $\boldsymbol{r}_3$ are aligned. Based on the initial actuator angles of Fanuc M20-iA, Eq.(4-27) can be satisfied by,

$$\theta_3 = \pm\frac{\pi}{2} \qquad (4\text{-}28)$$

However, $\theta_3 = -\frac{\pi}{2}$ is precluded by joint limits and interference. Therefore, this type of positional singularity is restricted to the condition when $\theta_3 = \frac{\pi}{2}$.

The elbow singularity occurs whenever the wrist center lies in the same plane as the axes of joint 2 and joint 3. The elbow singular sub-space consists of a portion of a torus' surface centered at the origin of the base frame F_b^s. The torus shape parameters are dependent upon the link lengths and joint offset between axes of the joint 1 and joint 2. Two elbow singular configurations are shown in Figure 4.6.

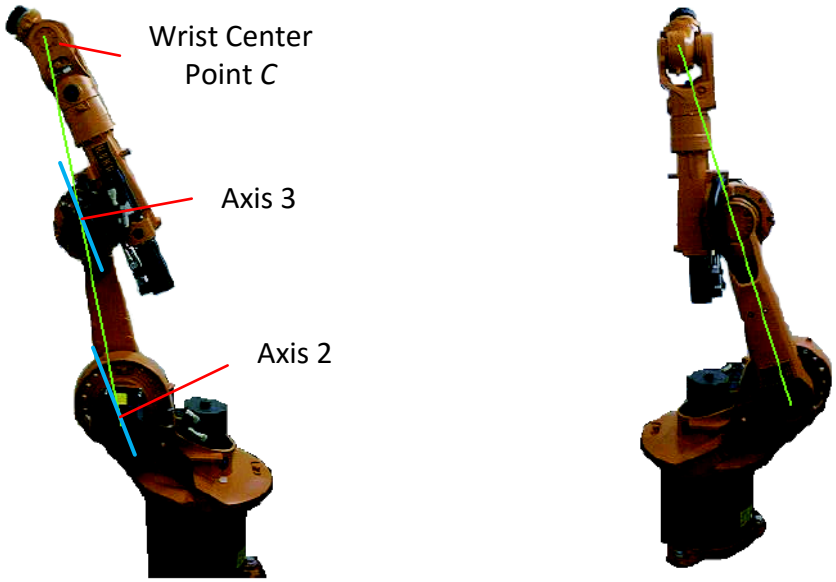

Figure 4.6. Elbow Singularity [144]

B. The shoulder singularity occurs when the third factor in Eq.(4-26) vanishes, which is given by,

$$r_{1_y} e_{3_x} - e_{3_y} r_{1_x} = 0 \qquad (4\text{-}29)$$

Accordingly, when $e_{3_x} = 0$, then $r_{1_x} = 0$ due to the fact that the components of $\boldsymbol{e}_3$, a direction vector which is parallel to the xy-plane, e_{3_x}, e_{3_y}, e_{3_z} cannot equal to zero simultaneously. Because of the construction of the Fanuc M20-iA, as well as the condition $e_{3_x} = e_{3_z} = 0$, the wrist center point C lies on the z-axis of the base frame F_b^s.

When $e_{3_y} = 0$, then $r_{1_y} = 0$. The reason is the same as the first circumstance, which is that e_{3_x}, e_{3_y}, e_{3_z} cannot equal to zero simultaneously. Due to the structure of the Fanuc M20-iA, as well as the condition $e_{3_y} = e_{3_z} = 0$, the wrist center point C lies on the z-axis of the base frame F_b^s.

To sum up, the shoulder singularity occurs when the wrist center point C lies on a cylinder centered about axis of joint 1 and with a radius r equal to the distance between axes of joint 1 and joint 4. In this case, $r = 0$. Two shoulder singular configurations are shown in Figure 4.7.

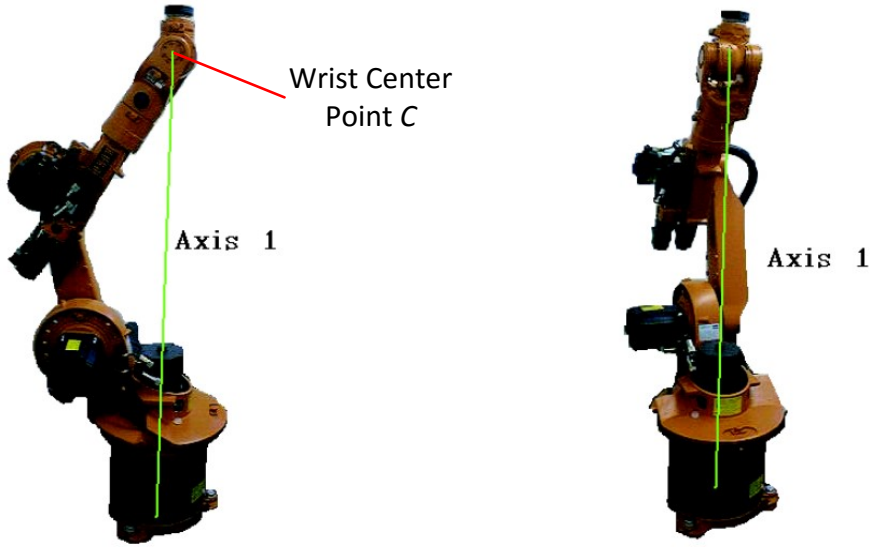

Figure 4.7. Shoulder Singularity [144]

C. The wrist singularity occurs when the fourth factor in Eq. (4-26) equals to zero, which is given by,

$$e_{4_x}e_{5_z}e_{6_y} - e_{4_x}e_{6_z}e_{5_y} + e_{4_y}e_{5_x}e_{6_z} - e_{4_y}e_{6_x}e_{5_z} + e_{4_z}e_{6_x}e_{5_y} - e_{4_z}e_{5_x}e_{6_y} = 0 \quad (4\text{-}30)$$

Differing from the former two singularities which depend on the position of the wrist center point C, the wrist singularity is orienting singularity. Assuming the orientation of one of the last three axes is fixed, Eq.(4-30) can reduced as,

$$e_{4_y}e_{6_z} - e_{4_z}e_{6_y} = 0 \qquad (4\text{-}31)$$

when $\boldsymbol{e}_5 = \begin{bmatrix}1\\0\\0\end{bmatrix}$.

$$e_{4_z}e_{6_x} - e_{4_x}e_{6_z} = 0 \qquad (4\text{-}32)$$

when $\boldsymbol{e}_5 = \begin{bmatrix}0\\1\\0\end{bmatrix}$.

$$e_{4_x}e_{6_y} - e_{4_y}e_{6_x} = 0 \qquad (4\text{-}33)$$

when $\boldsymbol{e}_5 = \begin{bmatrix}0\\0\\1\end{bmatrix}$.

Thus, the wrist singularity occurs whenever the axes of joint 4 and joint 6 are aligned. Similarly, assuming the fixed $\boldsymbol{e}_4$ or $\boldsymbol{e}_6$, the singular conditions satisfied when $\boldsymbol{e}_5$ is parallel to $\boldsymbol{e}_6$ or $\boldsymbol{e}_4$ is parallel to $\boldsymbol{e}_5$. However, due to the structure of the wrist-partitioned robot Fanuc M20-iA, $\boldsymbol{e}_5$ is always perpendicular to $\boldsymbol{e}_4$ and $\boldsymbol{e}_6$, such conditions can never be satisfied.

Summarily, based on the initial actuator angles of the Fanuc M20-iA, the wrist singularity occurs whenever the fifth actuator angle $\theta_5 = 0°$ as shown is Figure 4.8.

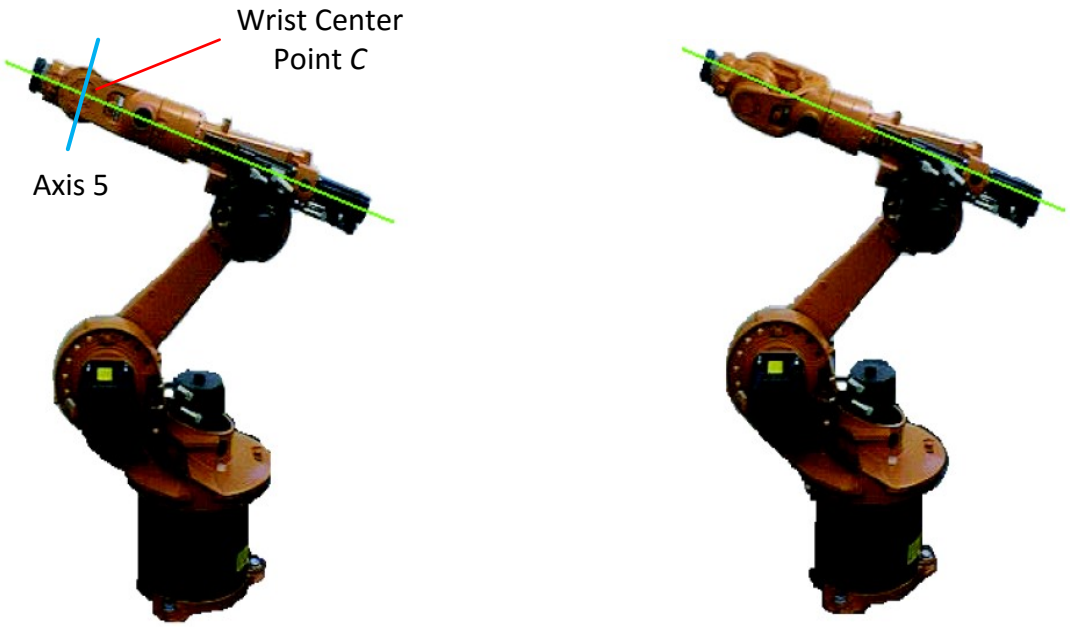

Figure 4.8. Wrist Singularity [144]

The first two types of singularities can be easily avoided by restricting the workspace of a robot. The locations of these two types of singularities in the workspace of the Fanuc M20-iA are shown in Figure 4.9.

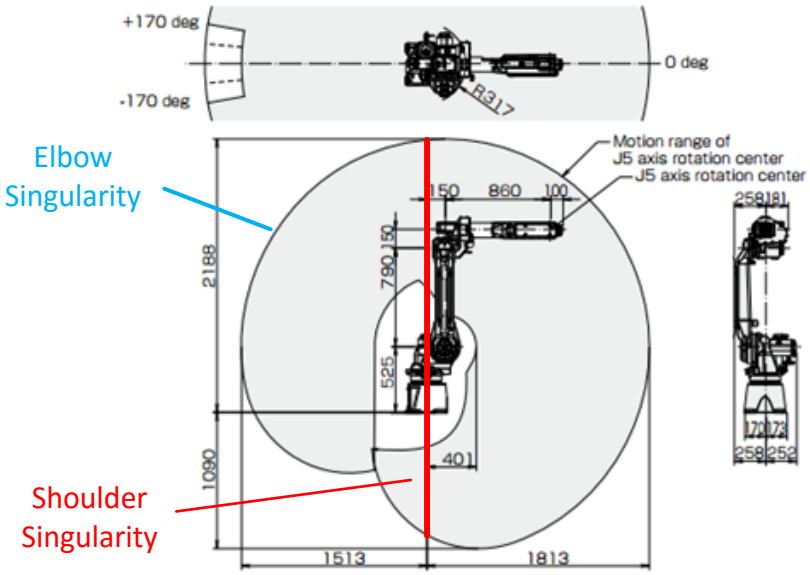

Figure 4.9. Locations of the first two types of Singularities

However, the wrist singularity might happen virtually any place inside the reachable workspace.

4.5 Summary

This chapter focuses on the analysis of the constraints and singularities of the cooperative AFP system. The comprehensive analysis of the workspace constraint of the 6-RSS parallel robot using geometrical approach with a constant orientation is conducted. The geometrical approach is more intuitive, fast and accurate. The constant-orientation workspace can be obtained by the intersection of six so-called vertex spaces. And then, the workspace of the serial robot is presented. A proper motion range of the actuator angles of the parallel robot which could cover the biggest available workspace, provide the unique solution for the kinematical calculation and singularity-free is given. And the joints space constraint of the serial robot is introduced. After that, the singularity analysis of the parallel robot is discussed. Finally, the derived processes of the three types of singularities for the wrist-partitioned serial robot is presented. The first two types of singularities can be easily avoided by restricting the workspace of a robot. However, the wrist singularity might happen virtually any place inside the reachable workspace. A control algorithm is needed to avoid such singularity, which will be covered in Chapter 6.

.

CHAPTER 5

5 POSE TRACKING AND KINEMATIC PARAMETERS CALIBRATION

5.1 Introduction

When the robot is close to its constraints or singularities found on the trajectory, it is not possible to go back and choose another path after the trajectory of the robot is defined. During the fiber laying up process, it is important to keep the continuous operation to avoid the robots' constraints and singularities. However, the pre-planned paths for both robots in the collaborative AFP system may often comprise of the constraints or singularities of the robots. In order to keep the continuous operation, a visual servoing control strategy is designed to move the robots away from the constraints or singularities points without changing the pre-planned fiber path. The visual servoing control strategy uses the photogrammetry sensor to obtain the pose information of both robots and generates the pose correction which can be added to the off-line planned path in the real time. To realize such visual servoing control strategy, so called semi-offline trajectory synchronized algorithm, the accurate poses of both robots need to be measured for precise pose tracking.

The accurate poses of both robots in the cooperative AFP system are obtained by a photogrammetry sensor and are used as the pose feedback for precise pose tracking in the three-dimensional workspace. An eye-to-hand position based visual servoing scheme is adopted. The photogrammetry sensor, C-track, is used in this project.

In this chapter, the pose estimation of an object is introduced at first. The processes of the frame definitions for both the parallel robot and the serial robot are presented. Moreover, in order to refine the kinematic model and the CAD model of the 6-RSS parallel robot, some kinematic

parameters used in parallel robot modelling are calibrated using C-track. The VXelements software provided by Creamform is used for the visual tracking modelling.

5.2 Pose Estimation of an Object

The purpose of using photogrammetry sensor is to detect the poses of the end-effectors on parallel robot and serial robot, and to on-line adjust the pre-planned trajectory for avoiding singularities, optimizing joint limits based and expanding workspace of the cooperative AFP system on the estimated poses.

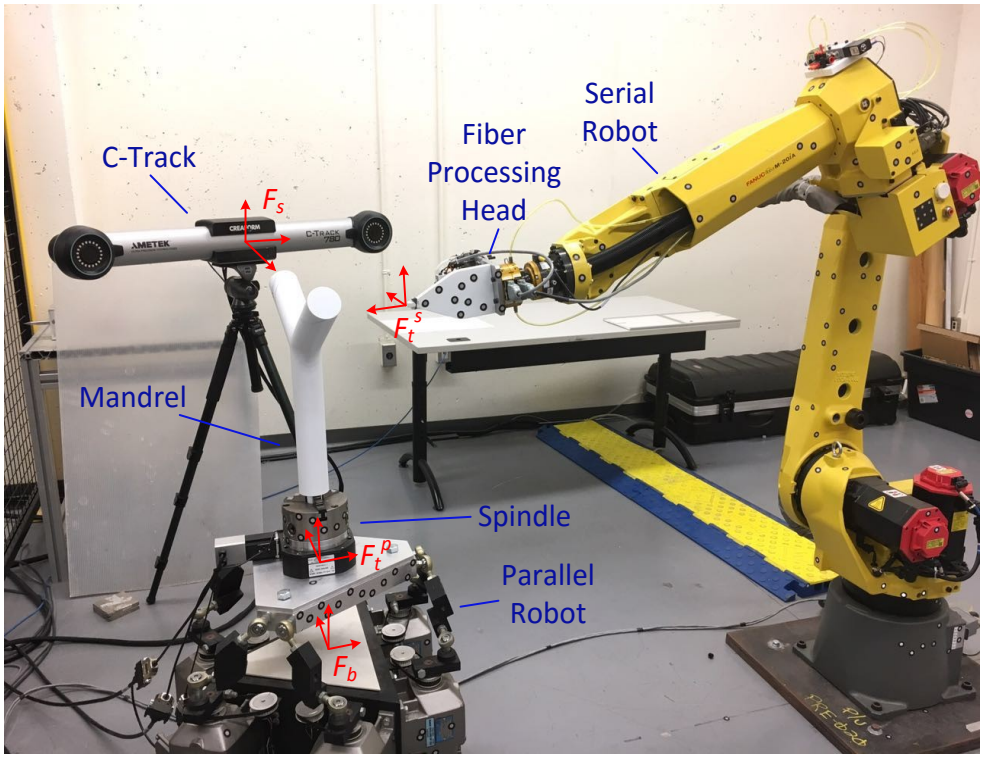

Figure 5.1. Cooperative AFP System Setup

The default sensor frame is denoted as F_s whose origin is at the center of photogrammetry sensor as shown in Figure 5.1. The pose of the object with respect to F_s is composed of three position variables and three orientation variables which define the pose of the object frame F_O with respect to F_s. The pose estimation is to localize F_O with respect to F_s, which is developed by mapping object targets from F_O onto F_s and then projecting them onto the image plane [123].

The photogrammetry sensor used in the cooperative AFP system is C-track 780 which is a dual-camera sensor. It can track the object with a rigid set of reflectors as the targets in real time. Assume that there is no relative movement among all the targets on the same rigid object. Consider n targets on the rigid model. The homogenous coordinates of each target with respect to F_s are represented as ${}_i^S P = (x_i, y_i, z_i, 1)$, $i = 1 \cdots n$. The projection coordinates of each target on the image plane of the j^{th} camera is denoted as ${}_{ij}^C P = \left(u_{ij}, v_{ij}, 1\right)$, $i = 1 \cdots n$ and j is the number of cameras, in this case, $j = 1, 2$. The perspective projection is shown as following,

$$\begin{aligned} {}_{ij}^C P &= {}_j^C M \, {}_i^S P \\ {}_j^C M &= B_j \, {}_S^C T_i \end{aligned} \tag{5-1}$$

where ${}_j^C M$ is the projection matrix of each camera; B_j is the camera matrix, containing the intrinsic parameters of the j^{th} camera; ${}_S^C T_i$ is the homogenous transformation matrix from the sensor frame F_s to the j^{th} camera frame, B_j and ${}_S^C T_i$ are known after the calibration of the dual-cameras sensor. ${}_i^S P$ can be calculated when ${}_{ij}^C P$ is obtained in the image plane [147].

The homogenous coordinates of the n targets on the object with respect to the object frame F_O are denoted as $\boldsymbol{p}_i^o = (x_i^o, y_i^o, z_i^o, 1)$, which is known when the object frame F_O is defined. The current pose $\boldsymbol{p}_c(t)$ of F_O with respect to F_s is denoted as $(x_c, y_c, z_c, \alpha_c, \beta_c, \gamma_c)$, where (x_c, y_c, z_c) are the three origin position variables of F_O and $(\alpha_c, \beta_c, \gamma_c)$ are the three orientation variables of F_O. The homogenous transformation matrix ${}_o^s \boldsymbol{T}$ from F_O to F_s can be shown as the following,

$${}_o^s \boldsymbol{T} = \begin{bmatrix} R(\alpha_c, \beta_c, \gamma_c) & (x_c, y_c, z_c)^T \\ 0 \quad 0 \quad 0 & 1 \end{bmatrix} \tag{5-2}$$

where $R(\alpha_c, \beta_c, \gamma_c)$ is the rotation matrix from F_O to F_s. Thus, the transformation equation of i^{th} target can be written like this,

$$\begin{aligned} {}_i^S P &= {}_o^s \boldsymbol{T} \boldsymbol{p}_i^o \\ &= \begin{bmatrix} c\alpha_c c\beta_c & c\alpha_c s\beta_c s\gamma_c - s\alpha_c c\gamma_c & c\alpha_c s\beta_c c\gamma_c + s\alpha_c s\gamma_c & x_c \\ s\alpha_c c\beta_c & s\alpha_c s\beta_c s\gamma_c + c\alpha_c c\gamma_c & s\alpha_c s\beta_c c\gamma_c - c\alpha_c s\gamma_c & y_c \\ -s\beta_c & c\beta_c s\gamma_c & c\beta_c c\gamma_c & z_c \\ 0 & 0 & 0 & 1 \end{bmatrix} \begin{bmatrix} x_i^o \\ y_i^o \\ z_i^o \\ 1 \end{bmatrix} \end{aligned} \tag{5-3}$$

where $c\alpha = \cos(\alpha)$ and $s\alpha = \sin(\alpha)$. At least six independent equations are required to obtain the pose $(x_c, y_c, z_c, \alpha_c, \beta_c, \gamma_c)$, which means the image plane measurements of a minimum of three non-collinear targets are needed. But at least four coplanar targets are needed for a unique solution. Additional non-coplanar targets can improve the estimation accuracy in the presence of measurement noise [148].

5.3 Frame Definitions

5.3.1 Frame Definitions of the Parallel Robot

VXelements provided by Creamform was used for the visual tracking modelling. As mentioned in Section 5.2, at least four positioning targets can determine the pose of a unique object. There are four referencing modes can be adopted in VXelements for pose tracking using C-track, which are static, dynamic, sensor and automatic. Each mode has its own features presented as following.

- Sensor mode: In this mode, C-track and part cannot move during the work.
- Dynamic mode: When the environment of work has vibrations, it is suggested to use dynamic mode. In this mode the positioning targets need to remain in the place where they are detected at first time. Each time, a minimum of four positioning targets should be observed by C-track as well. The most important feature is that C-track can be moved during the experimental work.
- Static mode: In contrast to dynamic mode, when using the static mode, it's not allowed to move the C-track and the part during the measurement. But the advantage of this mode is C-track does not need to see the targets for each time of measuring.
- Automatic mode: It is a combination of static and dynamic modes. In this kind of mode, a minimum of one positioning target must to be seen by C-track during the measurement all the time. If the visible positioning targets are less than four, the system switches to static mode automatically. Furthermore, the targets could not be obstructed more than five minutes.

In this experimental work, the dynamic referential mode is used because the vibration of the environment and the location of C-track need to be moved to detect the poses of the objects with different angles during the measurement.

The referential object is defined by the positioning targets attached on the motors and the tracking object is defined by the positioning targets stuck on the upper platform. The positioning targets need to remain in the place where they was detected at the first time and a minimum of four positioning targets should be observed by C-track all the time.

Since the number of the positioning targets on the motors and the upper platform is more than 3, the poses $(x_t, y_t, z_t, \alpha_t, \beta_t, \gamma_t)$ of the referential object and the tracking object can be determined uniquely, as shown in Figure 5.2. Accordingly, the base frame F_b on the referential object and the tool frame F_t^P on the upper platform should be defined.

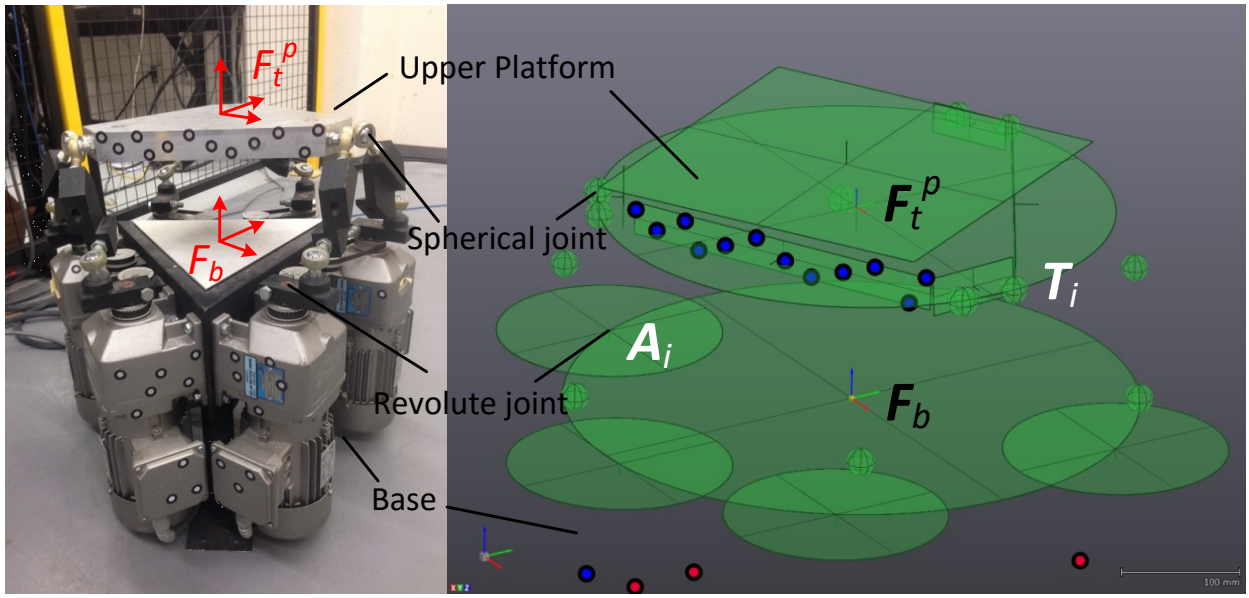

Figure 5.2. Frame Definitions of the Parallel Robot

Compared to the serial robot, defining coordinate frame is more difficult for the parallel robot due to the RSS structure. The center points of revolute joints A_i and the center points of spherical joints T_i cannot be observed accurately enough by C-Track directly.

The process of defining the base frame F_b is shown as follows:

1) Creating circles to define the center points of revolute joints A'_i.

A magnetic target is attached on the movement link of the revolute joint. The magnetic target is detected and recorded every time of moving the motor for a certain angle, which creates a circle (at least three recorded points are needed). The center points of the circles are A'_i .

2) Defining the x-y plane of the base frame F_b.

   The x-y plane of the base frame F_b is defined to be parallel to the floor. The planar surface of the base platform is applied as the x-y plane in our application. All the center points A'_i are projected onto the x-y plane, which denotes the center points of revolute joints A_i in kinematic model as shown in Figure 3.2. 6-RSS Parallel Robot Mechanism.

3) Determining the origin point of the base frame F_b.

   The projected center points A_i define a circle whose center point is the origin point of the base frame F_b.

4) Defining orientation of the base frame F_b.

   The x-axis or y-axis of the base frame F_b are defined by the center points of revolute joints A_i. Two of the projected center points A_2 and A_3 are connected to defind the mid-point of the line A_2A_3. The x-axis is along the line between the origin point the base frame F_b and the mid-point of the line A_2A_3. The direction is from the origin point to the mid-point. The z-axis is perpendicular to the x-y plane and the direction is from the origin point of the base fame F_b to the upper platform.

Hence, the definition of the base frame F_b of the referential model is finished.

The sequences of defining the tool frame F_t^P of the upper platform is shown as following:

1) Determining the center points of the spherical joints attached on the upper platform T_i.

   A minimum of four surface points of one spherical joint are detected and recorded using Handy Probe by touching the surface of the joint. The center points of the spherical joints attached on the upper platform T_i can be defined by these points located on the spherical surface.

2) Defining the x-y plane of the tool frame F_t^P.

Several points on the planar surface of the upper platform are detected using Handy Probe by touching the top surface of the upper platform. In order to increase the accuracy of the defined plane, at least four asymmetric points with longer distances among them are required. Such plane is defined as the x-y plane of the tool frame F_t^P.

3) Defining the origin point of the tool frame F_t^P.

   All the center points of the spherical joints T_i are projected onto the x-y plane. Due to the structure of the RSS parallel robot, these projected points can determine a circle whose center point denotes the origin point of the tool frame F_t^P.

4) Defining orientation of the tool frame F_t^P.

   Using the center points of the spherical joints T_i on the upper platform, the x-axis or y-axis of the tool frame F_t^P can be defined. Connecting two of the projected center points T_2 and T_3, the projected mid-point of the line T_2T_3 on the x-y plane can be found. The x-axis is along the line between the origin point the tool frame F_t^P and the projected mid-point of the line T_2T_3 on the x-y plane. The direction is from the origin point to the projected mid-point. The z-axis is perpendicular to the x-y plane and the direction is from the base platform to the origin point of the tool frame F_t^P.

To this end, the definition of the tool frame F_t^P of the parallel robot is finished.

5.3.2 Frame Definitions of the Serial Robot

In order to track the pose of the end-effector of the serial robot, the tool frame F_t^S of the serial robot should be defined first. The default tool frame F_t^S of the serial robot is defined at the center of the flange of the 6^{th} joint. The process of defining the tool frame F_t^S of the serial robot is shown as following:

1) Determining the origin point of the tool frame F_t^S.

   The relative position between the center point of the flange and the press point of the compression roller on the fiber processing head needs to be identified. Then, a tool frame F_t^S with origin point at the press point of the compression roller can be defined by offsetting the default tool frame F_t^S with such relative position information.

2) Defining the orientation of the tool frame F_t^S.

The z-axis of the tool frame F_t^S is perpendicular to the surface of the flange. The x-axis of the tool frame F_t^S can be defined by the intersection line between the two planar surfaces of the fiber processing head, as shown in Figure 5.3. These two planar surfaces are detected using Handy Probe by touching the end probe to the surface of the objects.

To track the tool frame F_t^S during the experimental process, a minimum of four targets on the end-effector should be observed by C-track all the time.

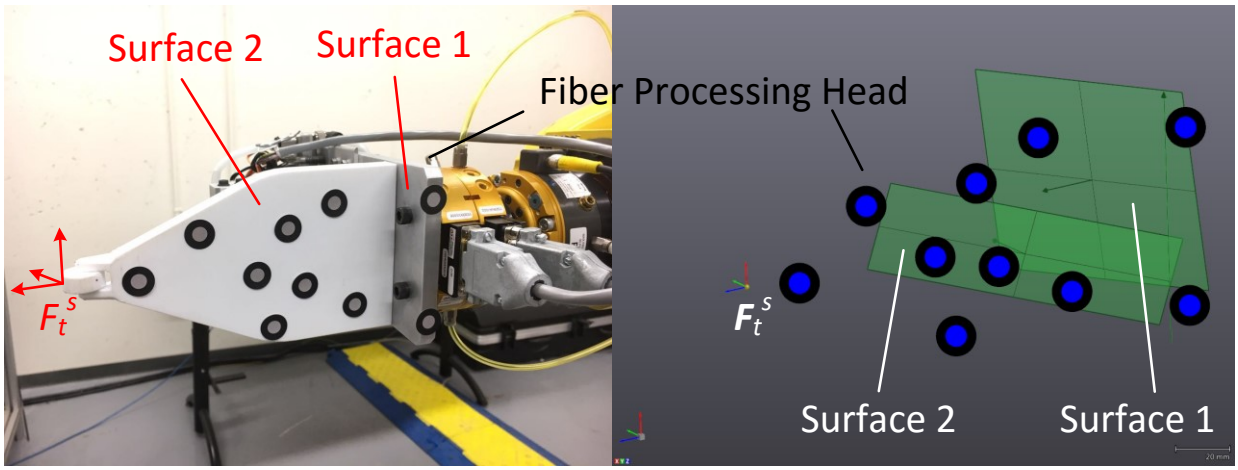

Figure 5.3. Frame Definitions of the Serial Robot

Because there is no relative movement between the base of the serial robot and the base of the parallel robot, the base frame F_b of the serial robot can be defined the same as that of the parallel robot.

5.4 Kinematic Parameters Calibration

The kinematic parameters of the parallel robot used in the inverse kinematic model and CAD model were measured by the ruler, which means those parameters are not accurate enough and might result in control errors. In order to refine the kinematic model and reduce the errors, some parameters have to be calibrated by C-track. There are two measuring volumes for C-track780, provided by Creaform Inc., which are 7.8 m^3 and 3.8 m^3. The accuracy is up to 0.025 mm. The single point repeatability is 0.055 mm for measuring volume 7.8 m^3, and 0.050 mm for the

measuring volume 3.8 m^3. The volumetric accuracy is 0.085 mm for measuring volume 7.8 m^3 and 0.080 mm for measuring volume 3.8 m^3.

I. Calibration process of the length L_{BT}:

1) Detecting center points of the spherical joints of the RSS parallel robot.

A minimum of four surface points of one spherical joint are detected and recorded using Handy Probe by touching the surface of the joint. The center points of the spherical joints attached on the upper platform T_i $(i = 1, 2, 3 \dots, 6)$ and the spherical joints attached on the proximal links B_i $(i = 1, 2, 3 \dots, 6)$ can be defined by these points located on the spherical, as shown in Figure 5.4.

2) Creating lines $L_{B_iT_i}$.

The center points of the spherical joints with the same subscripts $(B_1T_1, B_2T_2, B_3T_3, \dots, B_6T_6)$ are connected and generated 6 lines $L_{B_iT_i}$.

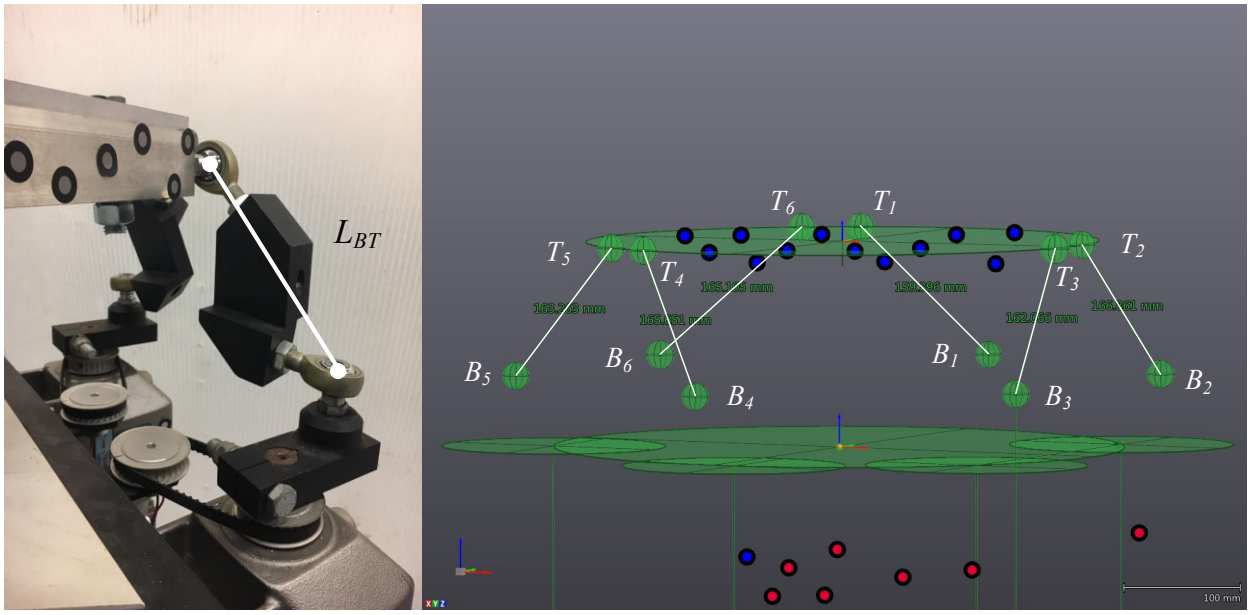

Figure 5.4. Calibration of the Length L_{BT}

3) Calibrating the length L_{BT}.

The 6 lines $L_{B_iT_i}$ are measured in VXelements software. The average value of these lines $L_{B_iT_i}$ is calculated, which is the calibrated length L_{BT} as shown in Table 5-1. The length L_{BT} represents L the kinematic model shown in Figure 3.3. Thus, the result is $L = 163.724$.

Table 5-1. Length $L_{B_iT_i}$

$L_{B_iT_i}$	$i = 1$	$i = 2$	$i = 3$	$i = 4$	$i = 5$	$i = 6$	**Average**
(mm)	159.396	166.861	162.066	165.651	163.263	165.105	163.724

II. Calibration process of the length L_{AB}:

1) Detecting center points of the spherical joints attached on the proximal links B_i.

   As mentioned above, a minimum of four surface points of one spherical joint are detected and recorded using Handy Probe by touching the surface of the joint. The center points of the spherical joints attached on the proximal links B_i $(i = 1, 2, 3 \dots, 6)$ can be defined by these points located on the spherical, as shown in Figure 5.5.

2) Finding the center points of revolute joints A_i.

   A magnetic target is attached on the proximal link of the revolute joint. The magnetic target is detected and recorded every time of moving the motor for a certain angle, which creates a circle (at least three recorded points are needed). The center points of the circles are projected onto the x-y plane, which creates the center points of revolute joints A_i in kinematic model.

3) Measuring the length $L_{A_iB_i}$.

   The length $L_{A_iB_i}$ are the distances between two set of lines. One set of lines are perpendicular to the x-y plane and pass though the center points of the spherical joints B_i are created. And the other set of lines are perpendicular to the x-y plane and pass though the center points of revolute joints A_i. Apparently, the length $L_{A_iB_i}$ represents r the kinematic model shown in Figure 3.3.

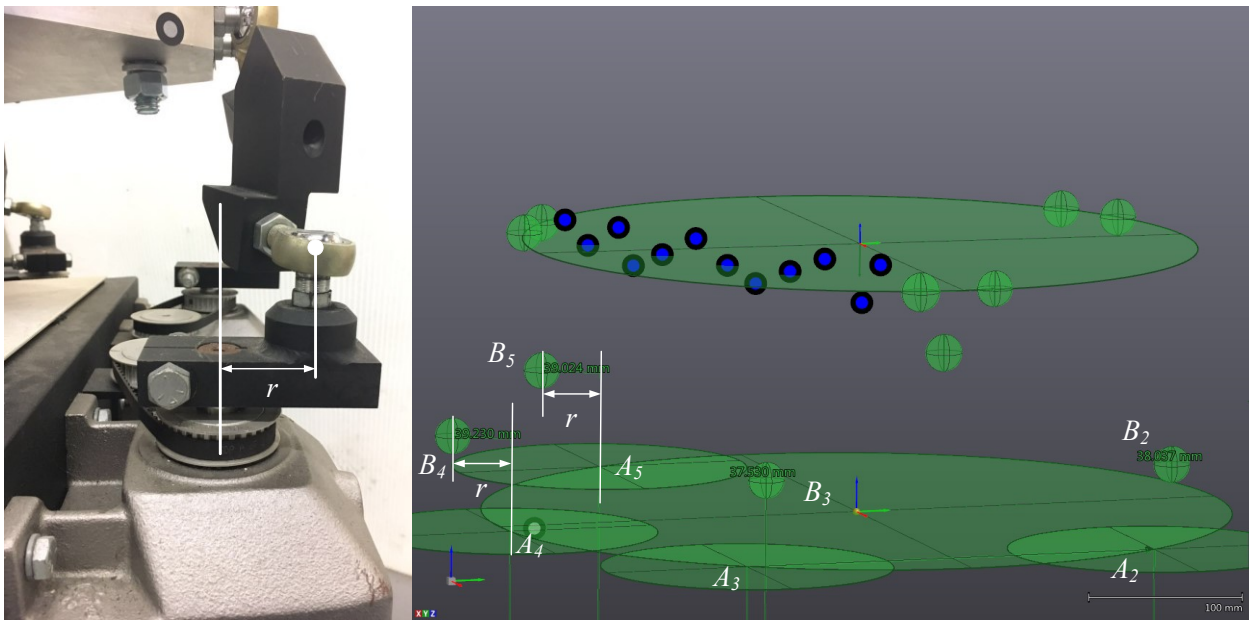

Figure 5.5. Calibration of the Length L_{AB}

4) Calibrating the length L_{AB}.

Lines $L_{A_iB_i}$ are measured in VXelements software. The average value of these lines $L_{A_iB_i}$ is calculated, which is the calibrated length L_{AB}, as shown in Table 5-2. Due to the structure of the parallel robot, only four motors can be observed by C-track at the same time. Thus, the result is $r = 38.455$.

Table 5-2. Length $L_{A_iB_i}$

$L_{A_iB_i}$	$i = 2$	$i = 3$	$i = 4$	$i = 5$	**Average**
(mm)	38.037	37.530	39.230	39.024	38.455

III. Calibration process of the distances between six vertices of the upper platform T_i:

1) Determining the center points of the spherical joints attached on the upper platform T_i.

As mentioned above, the center points of the spherical joints attached on the upper platform T_i $(i = 1, 2, 3 \ldots, 6)$, which are the vertices of the upper platform, can be defined by the points on the surface of the spherical joints detected by Handy Probe, as shown in Figure 5.6.

2) Creating lines by connecting the six vertices

The center points of the spherical joints attached on the upper platform T_i $(i = 1, 2, 3 \dots, 6)$ are connected in sequence, which creates lines $L_{T_iT_{i+1}}$ $(i = 1, 2, 3 \dots, 5)$. Among these lines, $L_{T_2T_3}$, $L_{T_4T_5}$, $L_{T_1T_6}$ are denoted as a, and $L_{T_1T_2}$, $L_{T_3T_4}$, $L_{T_5T_6}$ are denoted as c in kinematic model shown in Figure 3.2.

3) Calibrating the lengths a and c.

The lengths of $L_{T_2T_3}$, $L_{T_4T_5}$, $L_{T_1T_6}$ and $L_{T_1T_2}$, $L_{T_3T_4}$, $L_{T_5T_6}$ are measured in VXelements software. The average values of these lines $L_{T_iT_{i+1}}$ are calculated respectively, which is the calibrated lengths a and c, as shown in Table 5-3. Thus, the results are $a = 50.767$, and $c = 353.883$.

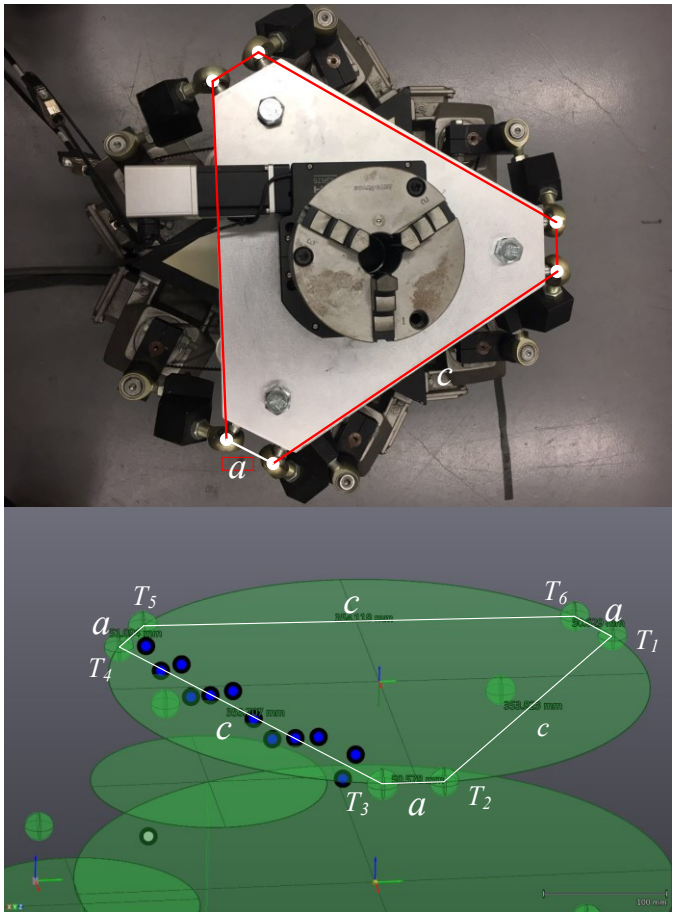

Figure 5.6. Calibration of Lengths a and c

Table 5-3. Lengths $L_{T_iT_{i+1}}$

$L_{T_iT_{i+1}}$	$L_{T_2T_3}$	$L_{T_4T_5}$	$L_{T_1T_6}$	$L_{T_1T_2}$	$L_{T_3T_4}$	$L_{T_5T_6}$
(mm)	50.578	51.094	50.629	353.823	353.707	354.118
Parameters	a			c		
Average	50.767			353.883		

IV. Calibration process of the distances between six vertices of the base platform A_i:

1) Determining the center points of revolute joints A_i.

As mentioned above, the center points of the circles created by moving motors and recording the positions of the magnetic targets attached on the proximal links using Handy Probe. These center points are projected on the x-y plane of the base frame F_b, which define the center points of the revolute joints A_i, as shown in Figure 5.7. Only four center points of the revolute joints can be observed by C-track.

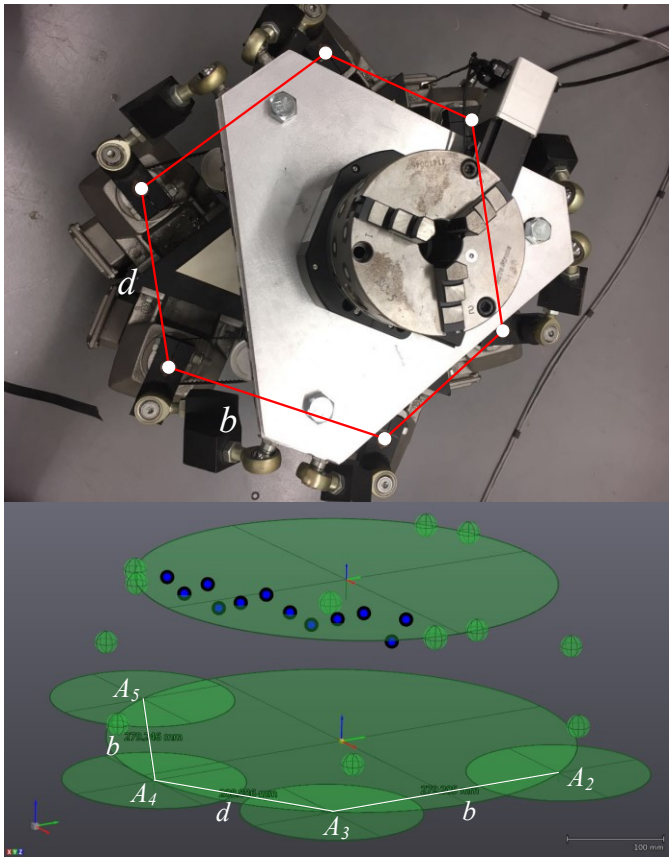

Figure 5.7. Calibration of Lengths b and d

2) Creating lines by connecting the four revolute joints.

The center points of the revolute joints A_i $(i = 2, 3, 4, 5)$ are connected in sequence, which creates lines $L_{A_iA_{i+1}}$ $(i = 2, 3, 4)$. Among these lines, $L_{A_2A_3}$, $L_{A_4A_5}$ are denoted as b, and $L_{A_3A_4}$ are denoted as d in kinematic model shown in Figure 3.2.

3) Calibrating the lengths b and d.

The lengths of $L_{A_2A_3}$, $L_{A_4A_5}$ and $L_{A_3A_4}$ are measured in VXelements software. The average values of these lines $L_{A_iA_{i+1}}$ are calculated and the calibrated lengths b and d are shown in Table 5-4, which are $b = 279.226$, and $d = 208.886$.

Table 5-4. Lengths $L_{T_iT_{i+1}}$

$L_{A_iA_{i+1}}$	$L_{A_2A_3}$	$L_{A_4A_5}$	$L_{T_3T_4}$
(mm)	279.205	279.246	208.886
Parameters	b		d
Average	279.226		208.886

V. Calibration process of the length L_z:

The lengths from the center points of the spherical joints attached on the proximal links B_i to the top surface of the proximal links are neglected to simplify the kinematic model of the 6-RSS parallel robot because the length L_z is constant during the operation of the parallel robot. However, in order to determine the distance from the center points of the spherical joints B_i to the x-y plane of the base frame F_b and build more accurate CAD model, the precise length L_z is required.

1) Determining the center points of the spherical joints attached on the proximal links B_i.

the As mentioned above, the center points of the spherical joints attached on the proximal links B_i $(i = 1, 2, 3 \ldots, 6)$ can be defined by the points on the surface of the spherical joints detected by Handy Probe.

2) Creating the top planar surfaces of the proximal links.

At least four asymmetric points on each of the top surface of the proximal links are detected using Handy Probe by touching method. The planar surfaces are created by these detected points, as shown in Figure 5.8.

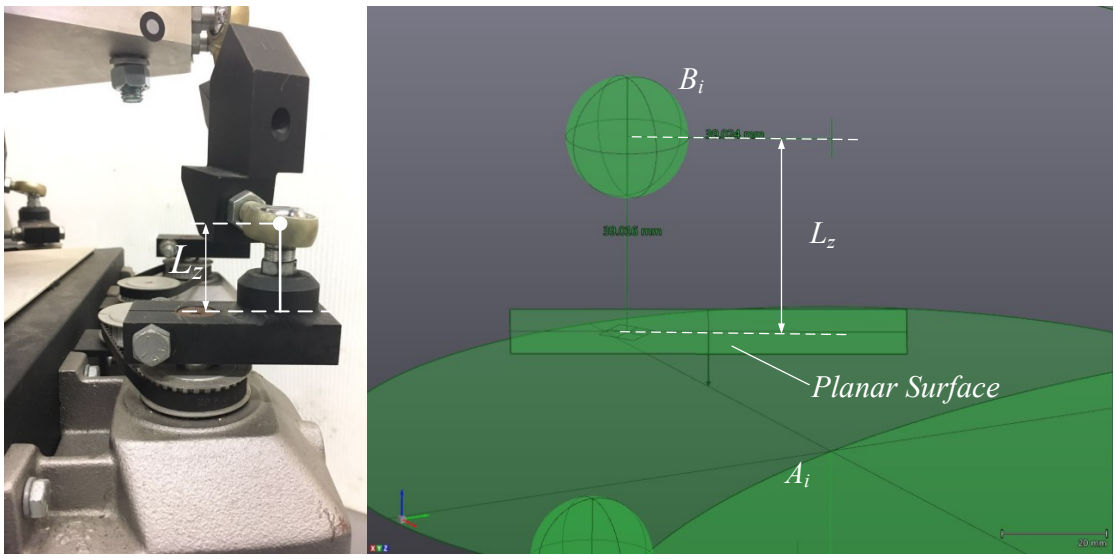

Figure 5.8. Measurement of the length L_{z_i}

3) Measuring the lengths L_{z_i}.

The distances from the center points of the spherical joints B_i to the created planar surfaces which are the top surface of the proximal links are measured in VXelements software, as shown in Figure 5.9.

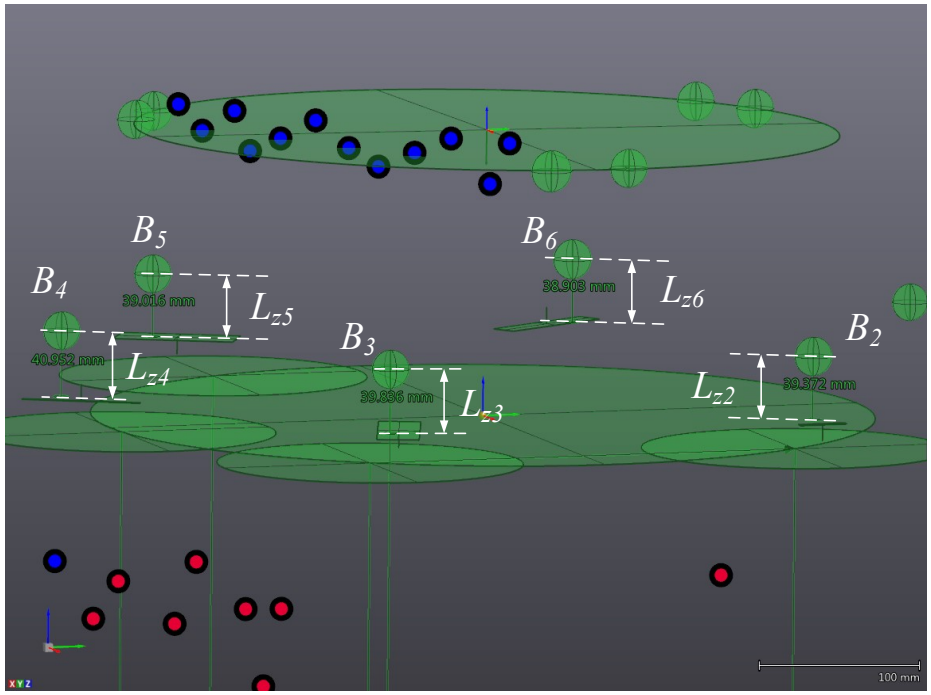

Figure 5.9. Calibration of the length L_z

4) Calibrating the length L_z.

The average value of these lines L_{z_i} is calculated, which is the calibrated length L_z, as shown in Table 5-5. The sixth length cannot be observed by C-track. Thus, the result is $L_z = 39.616$.

Table 5-5. Length $L_{A_iB_i}$

L_{z_i}	$i = 2$	$i = 3$	$i = 4$	$i = 5$	$i = 6$	**Average**
(mm)	39.372	39.836	40.952	39.016	38.903	39.616

5.5 Summary

In order to measure the accurate poses of both robots in the cooperative AFP system for precise pose tracking, a photogrammetry sensor, i.e. C-track provided by Cramform Inc. is used in this project. The pose estimation of an object is obtained from the output of C-track, which observes at least four coplanar or non-coplanar targets. Then, the processes of the frame definitions for both the parallel robot and the serial robot are presented. Moreover, in order to refine the kinematic model and the CAD model of the 6-RSS parallel robot, some kinematic parameters in parallel robot modelling are calibrated using C-track. The VXelements provided by Creamform Inc. is used for the visual tracking modelling of the parallel robot and the serial robot.

With the poses feedback acquired by the photogrammetry sensor, the semi-offline trajectory synchronized algorithm will be introduced in the next chapter.

CHAPTER 6

6 SEMI-OFFLINE TRAJECOTRY SYNCHRONIZED ALGORITHM

6.1 Introduction

In the cooperative robot system, trajectories should be generated for each robot. Plenty of researches have focused on the trajectory planning with collision-free and singularities-free for robots. However, when the manufactured composite part is of complicated shape, it becomes increasingly difficult to generate the trajectories for both robots which are free from collision and singularities, and meanwhile, satisfy the requirements for fiber placement. These requirements include considering the limitation of minimum turning radius, defects resulted from gaps and overlaps, multiple layers, continuous laying without cutting tows to keep the consistent stress, and keeping the roller of the fiber process head perpendicular to the surface of the mold all the time. In certain cases, no feasible trajectory can be generated for the continuous fiber placement. The traditional practice, namely, off-line generating path and inputting the generated path to robot controller for on-line fiber placement, cannot fulfil the task of manufacturing complicated composite components by the cooperative AFP system.

To meet the challenge, a semi-offline trajectory synchronized algorithm is proposed to incorporate the on-line robot control in following the paths generated off-line especially when the generated paths are infeasible for the current multiple-robots to realize due to the constraints, singularities and other requirements for fiber placement. By adjusting the pre-planned paths of the robots at the points where the collision, limitation and singularity occur on-line, the fiber can be laid up continuously without interruption. The correction is calculated based on the pose tracking data of the parallel robot and the serial robot detected by the photogrammetry sensor on-line. Due to the

flexibility of the 6-DOF parallel robot, the optimized offsets with varying orientation and translation movements are generated based on the different singularities and constraints, as well as the current pose of the serial robot's end-effector.

In this chapter, the control structure regarding a semi-offline trajectory synchronized algorithm is introduced for a cooperative AFP system consisting of a 6-DOF serial robot holding the fiber placement head, a 6-RSS parallel robot on which a one-DOF mandrel holder is installed at first. Secondly, the synchronization function for the cooperative AFP system is presented to maintain the certain kinematic relationships amongst robots in Section 6.3. Thirdly, the off-line trajectory planning and the decomposition processes for the cooperative AFP system are illustrated in Section 6.4. Then, the procedures of the generation offsets for the parallel robot are given in Section 6.5. The offsets are generated based on different conditions including singularity avoidance and joints constraints avoidance. A photogrammetry sensor is adopted to detect the poses of the end-effectors on parallel robot and serial robot. Accordingly, the compensation pose calculation process is proposed in Section 6.6. Based on the measured poses of both the serial robot and the parallel robot, a pose correction is calculated and added to the pre-planned trajectory for avoiding singularities, optimizing joint limits, and expanding the workspace of the whole system online.

6.2 Control Structure

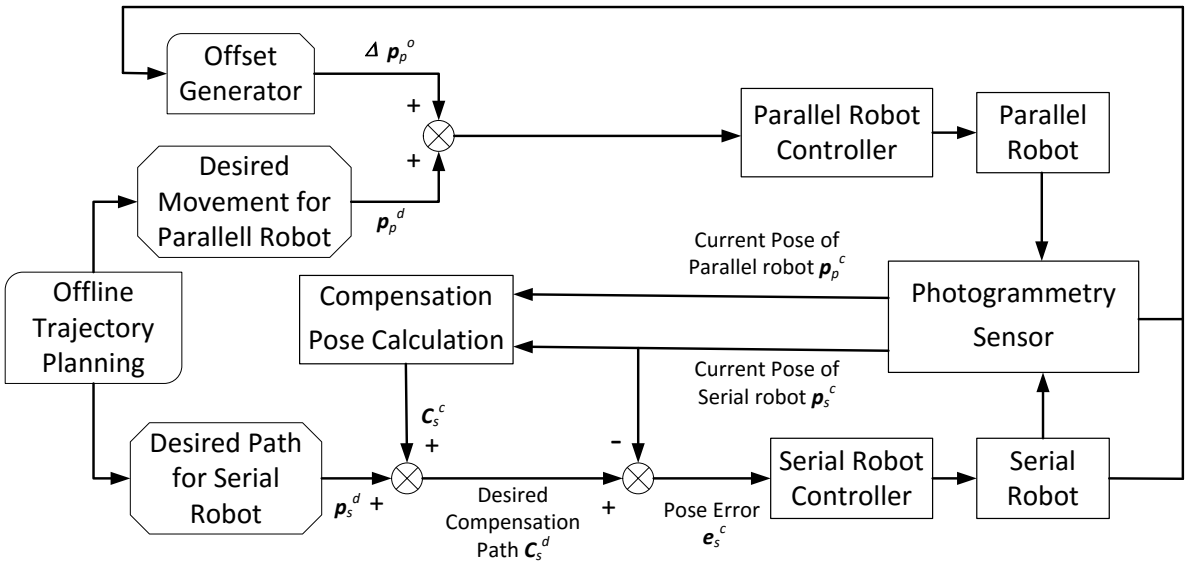

Figure 6.1. Semi-offline Trajectory Synchronized Algorithm Diagram

A novel visual based synchronized algorithm is presented to achieve the coordination of two robots in the cooperative AFP system. The off-line trajectory planning of serial robot can be adjusted according to the offsets of parallel robot in real-time and the certain kinematic relationships between them is maintained in the meantime. As shown in Figure 6.1, the off-line trajectory planning is generated at first, which consists of the desired path for serial robot, the desired movement for parallel robot and the 1-DOF rotary stage. The photogrammetry sensor detects the poses of the tool frames of both serial robot and parallel robot for compensation and offset calculation. The "offset generator" block outputs the offset signal to move the parallel robot based on the received condition information on the constraints and singularities of the serial robot and the current poses observed by the photogrammetry sensor. The offset of the 6-RSS parallel robot varies according to the current pose of the index frame attached on the joints of the serial robot. The "compensation pose calculation" block computes the pose correction based on the current measured pose information of tool frames of serial robot and parallel robot and adds the correction to the pre-planned trajectory of the serial robot. The "serial robot controller" block produces the control input for serial robot based on the current pose error.

6.3 Synchronization Function

Basically, multi-robots coordination is to maintain the certain kinematic relationships amongst them. The pose of i^{th} robot is denoted as $\boldsymbol{p}_i(t) = (x_t, y_t, z_t, \alpha_t, \beta_t, \gamma_t)$, where $i = 1 \cdots n$. Assume that the coordinated robots are subject to the following synchronization function [149]

$$\mathcal{R}\{\boldsymbol{p}_{i\cdots n}(t) | f(\boldsymbol{p}_1(t), \boldsymbol{p}_2(t), \dots, \boldsymbol{p}_n(t)) = 0\} \quad (6\text{-}1)$$

Apparently, Eq. (6-1) with the desired poses $\boldsymbol{p}_i^d(t)$ can be written as following,

$$\mathcal{R}\left\{\boldsymbol{p}_{i\cdots n}^d(t) \middle| f\left(\boldsymbol{p}_1^d(t), \boldsymbol{p}_2^d(t), \dots, \boldsymbol{p}_n^d(t)\right) = 0\right\} \quad (6\text{-}2)$$

The pose error $\boldsymbol{e}_i(t)$ is obtained by

$$\boldsymbol{e}_i(t) = \boldsymbol{p}_i^d(t) - \boldsymbol{p}_i(t) \quad (6\text{-}3)$$

where $\boldsymbol{p}_i^d(t)$ is the desired pose trajectory. $f\big(\boldsymbol{p}_1(t), \boldsymbol{p}_2(t), \dots, \boldsymbol{p}_n(t)\big)$ can be expanded at the desired poses $\boldsymbol{p}_i^d(t)$ by using a Taylor series expansion,

$$\begin{aligned} & f\big(\boldsymbol{p}_1(t), \boldsymbol{p}_2(t), \dots, \boldsymbol{p}_n(t)\big) \\ & \quad = f\left(\boldsymbol{p}_1^d(t), \boldsymbol{p}_2^d(t), \dots, \boldsymbol{p}_n^d(t)\right) \\ & \quad + \sum_{i=1}^{n}\left[\frac{\partial f}{\partial \boldsymbol{p}_i}|_{\boldsymbol{p}_i^d}\left(\boldsymbol{p}_i(t) - \boldsymbol{p}_i^d(t)\right) + \Phi\big(\boldsymbol{p}_i(t)\big)\right] \\ & \quad = \sum_{i=1}^{n}\left[-\frac{\partial f}{\partial \boldsymbol{p}_i}|_{\boldsymbol{p}_i^d}\boldsymbol{e}_i(t) + \Phi\big(\boldsymbol{p}_i(t)\big)\right] \end{aligned} \qquad (6\text{-}4)$$

where $\Phi\big(\boldsymbol{p}_i(t)\big)$ is higher order terms. Thus, the synchronization function of the coordinated robots becomes

$$\sum_{i=1}^{n}\left[\delta_i(t)\boldsymbol{e}_i(t) + \Phi\big(\boldsymbol{p}_i(t)\big)\right] = 0 \qquad (6\text{-}5)$$

where $\delta_i(t) = -\frac{\partial f}{\partial \boldsymbol{p}_i}|_{\boldsymbol{p}_i^d}$ denotes a diagonal coupling parameter regarding the first-order error $\boldsymbol{e}_i(t)$ and is bounded. Eq. (6-5) must be satisfied in order to achieve the multi-robots coordination control.

In our project, the serial robot is required to track its off-line generated desired trajectories when the parallel robot is stationary. When the parallel robot is moving, the desired trajectories of the serial robot is adjusted to maintain a certain kinematic relationship with parallel robot. The pose trajectories of the two robots are subject to a synchronization function, which is

$$f\left(\boldsymbol{p}_s(t), \boldsymbol{p}_p(t)\right) = \boldsymbol{p}_s(t) - \boldsymbol{p}_p(t) - \boldsymbol{\psi}_s(t) - \boldsymbol{\rho} = 0 \qquad (6\text{-}6)$$

where $\boldsymbol{p}_s(t)$ and $\boldsymbol{p}_p(t)$ denote the pose trajectories of the serial robot and the parallel robot in reference to the base frame F_b respectively, $\boldsymbol{\psi}_s(t)$ represents the relative kinematic relationship of the tool frame of the serial robot F_t^S with respect to the tool frame of the parallel robot F_t^P, which in fact is the task trajectory and is defined offline, $\boldsymbol{\rho}$ denotes the constant difference between the tool frame of the serial robot F_t^S and the tool frame of the parallel robot F_t^P.

According to Eq. (6-5), Eq. (6-6) is equivalent to making the pose errors $\boldsymbol{e}_s(t)$ and $\boldsymbol{e}_p(t)$ satisfy

$$\boldsymbol{\varepsilon}(t) = \boldsymbol{e}_s(t) - \boldsymbol{e}_p(t) = 0 \qquad (6\text{-}7)$$

where $\boldsymbol{\varepsilon}(t)$ represents synchronization error. In order to achieve the coordination control of the two robots with a certain relative movement, it is required that $\boldsymbol{\varepsilon}(t) \to 0$ during the movement process and achieving $\boldsymbol{e}_s(t) \to 0$ and $\boldsymbol{e}_p(t) \to 0$.

6.4 Off-line Trajectory Planning and Decomposition

6.4.1 Off-line Trajectory Planning

Because of the large range of applications and sensitivity on manufacturing parameters of composites structures, trajectory planning of the AFP tool head is a critical aspect to produce a reliable and high performance final product. Generally, the methodology of the trajectory planning for fiber lay-up formulates a reference curve on the mold surface at first, and the reference curve is subsequently shifted to produce the different courses composing the ply. The computation of this reference course is usually done by intersecting a reference plane with the mold surface [6, 150, 151], mapping a 2D curve onto it [105, 152], or using parametric functions [107]. Once this initial path is formulated, it can be shifted along the direction of a defined axis to generate the remaining courses [153]. However, this method cannot produce perfectly parallel trajectories in all cases, which may result in gaps and overlaps in the ply. To address this issue, another method is proposed: once the reference path is known, the next course is computed by offsetting the original one of a constant magnitude in a direction locally perpendicular to the curve. The offset distance is the total width of tows for multiple tows lay-up. The offset path should be extended to the boundary when it does not reach the surface boundary or falls outside the range of the mold [2]. [6] produces a uniform lay-up on open contoured surfaces without any gaps or overlaps by using this method.

For a given free-form shaped structure, the initial path is formulated by the surface-plane intersection strategy. The major axis $\boldsymbol{K} = [K_x \quad K_y \quad K_z]^T$ is specified to pass through the point $\boldsymbol{X} = [X_x \quad X_y \quad X_z]^T$, then a projection $\boldsymbol{P} = [P_x \quad P_y \quad P_z]^T$ of the major axis forms the reference plane is given by,

$$\boldsymbol{P}(x, y, z) = ax + by + cz + d = 0 \qquad (6\text{-}8)$$

where $[a \quad b \quad c]^T = \boldsymbol{K} \times \boldsymbol{P}$, and $d = -\boldsymbol{X} \cdot [a \quad b \quad c]^T$.

The surface-plane intersection equation can be formed by substituting the parametric equation of the mold surface $S(u, v) = [x(u, v) \quad y(u, v) \quad z(u, v)]^T$ into Eq. (6-8),

$$f(u, v) = ax(u, v) + by(u, v) + cz(u, v) + d = 0 \qquad (6\text{-}9)$$

which is defined by the set of parameters u and v.

By solving Eq. (6-9), the coordinates of the intersection points (u, v) are obtained.

The bowl shape is used as the mandrel in simulation. The initial path is a straight line on the x-z plane while trajectory planning for producing the planar surface of the bowl-shaped mandrel, shown in Figure 6.2 A.

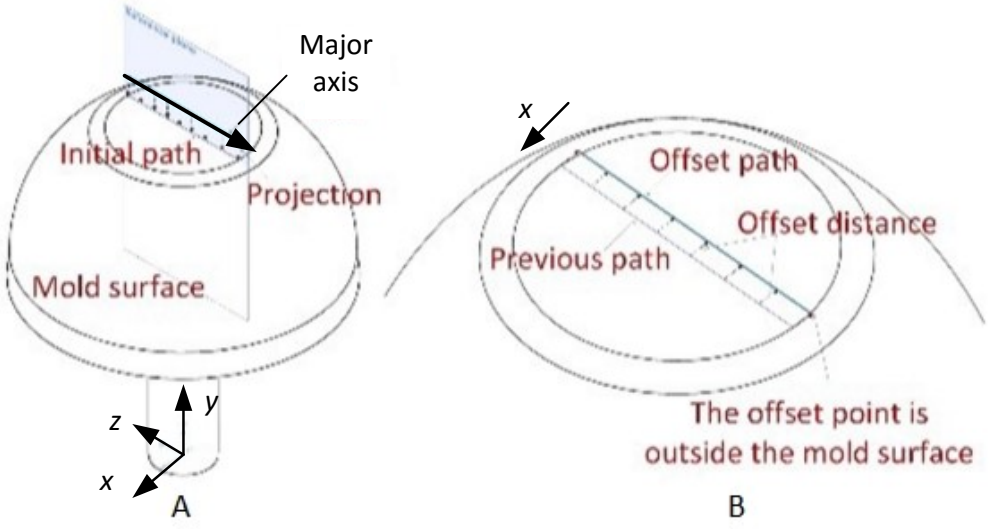

Figure 6.2. The Trajectory Planning for the Planar Surface

To achieve a uniform AFP path over a mold, the neighboring paths must be offset along the surface a distance of the total width of tows in a perpendicular direction from the given path. For the free-form shaped structure, the offset direction at one point is actually a curve, which is along the mold and perpendicular to the reference path at that point. This curve is formulated by surface-plane

intersection strategy as well. However, for the plane surface case, the offset direction is along x direction on the x-z plane, as shown in Figure 6.2 B.

Normally, there are two reasons for the incomplete offset. The first is that the offset points fall outside the range of the mold. The other reason is that the original points are not on the mold. The offset path should be extended to the boundary by calculating the extrapolated points and adding them to the existing points when it does not reach the surface boundary.

For the curved surface of the bowl, the planning path for the end effector of the serial robot is formulated by the surface-plane intersection strategy, shown in Figure 6.3.

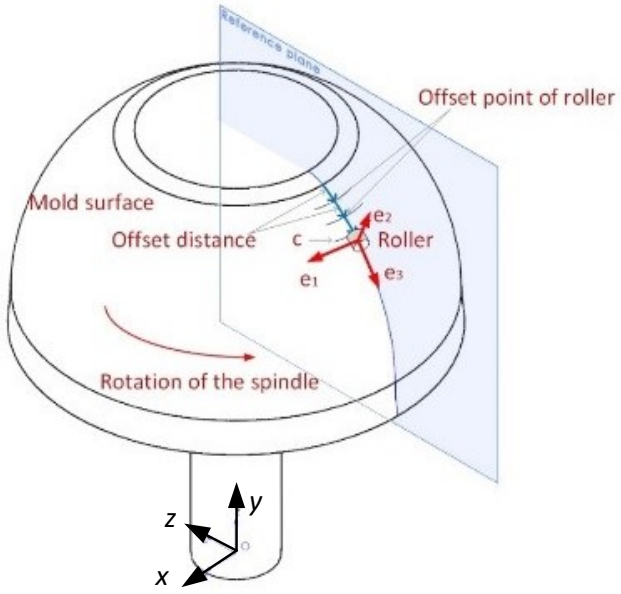

Figure 6.3. The Trajectory Planning for the Curved Surface

The Frenet-Frame at the offset point could be defined as

$$\boldsymbol{e}_1 = [e_{1x} \quad e_{1y} \quad e_{1z}]^T = \frac{\boldsymbol{c}'(t)}{|\boldsymbol{c}'(t)|} \tag{6-10}$$

$$\boldsymbol{e}_2 = [e_{2x} \quad e_{2y} \quad e_{2z}]^T = \frac{\boldsymbol{n}'(t)}{|\boldsymbol{n}'(t)|} \tag{6-11}$$

$$\boldsymbol{e}_3 = [e_{3x} \quad e_{3y} \quad e_{3z}]^T = \boldsymbol{e}_2(t) \times \boldsymbol{e}_1(t) \tag{6-12}$$

where $\boldsymbol{e}_1$ is the unit vector tangent to the curve; $\boldsymbol{e}_2$ is the normal unit vector which guarantees the roller would always be normal to the mold surface; $\boldsymbol{e}_3$ is the bi-normal unit vector which is the offset direction in this case.

Additionally, the off-line trajectories on Y-shape mandrel with different placement angles are generated in the previous work [154] done by Polytechnique research group. The proposed two trajectory generation algorithms cover two branches of the Y shaped mandrel with a single course. The first algorithm aims to generate paths of constant angle with respect to the revolution axis of the associated cylinder. The second algorithm allows for the definition of a maximum geodesic curvature for the path in order to avoid fiber buckling during steering.

A. Constant Placement Angle

Normally, standard orientation is used in industry to define the different plies of the laminate. In this project, the ply definition is extended to multiple-axis bodies. Similarly to planar surfaces, the ply orientation can be defined with respect to a reference direction. Considering the geometry of the Y-shape mandrel, a natural choice for this reference is the axes of the cylinders. Three ply orientations are chosen as examples, which are 0° (parallel to the cylinder axis), 45° and 90°. In order to obtain a continuous course, the 90° ply is approximated by a helix with a pitch equal to the width of the course, which means that the actual placement angle is slightly smaller than 90°.

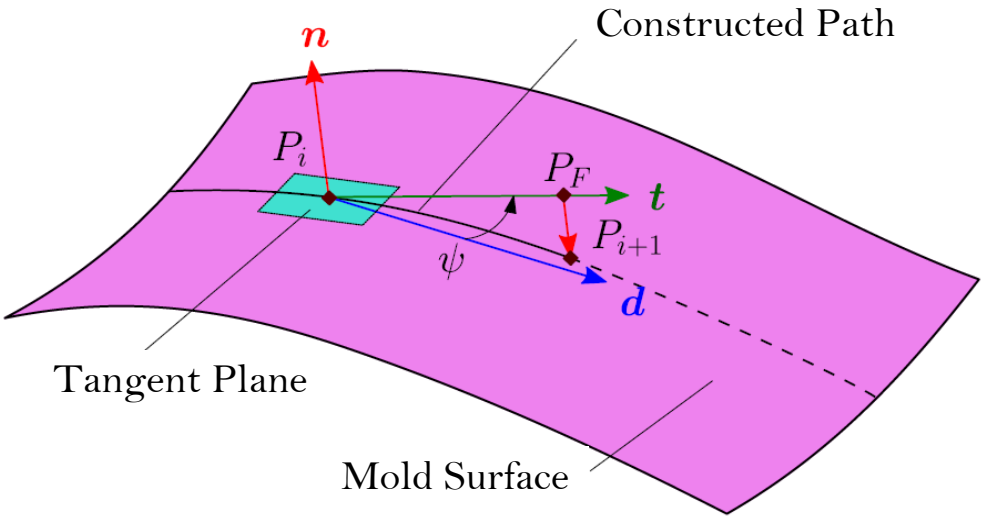

Figure 6.4. Iterative Algorithm for Trajectory Generation

For each ply, a path is defined as a constant angle helix and is constructed using an iterative algorithm introduced in [154]. The algorithm is based on a user-defined reference direction, which is the cylinder axis in the project. As shown in Figure 6.4, A vector $\boldsymbol{d}$ tangent to the surface at the current point $\boldsymbol{P}_i$ of the path and pointing towards the reference direction is estimated. A second vector $\boldsymbol{t}$ is then computed by rotating $\boldsymbol{d}$ around the surface normal vector $\boldsymbol{n}$ by the selected placement angle ψ. An intermediate point $\boldsymbol{P}_F$ is thereby computed by translating $\boldsymbol{P}_i$ along $\boldsymbol{t}$ of a small distance. Finally, $\boldsymbol{P}_F$ is projected onto the mold surface along $-\boldsymbol{n}$ to obtain the next point of the path, $\boldsymbol{P}_{i+1}$. This process stops when the boundary of the region to be covered is reached, and the final point of the path is then computed on this boundary.

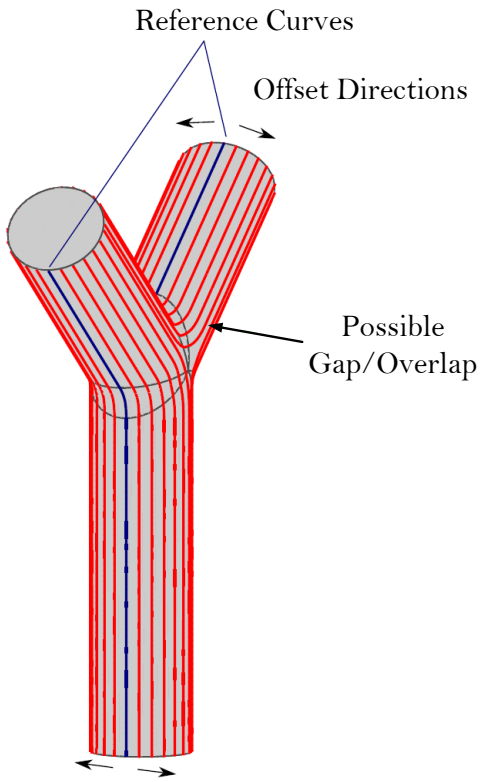

Figure 6.5. Trajectory of 0° Ply

Once the reference curve is completed, it is offset in the orthogonal direction by a geodesic distance equal to the course width by using the method proposed in [155]. Figure 6.5 illustrates the result of this method for the 0° ply.

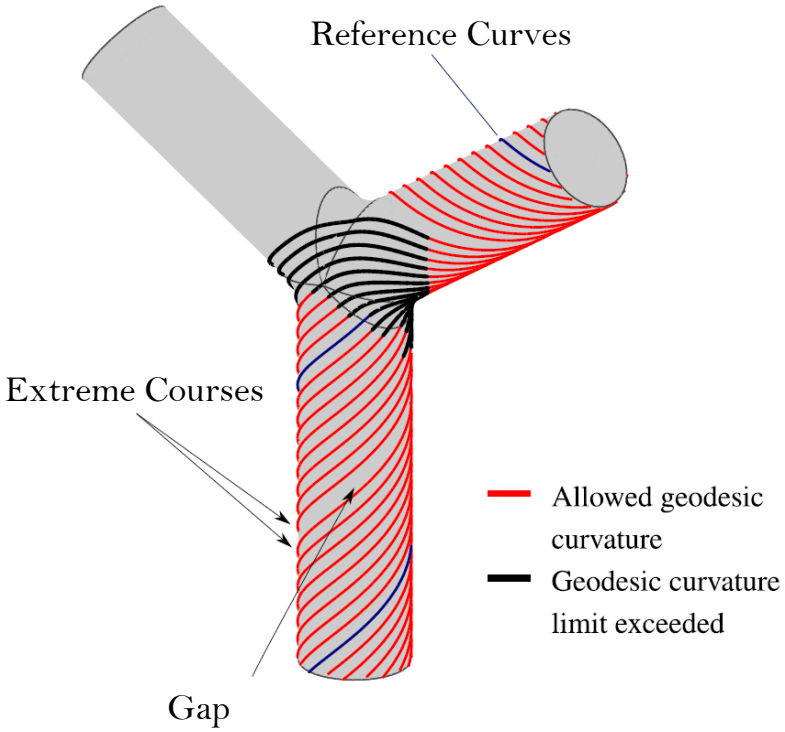

Figure 6.6. Trajectory of 45° Ply

However, one of the drawbacks of this method is that the geodesic curvature of the parallel courses can possibly become quite large, depending on the reference curve and the geometry of the part. Take the trajectory for 45° ply illustrated in Figure 6.6 for example, it shows that the further the path is from the reference curve the greater its geodesic curvature. Another issue of the offset method is the gap or overlap in other cases appeared between the extreme courses, which is shown in this figure too. The areas of the part lacking coverage depend on the starting point of the reference part, but this issue is difficult to avoid if the perimeter of the base circle of the cylinder is not a multiple of the offset distance, even with a 0°. The illustrated placement angle value leads to a partial coverage of the third branch near the junction region. The result of a 90° ply trajectory illustrates a uniform coverage of the two considered branches but a lack of fiber in the junction region, shown in Figure 6.7.

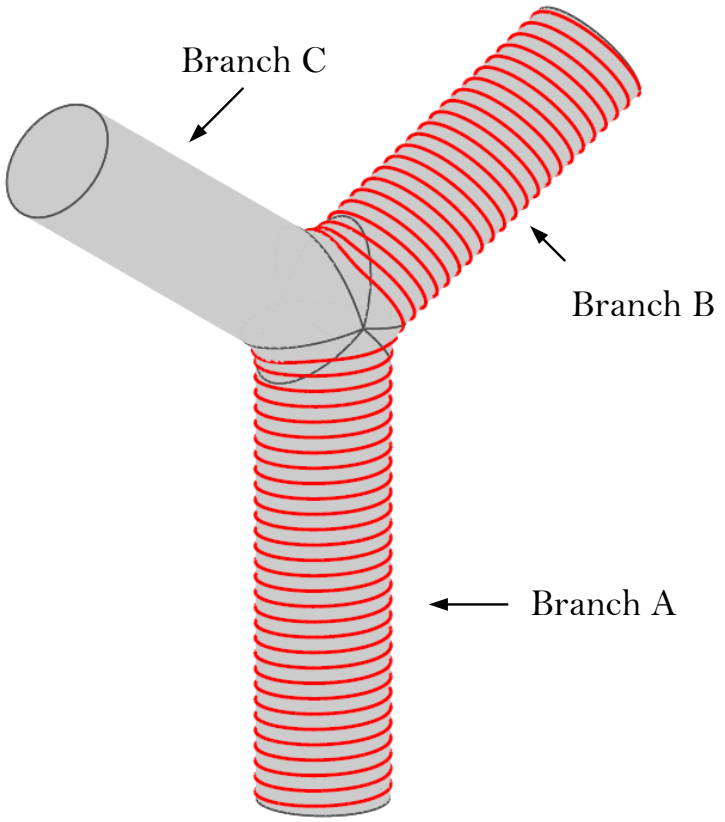

Figure 6.7. Trajectory of 90° Ply

It is possible to cover two branches with a continuous course while minimizing gaps and overlaps, and obtain a uniform coverage by using this algorithm. Nevertheless, when using 45° and 90° placement angle, a combination of plies starting from the different branches is required to obtain the same number of layers on each branch. As shown in Figure 6.7, if the three branches of the part are labeled as A, B, and C, a first trajectory will cover branches A and B but leave branch C empty. To cover branch C, another trajectory using branches B and C can be generated. Then, the Y-shape mandrel would have one layer for branch A, one layer for branch C and two layers for branch B. One more trajectory covering branches A and C will allow to obtain two layers on each branch. The main drawback of this method is its tendency to create paths with high geodesic curvature around the junction region. This can lead the fiber to buckle during manufacturing and produce parts with severe weakened mechanical properties.

B. Maximal Curvature Constraint

The trajectory is generated to cover at least two branches continuously while avoiding geodesic curvatures greater than a selected threshold by using this trajectory planning technique. The typical minimum turning radius feasible in AFP seems to be approximately $635\ mm$ for $3.175\ mm$ wide tows [156], which is used in this algorithm. However, the value can be adjusted depending on the tow width and specifications.

To ensure that the maximal curvature is not exceeded, the proposed algorithm first computes a helix path on the starting branch in order to generate a full ply. The rationale of using again a helix is that this curve is a geodesic for cylinders regardless of its pitch (i.e. it has a zero geodesic curvature.) Therefore, the path on the first branch of the Y-shape mandrel will necessarily satisfy the curvature constraint, namely to have a turning radius greater than $635\ mm$. However, once the helix reaches the junction region, this property is not necessarily satisfied anymore. Trying to pursue the iterative construction of the path, if the algorithm detects a geodesic curvature greater than the set threshold, it stops there and an optimization is run to compute the next points of the path. Three options for the continuation of the path were selectable by the user in the algorithm:

(1) move in the direction of the minimal curvature path

(2) reach a path generating a helix on the second branch with a pitch equal to the course width, within the allowable curvature limit

(3) reach a path generating a straight line on the second branch still while respecting the curvature constraint.

This algorithm is similar to the one presented above except the angle ψ is variable. Point $\boldsymbol{P}_{i+1}$ is computed from point $\boldsymbol{P}_i$ under the condition of satisfying one of the three options listed above. For each point $\boldsymbol{P}_{i+1}$, a golden section search algorithm is used to compute the placement angle ψ which minimizes a fitness function established from the desired options. The algorithm searches for an optimal value of ψ within the range of angles creating an acceptable geodesic curvature of the path. It works by sequentially narrowing down the interval in which the optimum value of ψ is assumed to be located. At each step, a new interval is defined with a length equal to the inverse of the golden ratio of the original interval, which is ≈ 0.618, and all the boundary values are tested. Using the golden ratio ensures that the spacing between tested values stays proportional to the spacing at each step of the algorithm [157]. In the case of option (1), the fitness function is simply the opposite of the radius of the circle tangent to the path computed at point $\boldsymbol{P}_i$ and belong to the

local tangent plane. For options (2) and (3) the difference between the minimal allowed curvature radius for the path and the obtained curvature radius with $\boldsymbol{P}_{i+1}$ is minimized. The optimization allows to choose a specific angle ψ which both satisfies the curvature constraint and minimizes a defined criterion. This technique is able to generate a trajectory slowly reaching the targeted placement angle ϕ.

Simulation conducted in RoboDK shows the results of trajectory generation algorithm. However, there are collision and singular points on the generated trajectories of the three constant placement angles, which cannot be used in the real experiment directly.

6.4.2 Trajectory Decomposition

Multi-robots system can respond to flexibility and adaptivity needs during manufacturing processes. It can be defined by decomposing the overall process across tasks, across robots or hybrid. The proposed cooperative AFP system is robot-based decomposition whose individual self-contained entities are the robots involved in the whole process [158].

Trajectory planning decomposition defines the trajectory of each robot independently to avoid collision with each other. However, the pressure of fiber processing head's compression roller must be normal to the surface of mandrel and the axis of the compression roller always keep perpendicular to the trajectory path during the manufacturing processes. The mandrel is mounted on the rotary stage which is fixed on the upper platform of parallel robot. The kinematic relationship between the end-effectors of two robots is pre-planned and known. As shown in Figure 6.8, when there is translation movement from the original point of parallel robot's end-effector $O_{\_P}$ to $O_{\_P'}$, the original point of serial robot's end-effector $O_{\_D}$ need to move to $O_{\_D'}$ with the same distance; when there is orientation movement from the original point of parallel robot's end-effector $O_{\_P'}$ to $O_{\_P''}$, the original point of serial robot's end-effector $O_{\_D'}$ need to move to $O_{\_D''}$ in the reference of original point $O_{\_P'}$ with the same rotational angle, which keeps the certain kinematic relationship between the poses of the two end-effectors the same. With such constraints, a proper pre-planned trajectory can free the two robots from collision during manufacturing processes, but cannot guarantee the collision-free between the robot and mandrel.

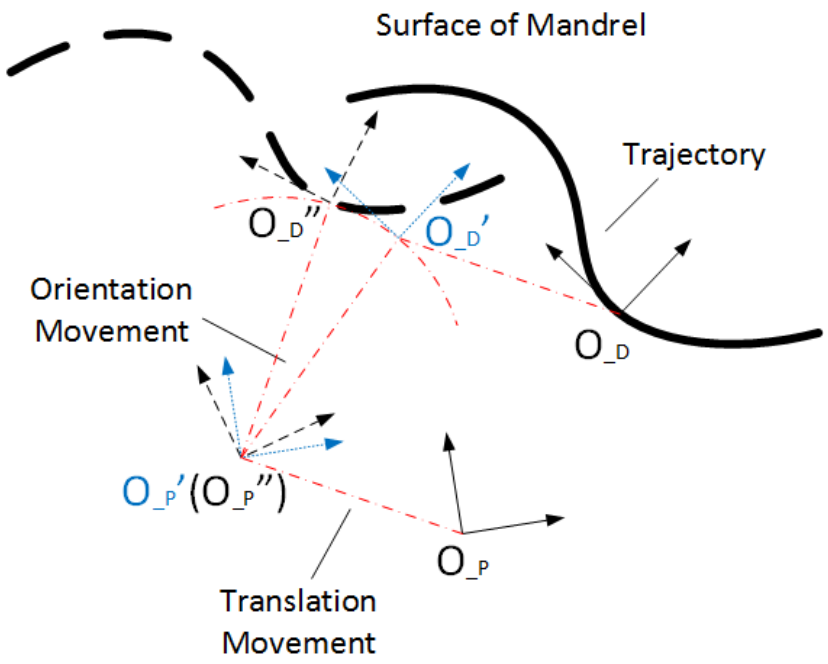

Figure 6.8. The Relative Movement between the Two End-effectors

As long as the desired path is determined, the relative pose between the two end-effectors cannot be changed. When one of the end-effector reach its pose limitation, the other end-effector can offset the gap between such limitation and the desired pose, which improves the manufacturing ability of the cooperative AFP system.

The basic principle of decomposing the multi-robot system is generating paths for each robot as simple as possible. Based on the analyses above, the desired path planning can be decomposed to trajectory of serial robot, rotary movement of rotary stage and the adjust movement of parallel robot. For example, spiral curve can be decomposed to rotary movement for rotary stage and line for serial robot as the trajectory for branch A of the Y-shape mandrel with constant placement angle in Section 6.4.1. As shown in Figure 6.9, the orientation of the serial robot's end-effector α, which is the selected placement angle ψ, is always kept the same as the desired path. As shown in Figure 6.10, planar curve can be decomposed to translation movement for the end effector of parallel robot with orientation β and line for serial robot with orientation ω, where β and ω can be either constant or variable angle based on the manufacturing case and satisfy the equation $\alpha = \beta + \omega$.

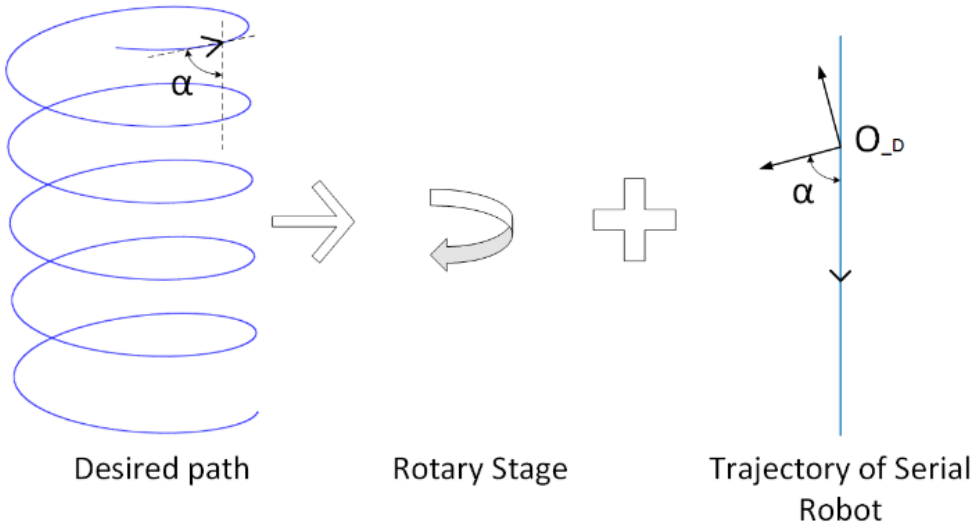

Figure 6.9. The Decomposition of Spiral Curve

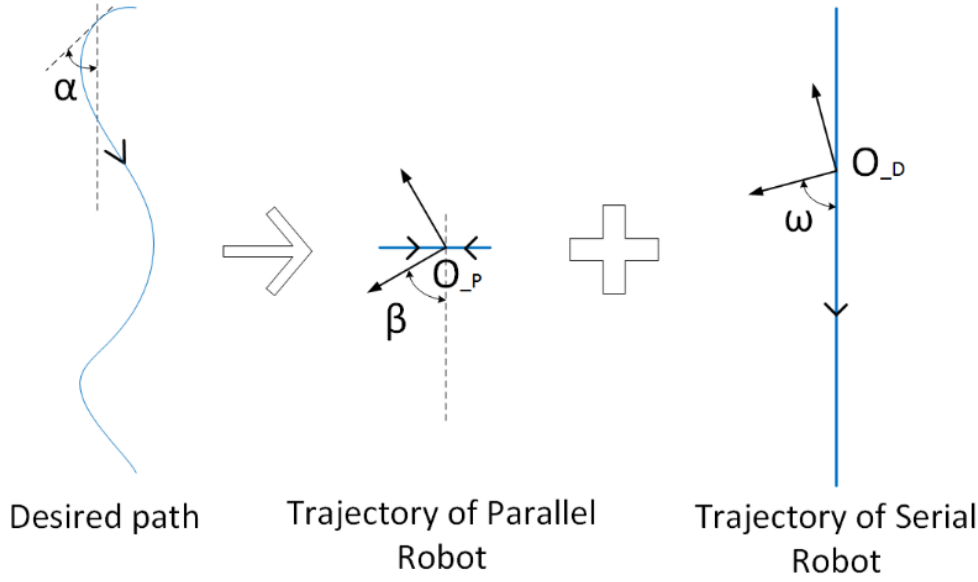

Figure 6.10. The Decomposition of Planar Curve

For general situation, in order to simplifying the decomposition process, the parallel robot is kept stationary normally. The parallel robot is only controlled to offset the gap between the desired path and the actual path to improve the accuracy and to compensate the pose limitation of serial robot when it encounter unreachable points for decomposition purpose.

Take the planar surface of the bowl shaped mandrel as example, the roller mounted on the end effector of the serial robot must be always normal to the mold surface. It is necessary to calculate

the position and orientation of the roller at any moment during fiber placement process. The decomposing process of this case is that: the parallel robot holds still; the trajectory for the end effector of the serial robot is parallel lines and the orientation of the roller on the serial robot is along y direction; rotary stage rotates the mold with required angle to change the orientation of tow for different layers.

The decomposing process for the curved surface of the bowl shaped mandrel is that: the roller moves to one point with the orientation shown in Figure 6.3 and maintains still while the rotary stage rotates one circle. Then, the roller offsets to the next point along vector $\boldsymbol{e}_3$ with the total width tow-width and repeats the operation until the producing process completes.

Figure 6.11 illustrates the decomposing process of continuously wrapping two branches of the Y-shape mandrel with constant placement angle, as shown in Section 6.4.1. It can be decomposed to the trajectory of serial robot and rotary movement of rotary stage. $\boldsymbol{e}_2$ is the normal unit vector which guarantees the roller would always be normal to the mold surface. As mentioned above, after finishing wrapping from branch A to branch B, another layer is wrapped from branch B to branch C. Then, a new layer is started from branch A to branch C and keep the wrapping cycle like this.

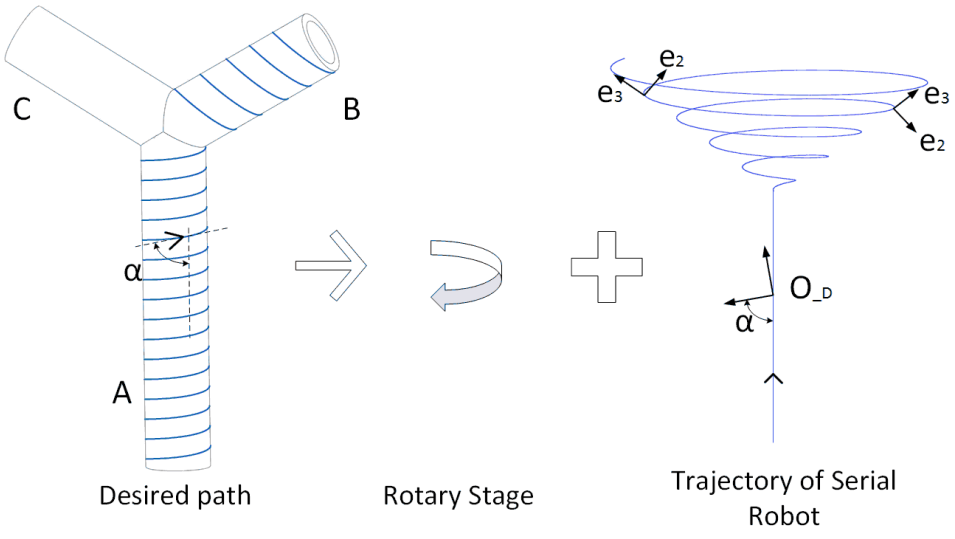

Figure 6.11. The Decomposition for Y-Shape Trajectory

However, the trajectory generated off-line for the cooperative AFP system inevitably consists of singular points and constraints in some cases. To be able to use these off-line trajectories, an

avoidance algorithm is needed. Thus, a semi-offline trajectory synchronized algorithm is proposed to meet this challenge.

6.5 Offset Generation

The semi-offline trajectory synchronized algorithm requires not only the triggering signal which indicates the moment when the offset should be added to move the parallel robot but also how much offset should be used. The poses of the end-effectors on the parallel robot and the serial robot are measured by C-track. The "offset generator" block produces the offset $\Delta \boldsymbol{p}_{\boldsymbol{p}}^{\boldsymbol{o}}$ based on different singularities, constraints and poses of the current end-effectors. The process of the offset generation is shown in Figure 6.12.

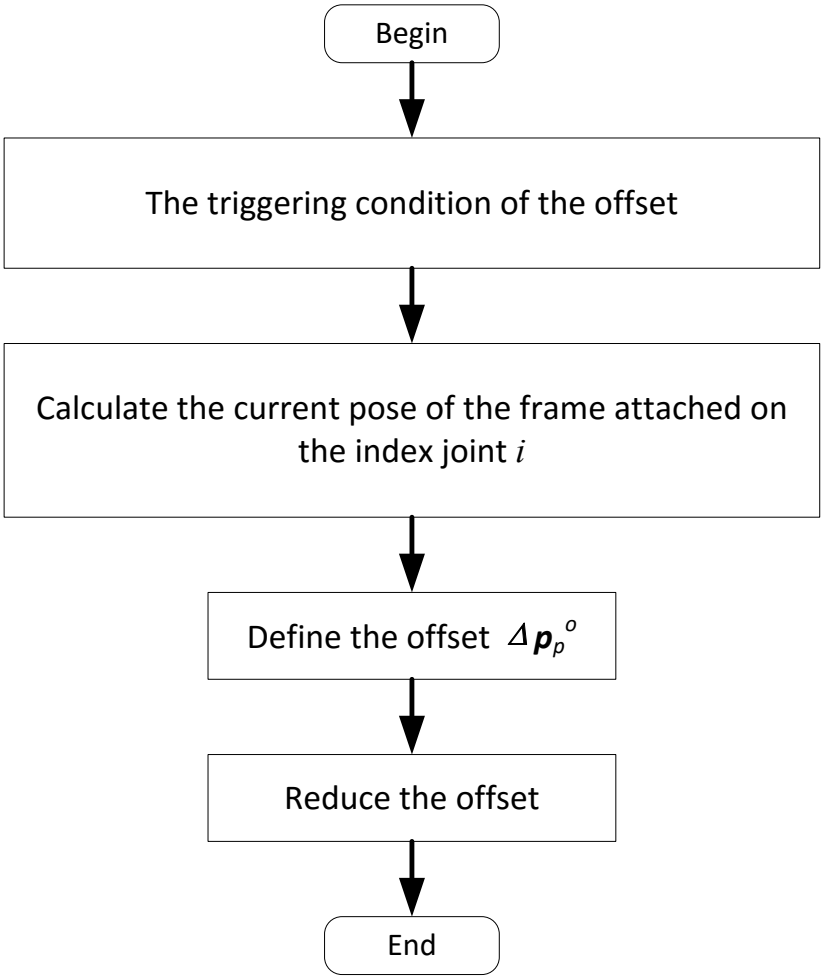

Figure 6.12. Process of the Offset Generation

6.5.1 Singularity Avoidance

Fanuc provides singularity avoidance function [159], however, it only supports linear motion and cannot be used for circular motion. Moreover, constant path and velocity may not be maintained around the singularity when the singularity is encountered. The method proposed in this dissertation can generate an optimized offset to bypass the singularities by correcting the pre-planned path without changing the kinematic relationship between the manipulator and the parallel robot. Based on the current pose of the frame attached on the index joint, the offset is generated for the parallel robot to fulfill the purpose with the minimum movement. In other words, the optimized offset for the parallel robot varies depending on the current poses of the serial robot, which guarantees that the most effective movement for the parallel robot can be generated to avoid the constraint or singular points. It can only be satisfied by using the 6-DOF robot.

As mentioned in Section 4.4.2, there are three types of singularities for the serial robot. The comprehensive processes of avoiding those singular points are presented below.

I. The Process of Wrist Singularity Avoidance

The wrist singularity happens when the axes of joint 4 and joint 6 are aligned, and might occur inside the entire reachable workspace. The triggering condition of this type of singularity is when the angle of the joint 5 is close to zero, namely $\theta_5 \approx 0°$. The process of defining the offset $\Delta \boldsymbol{p}_{\boldsymbol{p}}^{\boldsymbol{o}}$ for wrist singularity is demonstrated as following,

The rotational angle of joint 5 from the encoders of the serial robot satisfies

$$|\theta_5(k)| \leq \Delta\theta_{5min} \tag{6-13}$$

where $\Delta\theta_{5min}$ is the threshold of the joint 5 close to 0°, then the triggering signal of singularity is generated.

The offset $\Delta \boldsymbol{p}_{\boldsymbol{p}}^{\boldsymbol{o}}$ for this type of singularity is to rotate the parallel robot about the axis of the 5^{th} joint. The homogenous transformation matrix of the current pose of the serial robot ${}_{s}^{b}\boldsymbol{T}$, which can be detected from photogrammetry sensor, is given by,

$${}_{s}^{b}\boldsymbol{T} = {}_{5}^{0}\boldsymbol{T}\,{}_{6}^{5}\boldsymbol{T}\,{}_{s}^{6}\boldsymbol{T} \tag{6-14}$$

where ${}_{j}^{i}\boldsymbol{T}$ denotes the homogeneous transformation associated with the frames that are attached to the joint j and i. ${}_{s}^{6}\boldsymbol{T}$ represents the homogeneous transformation between the tool frame of serial robot and the frame attached on joint 6, which is a constant matrix. According to the kinematic of serial robot,

$$ {}_{6}^{5}\boldsymbol{T} = \begin{bmatrix} c\theta_6 & -s\theta_6 & 0 & 0 \\ 0 & 0 & 1 & 0 \\ -s\theta_6 & -c\theta_6 & 0 & 0 \\ 0 & 0 & 0 & 1 \end{bmatrix} \quad (6\text{-}15) $$

where $\mathrm{c}\theta_6 = \cos(\theta_6)$ and $\mathrm{s}\theta_6 = \sin(\theta_6)$, θ_6 can be obtained from the encoder of the sixth joint. Thus, the homogenous transformation matrix of the tool frame of the serial robot with respect to the frame attached on the joint 5 at time $t = k$ is obtained as,

$$ {}_{s}^{5}\boldsymbol{T} = {}_{6}^{5}\boldsymbol{T}\,{}_{s}^{6}\boldsymbol{T} = \begin{bmatrix} \boldsymbol{R}_6^5(\theta_6(k))\boldsymbol{R}_s^6 & \boldsymbol{R}_6^5(\theta_6(k))\boldsymbol{P}_s^6 \\ 0 & 1 \end{bmatrix} \quad (6\text{-}16) $$

where, $\boldsymbol{R}_6^5(\theta_6)$ is the orientation matrix of ${}_{6}^{5}\boldsymbol{T}$ shown in Eq.(6-15), $\boldsymbol{R}_s^6$ and $\boldsymbol{P}_s^6$ are the orientation and translation matrix of ${}_{s}^{6}\boldsymbol{T}$ respectively. Additionally, the homogenous transformation matrix of the fifth joint frame attached on the joint 5 with respect to the tool frame of parallel robot ${}_{5}^{p}\boldsymbol{T}$ is given by,

$$ {}_{5}^{p}\boldsymbol{T} = {}_{b}^{p}\boldsymbol{T}\,{}_{5}^{0}\boldsymbol{T} \quad (6\text{-}17) $$

Combining Eq. (6-14) and Eq. (6-16),

$$ {}_{5}^{p}\boldsymbol{T} = \left({}_{p}^{b}\boldsymbol{T}\right)^{-1}{}_{s}^{b}\boldsymbol{T}\left({}_{s}^{5}\boldsymbol{T}\right)^{-1} \quad (6\text{-}18) $$

Unfolding Eq. (6-18),

$$ {}_{5}^{p}\boldsymbol{T} = \begin{bmatrix} \boldsymbol{R}_p^c(k)^T & -\boldsymbol{R}_p^c(k)^T\boldsymbol{P}_p^c(k) \\ 0 & 1 \end{bmatrix}\begin{bmatrix} \boldsymbol{R}_s^c(k) & \boldsymbol{P}_s^c(k) \\ 0 & 1 \end{bmatrix}\begin{bmatrix} \boldsymbol{R}_s^{6^T}\boldsymbol{R}_6^5\left(\theta_6(k)\right)^T & -\boldsymbol{R}_s^{6^T}\boldsymbol{P}_s^6 \\ 0 & 1 \end{bmatrix} $$

$$ = \begin{bmatrix} \boldsymbol{R}_p^c(k)^T\boldsymbol{R}_s^c(k)\boldsymbol{R}_s^{6^T}\boldsymbol{R}_6^5\left(\theta_6(k)\right)^T & -\boldsymbol{R}_p^c(k)^T\boldsymbol{R}_s^c(k)\boldsymbol{R}_s^{6^T}\boldsymbol{P}_s^6 + \boldsymbol{R}_p^c(k)^T\boldsymbol{P}_s^c(k) - \boldsymbol{R}_p^c(k)^T\boldsymbol{P}_p^c(k) \\ 0 & 1 \end{bmatrix} \quad (6\text{-}19) $$

where ${}_{p}^{b}\boldsymbol{T} = \begin{bmatrix} \boldsymbol{R}_p^c(k) & \boldsymbol{P}_p^c(k) \\ 0 & 1 \end{bmatrix}$ denotes the homogenous transformation matrix of the current pose of the parallel robot $\boldsymbol{p}_p^c$ relative to the base frame F_b, ${}_{s}^{b}\boldsymbol{T} = \begin{bmatrix} \boldsymbol{R}_s^c(k) & \boldsymbol{P}_s^c(k) \\ 0 & 1 \end{bmatrix}$ denotes the homogenous transformation matrix of the current pose of the serial robot $\boldsymbol{p}_s^c$ relative to the base frame F_b.

The direction indicator $d(\theta_5)$ is given by,

$$d(\theta_5) = \theta_5(k) - \theta_5(k-1) \tag{6-20}$$

where $\theta_5(k)$ is the current angle, $\theta_5(k-1)$ is the former step angle. $d(\theta_5) > 0$ means the serial robot is reaching to the wrist singularity from the negative direction of the joint 5; $d(\theta_5) < 0$ means the serial robot is reaching to the wrist singularity from the positive direction of the joint 5. The full offset $\Delta\boldsymbol{p'}_{\boldsymbol{p}}^{\boldsymbol{o}}$ is defined as,

$$\Delta\boldsymbol{p'}_{\boldsymbol{p}}^{\boldsymbol{o}} = {}_{5}^{p}\boldsymbol{T}\begin{bmatrix} \boldsymbol{R}(z,\Delta) & 0 \\ 0 & 1 \end{bmatrix}\left({}_{5}^{p}\boldsymbol{T}\right)^{-1} \tag{6-21}$$

where $\boldsymbol{R}(z,\Delta)$ denotes the orientation matrix of the frame attached on the joint 5 about z axis by Δ. The offset for wrist singularity contains the orientation matrix of $\Delta\boldsymbol{p'}_{\boldsymbol{p}}^{\boldsymbol{o}}$, thus, one has

$$\Delta\boldsymbol{p}_{\boldsymbol{p}}^{\boldsymbol{o}} = \begin{bmatrix} \boldsymbol{R}_p^c(k)^T\boldsymbol{R}_s^c(k)\boldsymbol{R}_s^{6^T}\boldsymbol{R}_6^5\big(\theta_6(k)\big)^T\boldsymbol{R}(z,\Delta)\boldsymbol{R}_6^5\big(\theta_6(k)\big)\boldsymbol{R}_s^6\boldsymbol{R}_s^c(k)^T\boldsymbol{R}_p^c(k) & 0 \\ 0 & 1 \end{bmatrix} \tag{6-22}$$

where Δ is defined as

$$\begin{cases} \Delta = -\Delta\theta_5 & d(\theta_5) > 0 \\ \Delta = \Delta\theta_5 & d(\theta_5) < 0 \end{cases} \tag{6-23}$$

and $\Delta\theta_5$ is the desired offset of the θ_5, $\Delta\boldsymbol{p}_{\boldsymbol{p}}^{\boldsymbol{o}}$ represents the orientation movement of parallel robot about the z axis of the frame attached on joint 5.

When the rotation angle from the encoders of joint 5 satisfies

$$|\theta_5(k)| > \Delta\theta_{5min} \tag{6-24}$$

the wrist singularity triggering signal is removed and the parallel robot is moved to the initial pose where the offset starts. The process of avoiding wrist singularity is finished.

II. The Process of Elbow Singularity Avoidance

The elbow singularity, occurs when the wrist center lies in the same plane as axes of joint 2 and joint 3, could be avoided by keeping the end-effector at a safe distance from its limits. The singularity index also can be used to avoid the elbow singularity. In other words, the reachable workspace can be expanded by using elbow singularity avoidance. The index of this type of singularity is when the angle of joint 3 is close to 90°. The triggering condition of the elbow singularity is given as,

$$|\theta_3(k) - 90°| \leq \Delta\theta_{3min} \tag{6-25}$$

where $\Delta\theta_{3min}$ is the threshold of the joint 3 closed to 0°.

Different from the wrist singularity avoidance, the offset of parallel robot $\Delta \boldsymbol{p}_{\boldsymbol{p}}^{\boldsymbol{o}}$ is defined as translational movement instead of orientation movement. According to the kinematic of serial robot, ${}_{6}^{3}\boldsymbol{T}$, the homogeneous transformation associated with frames that are attached to joint 6 and 3, is given by.

$$ {}_{6}^{3}\boldsymbol{T} = \begin{bmatrix} c\theta_4 c\theta_5 c\theta_6 - s\theta_4 s\theta_6 & -c\theta_4 c\theta_5 s\theta_6 - s\theta_4 c\theta_6 & -c\theta_4 s\theta_5 & a_3 \\ s\theta_5 c\theta_6 & -s\theta_5 s\theta_6 & c\theta_5 & d_4 \\ -s\theta_4 c\theta_5 c\theta_6 - c\theta_4 s\theta_6 & s\theta_4 c\theta_5 s\theta_6 - c\theta_4 c\theta_6 & s\theta_4 s\theta_5 & 0 \\ 0 & 0 & 0 & 1 \end{bmatrix} \tag{6-26}$$

where $c\theta = \cos(\theta)$ and $s\theta = \sin(\theta)$, $a_3 = 250\ mm$, $d_4 = 835\ mm$ according to the mechanical structure of the Fanuc M20-iA. θ_4, θ_5, θ_6 can be obtained from the encoders. ${}_{6}^{3}\boldsymbol{T}$ is simplified as $\begin{bmatrix} \boldsymbol{R}_6^3(k)^T & \boldsymbol{P}_6^3 \\ 0 & 1 \end{bmatrix}$ at time $t = k$. The homogenous transformation matrix of the frame attached on joint 3 with respect to the tool frame of parallel robot ${}_{3}^{p}\boldsymbol{T}$ is given by,

$$ {}_{3}^{p}\boldsymbol{T} = \left({}_{p}^{b}\boldsymbol{T}\right)^{-1} {}_{s}^{b}\boldsymbol{T} \left({}_{6}^{3}\boldsymbol{T}\, {}_{s}^{6}\boldsymbol{T}\right)^{-1} \tag{6-27}$$

Unfolding Eq. (6-27),

$$
{}^{p}_{3}\boldsymbol{T} = \begin{bmatrix} \boldsymbol{R}_p^c(k)^T & -\boldsymbol{R}_p^c(k)^T\boldsymbol{P}_p^c(k) \\ 0 & 1 \end{bmatrix}\begin{bmatrix} \boldsymbol{R}_s^c(k) & \boldsymbol{P}_s^c(k) \\ 0 & 1 \end{bmatrix}\begin{bmatrix} \boldsymbol{R}_s^{6^T}\boldsymbol{R}_6^3(k)^T & -\boldsymbol{R}_s^{6^T}\boldsymbol{P}_s^6 - \boldsymbol{R}_s^{6^T}\boldsymbol{R}_6^3(k)^T\boldsymbol{P}_6^3 \\ 0 & 1 \end{bmatrix}
$$

$$
= \begin{bmatrix} \boldsymbol{R}_p^c(k)^T\boldsymbol{R}_s^c(k)\boldsymbol{R}_s^{6^T}\boldsymbol{R}_6^3(k)^T & \boldsymbol{R}_p^c(k)^T\boldsymbol{P}_s^c(k) - \boldsymbol{R}_p^c(k)^T\boldsymbol{P}_p^c(k) - \boldsymbol{R}_p^c(k)^T\boldsymbol{R}_s^c(k)\boldsymbol{R}_s^{6^T}(\boldsymbol{P}_s^6 + \boldsymbol{R}_6^3(k)^T\boldsymbol{P}_6^3) \\ 0 & 1 \end{bmatrix}
$$

(6-28)

The offset of the parallel robot $\Delta\boldsymbol{p}_{\boldsymbol{p}}^{\boldsymbol{o}}$ is defined as the following,

$$
\Delta\boldsymbol{p}_{\boldsymbol{p}}^{\boldsymbol{o}} = {}^{p}_{3}\boldsymbol{T}\begin{bmatrix} \boldsymbol{I} & \boldsymbol{P}(y, -\Delta d_3) \\ 0 & 1 \end{bmatrix}\left({}^{p}_{3}\boldsymbol{T}\right)^{-1} \qquad \text{(6-29)}
$$

Thus,

$$
\Delta\boldsymbol{p}_{\boldsymbol{p}}^{\boldsymbol{o}} = \begin{bmatrix} \boldsymbol{I} & \boldsymbol{R}_p^c(k)^T\boldsymbol{R}_s^c(k)\boldsymbol{R}_s^{6^T}\boldsymbol{R}_6^3(k)^T\boldsymbol{P}(y, -\Delta d_3) \\ 0 & 1 \end{bmatrix} \qquad \text{(6-30)}
$$

where $\boldsymbol{P}(y, -\Delta d_3) = [0 \quad -\Delta d_3 \quad 0]^T$ denotes the offset distance Δd_3 along the negative y axis of the frame attached on joint 3. $\Delta\boldsymbol{p}_{\boldsymbol{p}}^{\boldsymbol{o}}$ represents the translation movement along the y direction of the frame attached on joint 3 by $-\Delta d_3$, which not only avoids the workspace constraints but also extends the reachable workspace of serial robot.

When the angle from the encoders of joint 3 satisfies

$$
|\theta_3(k) - 90°| > \Delta\theta_{3min} \qquad \text{(6-31)}
$$

, then the elbow singularity triggering signal is removed and the parallel robot is moved to the initial pose when the offset starts. The process of avoiding the elbow singularity is finished.

III. The Process of Shoulder Singularity Avoidance

The shoulder singularity of Fanuc M20-iA occurs when the wrist center lies on the axis of joint 1. This type of singularity does not apply to this application due to the constant distance between the bases of serial robot and parallel robot unless the mandrel mounted on the parallel robot is big enough to cross the axis of joint 1 in some positions. However, it can be easily removed by restricting the workspace of the serial robot. Thus, like the elbow singularity avoidance, the shoulder singularity avoidance represents one kind of workspace constraints avoidance as well.

If the origin of the frame attached on the 6^{th} joint locates at the wrist center point, the index of this type of singularity is when $x_6 = 0$ and $y_6 = 0$, where x_6 and y_6 denotes the position variables of the frame attached on the joint 6 with respect to the frame attached on the joint 1 of serial robot. The triggering condition of the shoulder singularity is given as,

$$\begin{cases} |x_6| \leq \Delta d_{min} \\ |y_6| \leq \Delta d_{min} \end{cases} \quad (6\text{-}32)$$

where Δd_{min} represents the threshold of minimum distance between the sixth frame attached on the joint 6 and the first frame attached on the joint 1 along x and y direction of the first frame, which are close to 0°.

The homogenous transformation matrix of the current pose of the sixth frame with respect to the first frame ${}^{1}_{6}\boldsymbol{T}$, when the base frame is defined as the same as the first frame, can be given by,

$${}^{1}_{6}\boldsymbol{T} = {}^{b}_{6}\boldsymbol{T} = {}^{b}_{s}\boldsymbol{T}({}^{6}_{s}\boldsymbol{T})^{-1} \quad (6\text{-}33)$$

where ${}^{b}_{s}\boldsymbol{T}$ can be detected from the photogrammetry sensor, ${}^{6}_{s}\boldsymbol{T}$ is a known constant matrix. The position variables of ${}^{1}_{6}\boldsymbol{T}$ is denoted as $\boldsymbol{P}^{1}_{6}(x, \Delta d)$. The offset of the parallel robot $\Delta \boldsymbol{p}^{\boldsymbol{o}}_{\boldsymbol{p}}$ is defined as,

$$\Delta \boldsymbol{p}^{\boldsymbol{o}}_{\boldsymbol{p}} = \begin{bmatrix} \boldsymbol{I} & \boldsymbol{P}(x, \Delta d) \\ 0 & 1 \end{bmatrix} \quad (6\text{-}34)$$

$\Delta \boldsymbol{p}^{\boldsymbol{o}}_{\boldsymbol{p}}$ represents the translation movement of parallel robot along x direction of the base frame by the positive distance Δd.

when

$$\begin{cases} |x_6| > \Delta d_{min} \\ |y_6| > \Delta d_{min} \end{cases} \quad (6\text{-}35)$$

the shoulder singularity index is removed and the parallel robot is moved to the initial pose. The process of avoiding the shoulder singularity is finished.

6.5.2 Joints Constraints Avoidance

According to Table 4-1, each joint is subject to its limits. The following process demonstrates the joint constraints avoidance for joint i.

First, joint i from the encoders of the serial robot is monitored. When they satisfy

$$\begin{cases} |\theta_i(k) - \theta_{imax}| \le \Delta\theta_{imin} \\ |\theta_i(k) - \theta_{imin}| \le \Delta\theta_{imin} \end{cases} \quad (6\text{-}36)$$

where $\Delta\theta_{imin}$ is the threshold of joint i closed to 0°, the index of joint i constraint is generated.

The offset $\Delta\boldsymbol{p}_{\boldsymbol{p}}^{\boldsymbol{o}}$ for the joint i constraint is defined as,

$$\Delta\boldsymbol{p}_{\boldsymbol{p}}^{\boldsymbol{o}} = \begin{bmatrix} \boldsymbol{R}_p^c(k)^T \boldsymbol{R}_s^c(k) \boldsymbol{R}_s^{6^T} \boldsymbol{R}_6^i(k)^T \boldsymbol{R}(z, \Delta\theta_i) \boldsymbol{R}_6^i(k) \boldsymbol{R}_s^6 \boldsymbol{R}_s^c(k)^T \boldsymbol{R}_p^c(k) & 0 \\ 0 & 1 \end{bmatrix} \quad (6\text{-}37)$$

where $\boldsymbol{R}(z, \Delta\theta_i)$ denotes the orientation matrix of the frame attached on the joint i about z axis by $\Delta\theta_i$. The direction is given as,

$$\begin{cases} \Delta\theta_i > 0, & |\theta_i(k) - \theta_{imin}| \le \Delta\theta_{imin} \\ \Delta\theta_i < 0, & |\theta_i(k) - \theta_{imax}| \le \Delta\theta_{imin} \end{cases} \quad (6\text{-}38)$$

The encoders of joint i is monitored. When the measured angles $\theta_i(k)$ satisfy

$$\begin{cases} |\theta_i(k) - \theta_{imax}| > \Delta\theta_{imin} \\ |\theta_i(k) - \theta_{imin}| > \Delta\theta_{imin} \end{cases} \quad (6\text{-}39)$$

, the joint i constraint triggering signal is removed and the parallel robot is moved to the initial pose. The process of avoiding joint i constraint is finished.

6.6 Compensation Pose Calculation

In most cases, coordination control of multi-robots focuses on the kinematic relationships amongst robots. The error with respect to the base frame is not priority issue for the multi-robots operation. In the application of this project, when the parallel robot is moved, the accuracy of it can be ignored because the current pose of the tool frame of the parallel robot F_t^P is fed to the controller of serial

robot directly to fulfill its purpose, i.e. avoiding singularities in the pre-planned trajectory planning. Under this circumstance, the pose error of parallel robot $\boldsymbol{e}_p(t)$ can be assumed as zero. Thus, the synchronization error $\boldsymbol{\varepsilon}(t)$ can be simplified as the compensation error of serial robot, $\boldsymbol{e}_s^c(t)$, which is given by

$$\boldsymbol{e}_s^c(t) = \boldsymbol{c}_s^d(t) - \boldsymbol{p}_s^c(t) \quad (6\text{-}40)$$

where $\boldsymbol{p}_s^c(t)$ is the current pose of the tool frame of the serial robot F_t^S with respect to the base frame F_b, which is detected by photogrammetry sensor; $\boldsymbol{c}_s^d(t)$ represents the desired compensation pose trajectory of F_t^S with reference to F_b.

$$\boldsymbol{c}_s^d(t) = \boldsymbol{p'}_s^d(t) + \Delta_s^d(t) \quad (6\text{-}41)$$

where $\boldsymbol{p'}_s^d(t)$ represents the desired offline trajectory planning pose of serial robot without compensation inputs, $\Delta_s^d(t)$ denotes the compensation pose of serial robot according to the offset inputs of parallel robot.

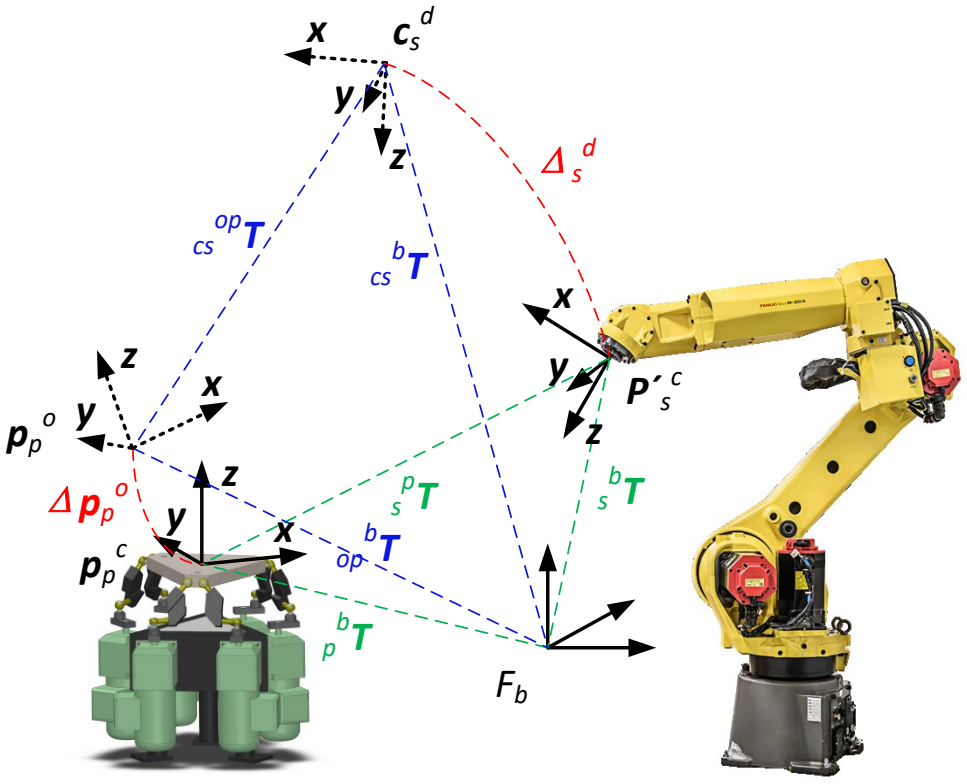

Figure 6.13. Compensation Pose Calculation

As shown in Figure 6.13, the desired compensation pose $\boldsymbol{c}_s^d(t)$ at $\mathrm{t} = k$, is composed of the three position variables $P(x_s^d(k), y_s^d(k), z_s^d(k))$ and three orientation variables $R(\alpha_s^d(k), \beta_s^d(k), \gamma_s^d(k))$. The homogenous transformation matrix of $\boldsymbol{c}_s^d(k)$ with respect to the base frame F_b is denoted as ${}^{b}_{cs}\boldsymbol{T} = \begin{bmatrix} \boldsymbol{R}_s^d(k) & \boldsymbol{P}_s^d(k) \\ 0 & 1 \end{bmatrix}$, given by

$$ {}^{b}_{cs}\boldsymbol{T} = {}^{b}_{op}\boldsymbol{T}\ {}^{op}_{cs}\boldsymbol{T} \qquad (6\text{-}42) $$

where, ${}^{b}_{op}\boldsymbol{T}$ denotes the homogenous transformation matrix of the current pose of the parallel robot with offset inputs $\boldsymbol{p}_p^o(t)$ at $\mathrm{t} = k$ relative to the base frame F_b, which is described as $\begin{bmatrix} \boldsymbol{R}_p^o(k) & \boldsymbol{P}_p^o(k) \\ 0 & 1 \end{bmatrix}$ and can be detected by the photogrammetry sensor, $\boldsymbol{R}_p^o(k)$ consists of three orientation variables $R\left(\alpha_p^o(k), \beta_p^o(k), \gamma_p^o(k)\right)$, $\boldsymbol{P}_p^o(k)$ consists of three position variables $P\left(x_p^o(k), y_p^o(k), z_p^o(k)\right)$, ${}^{op}_{cs}\boldsymbol{T}$ represents the homogenous transformation matrix from the tool frame of the serial robot F_t^S to the tool frame of the parallel robot F_t^P with offset inputs, which is $\boldsymbol{\psi}_s(k)$ in Eq. (6-6).

$$ {}^{b}_{s}\boldsymbol{T} = {}^{b}_{p}\boldsymbol{T}\ {}^{p}_{s}\boldsymbol{T} \qquad (6\text{-}43) $$

where ${}^{b}_{s}\boldsymbol{T}$ is the homogenous transformation matrix of the current pose of the serial robot $\boldsymbol{p'}_s^c$ without compensation inputs relative to the base frame F_b at $\mathrm{t} = k - 1$, which is described as $\begin{bmatrix} \boldsymbol{R}_s^c(k-1) & \boldsymbol{P}_s^c(k-1) \\ 0 & 1 \end{bmatrix}$. The six pose variables $\boldsymbol{p}(x_s^c(k-1), y_s^c(k-1), z_s^c(k-1), \alpha_s^c(k-1), \beta_s^c(k-1), \gamma_s^c(k-1))$ in ${}^{b}_{s}\boldsymbol{T}$ can be obtained as the former step pose of serial robot $\boldsymbol{p}_s^c(k-1)$ by the photogrammetry sensor. ${}^{b}_{p}\boldsymbol{T}$, described as $\begin{bmatrix} \boldsymbol{R}_p^c(k-1) & \boldsymbol{P}_p^c(k-1) \\ 0 & 1 \end{bmatrix}$, is the homogenous transformation matrix of the current pose of the parallel robot without offset inputs $\boldsymbol{p}_p^c$ relative to the base frame F_b, whose six pose variables $\boldsymbol{p}(x_p^c(k-1), y_p^c(k-1), z_p^c(k-1), \alpha_p^c(k-1), \beta_p^c(k-1), \gamma_p^c(k-1))$ is the former step pose of parallel robot $\boldsymbol{p}_p^c(k-1)$ known from the photogrammetry sensor. ${}^{p}_{s}\boldsymbol{T}$ represents the homogenous transformation matrix from the tool frame of the serial robot F_t^S to the tool frame of the parallel robot F_t^P without offset inputs, which is $\boldsymbol{\psi}_s(k-1)$.

The trajectory synchronized algorithm is to maintain the kinematic relationships between the two robots. Two cases are considered here. In the first case, the certain kinematic relationships between the end-effectors of the two robots is constant, which means ${}^{op}_{cs}\boldsymbol{T} = {}^{p}_{s}\boldsymbol{T}$. The desired compensation pose $\boldsymbol{c}_s^d(k)$ can be given by,

$$ {}^{b}_{cs}\boldsymbol{T} = {}^{b}_{op}\boldsymbol{T}\left({}^{b}_{p}\boldsymbol{T}\right)^{-1}{}^{b}_{s}\boldsymbol{T} \tag{6-44} $$

Thus, one has

$$ \begin{bmatrix} \boldsymbol{R}_s^d(t) & \boldsymbol{P}_s^d(k) \\ 0 & 1 \end{bmatrix} = \begin{bmatrix} \boldsymbol{R}_p^o(k) & \boldsymbol{P}_p^o(k) \\ 0 & 1 \end{bmatrix} \begin{bmatrix} \boldsymbol{R}_p^c(k-1)^T & -\boldsymbol{R}_p^c(k-1)^T\boldsymbol{P}_p^c(k-1) \\ 0 & 1 \end{bmatrix} \begin{bmatrix} \boldsymbol{R}_s^c(k-1) & \boldsymbol{P}_s^c(k-1) \\ 0 & 1 \end{bmatrix} \tag{6-45} $$

According to Eq. (6-45), the six desired compensation pose $\boldsymbol{c}_s^d(k)$ can be calculated by the following equations,

$$ \begin{aligned} \boldsymbol{R}_s^d(k) &= \boldsymbol{R}_p^o(k)\boldsymbol{R}_p^c(k-1)^T\boldsymbol{R}_s^c(k-1) \\ \boldsymbol{P}_s^d(k) &= \boldsymbol{R}_p^o(k)\boldsymbol{R}_p^c(k-1)^T\boldsymbol{P}_s^c(k-1) - \boldsymbol{R}_p^o(k)\boldsymbol{R}_p^c(k-1)^T\boldsymbol{P}_p^c(k-1) + \boldsymbol{P}_p^o(k) \end{aligned} \tag{6-46} $$

In the second case, $\boldsymbol{\psi}_s(k)$ is pre-planned, and the change of kinematic relationships between the two end-effector $\Delta\boldsymbol{T}$ is known. The relationship can be expressed as,

$$ {}^{op}_{cs}\boldsymbol{T} = {}^{p}_{s}\boldsymbol{T}\Delta\boldsymbol{T} \tag{6-47} $$

Eq. (6-44) can be rewritten as,

$$ {}^{b}_{cs}\boldsymbol{T} = {}^{b}_{op}\boldsymbol{T}\Delta\boldsymbol{T}\left({}^{b}_{p}\boldsymbol{T}\right)^{-1}{}^{b}_{s}\boldsymbol{T}\Delta\boldsymbol{T} \tag{6-48} $$

6.7 Summary

In this chapter, the control structure regarding a semi-offline trajectory synchronized algorithm is introduced for a cooperative AFP system consisting of a 6-DOF serial robot holding the fiber placement head, a 6-RSS parallel robot on which a one DOF mandrel holder is installed at first. Secondly, the synchronization function for the cooperative AFP system is presented to maintain the certain kinematic relationships amongst robots in Section 6.3. Thirdly, the off-line trajectory planning and the decomposition processes for the cooperative AFP system is illustrated. Two algorithms are proposed to generate the off-line trajectory for the Y-shape mandrel. Then, the procedures of the generation offsets for the parallel robot are given in Section 6.5. The offsets are calculated based on different conditions including singularity avoidance and joints constraints avoidance. The optimized offset for the parallel robot varies depending on the current poses of the serial robot, which guarantees that the most effective movement for the parallel robot can be generated to avoid the constraint or singular points. A photogrammetry sensor is adopted to detect the poses of the end-effectors on parallel robot and serial robot. Accordingly, the compensation pose calculation process is proposed in Section 6.6. Based on the measured poses of both the serial robot and the parallel robot, a pose correction algorithm is proposed to generate pose correction signal which is added to the pre-planned trajectory for avoiding singularities, optimizing joint limits, and expanding the workspace of the whole system online.

The experimental setup will be introduced and avoidance results will be demonstrated in next chapter

CHPATER 7

7 EXPERIMENT RESULTS

7.1 Introduction

The purpose of the proposed semi-offline trajectory synchronized algorithm is adding correction to adjust the pre-planned trajectory to avoid collision, singular points and expand workspace of the cooperative AFP system. Compared to the traditional trajectory planning, this method can free the off-line planned trajectory from strictly subjecting to the constraints and singularities. In other words, the generated trajectories consisting of collision and singular points can still be used for the fiber placement manufacturing.

In this chapter, the experimental setup of the cooperative AFP system is introduced at first. The cooperative AFP systems consists of one 6 RSS parallel robot, one 6 DOF serial manipulator, a fiber processing head, a spindle which is mounted on the platform and a photogrammetry sensor for the visual feedback. Then, the experimental tests demonstrate the cooperative AFP manufacturing process for Y-shape mandrel with joint limit and wrist singularity in the pre-planned trajectory. The serial robot successfully passes the joint limit and singularity points by adding the correction generated by semi-offline trajectory synchronized algorithm to the pre-planned trajectory online.

7.2 Cooperative AFP System Setup

The experimental setup of the cooperative AFP system consists of one 6 DOF serial manipulator, a fiber processing head, one 6 DOF parallel robot, a spindle which is mounted on the platform and a photogrammetry sensor, as shown in Figure 5.1.

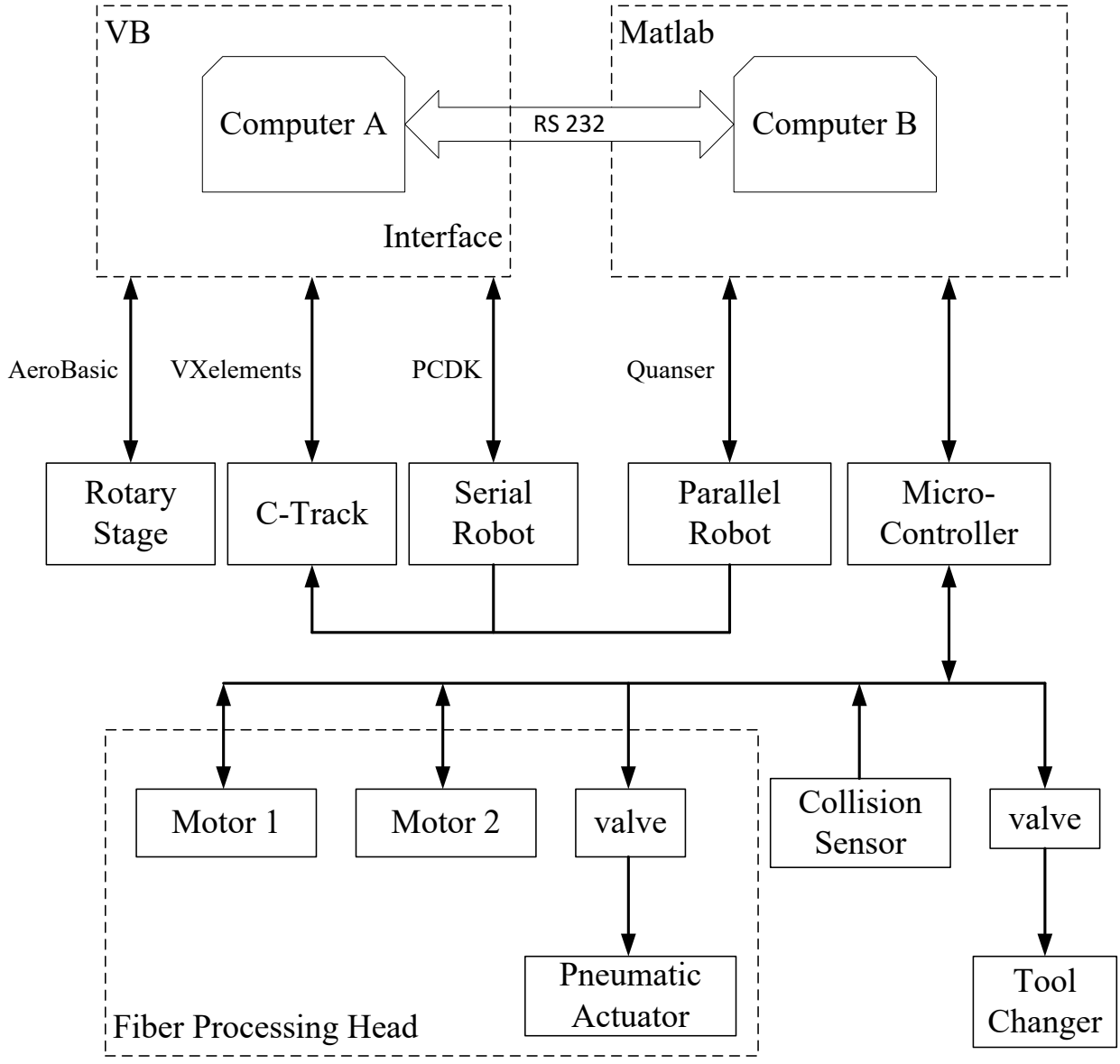

Figure 7.1. Hardware Structure

The hardware structure of the cooperative AFP system is illustrated in Figure 7.1. Two computers are used in the system. The serial communication RS232 is adopted for the communication between these two computers. There are serval reasons of using two computers instead of one computer. Firstly, implementing all controllers (including data acquisition of photogrammetry sensor, serial robot, rotary stage, parallel robot and micro-controller) on one computer would slow down the process speed and cause negative effects on real-time performance of the cooperative AFP system. Additionally, there are limitations from the hardware setup. Two Quanser data acquisition cards are used to control the parallel robot, which requires two PCI slots. It is not supported by computer-A. Moreover, the C-track license is bound to computer-A.

Control interface for computer-A is programed by Visual Basic (VB). Programing language AeroBasic provided by Aerotech Inc. is applied to control the rotary stage and receive the angle from encoder as well as other control feedback signals. In the meantime, alternative choice of control the rotary stage via API used by VB is also provided by the company. VXelements application programming interface (API) is employed by VB to control C-track to receive the detected poses of objects. The VXelements API is a collection of .NET classes to act as a programming interface between VXelements and other applications. Through the API, all of VXelements main functionalities can be controlled and the data produced by each VXelements module can be retrieved for the utilization of other applications. And PC developer's kit (PCDK) provided by Fanuc Robotics is applied for the communication of information and instructions between computer-A and the serial robot. Matlab is used as the control platform for computer-B. The 6-RSS parallel robot is controlled by computer-B via Quanser open-architecture control module. In addition, a micro-controller is integrated into the control platform of computer-B. Such micro-controller is applied to drive a 4-way solenoid valve for the tool changer, receive collision signal from the collision sensor and control the fiber processing head which consists of two servo motors and a valve for a pneumatic actuator. The control algorithm is programed on computer-A using VB. Based on poses information acquired by C-track and the value of every actuator angle received from the encoders of the serial robot via PCDK, the desired pose of the parallel robot generated by the semi-offline trajectory synchronized algorithm will be transferred to computer-B via the serial communication RS232. And computer-A will receive the feedback information regarding the values of actuator angles measured by the encoders of the parallel robot and output

signals of the micro-controller used for controlling tool changer, collision senor and the fiber processing head from computer-B.

The detail experimental setup is presented below.

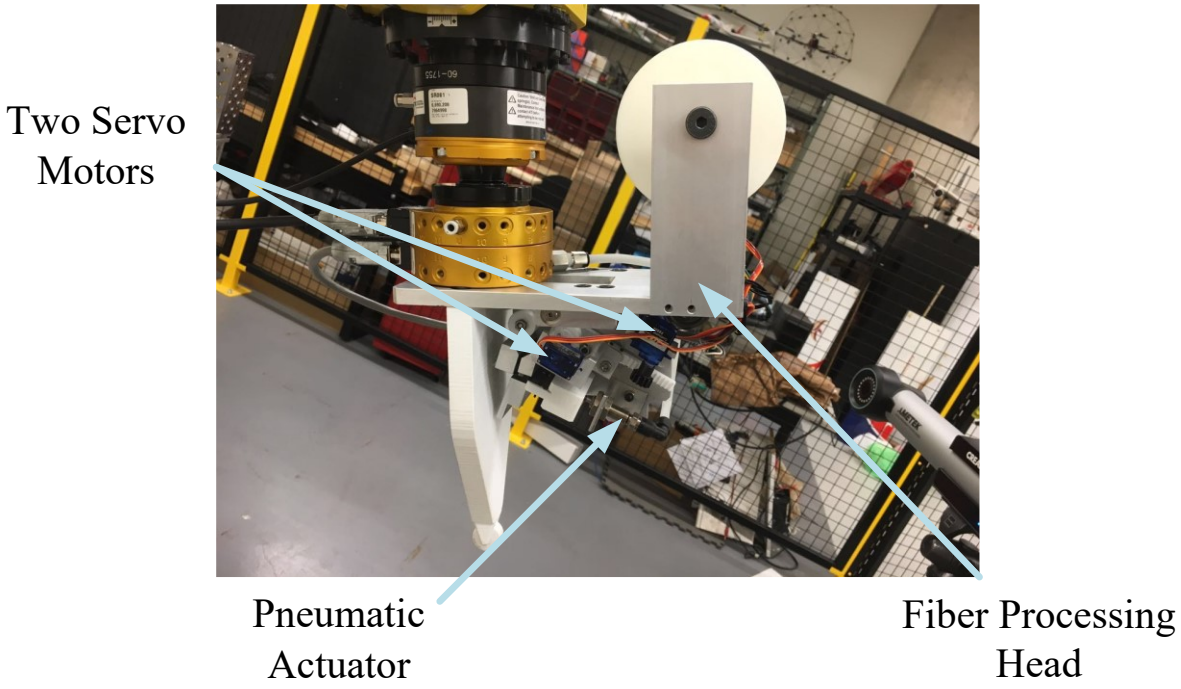

Figure 7.2. Fiber Processing Head

As mentioned before, the 6 DOF serial robot is Fanuc M20-iA along with Fanuc Robotics software, and the R-30iB controller. It's wrist-partitioned series of mechanical links driven by servomotors. The first three axes make up the major axes and the last three axes are the minor axes, which is called wrist. Its repeat accuracy is ± 0.10 mm , and the payload at wrist is 20 kg. As shown in Figure 7.2, the electrical part of fiber processing head consists of one cutter moved by a pneumatic actuator to cut fiber tows, and two servo motors. The pneumatic actuator is drove by a valve. The purpose of one servo motor is to feed the fiber tows and the other one is to adjust the distance between two rollers which can hold the fiber tows. Some mechanical components of the fiber processing head are shown in appendix D.

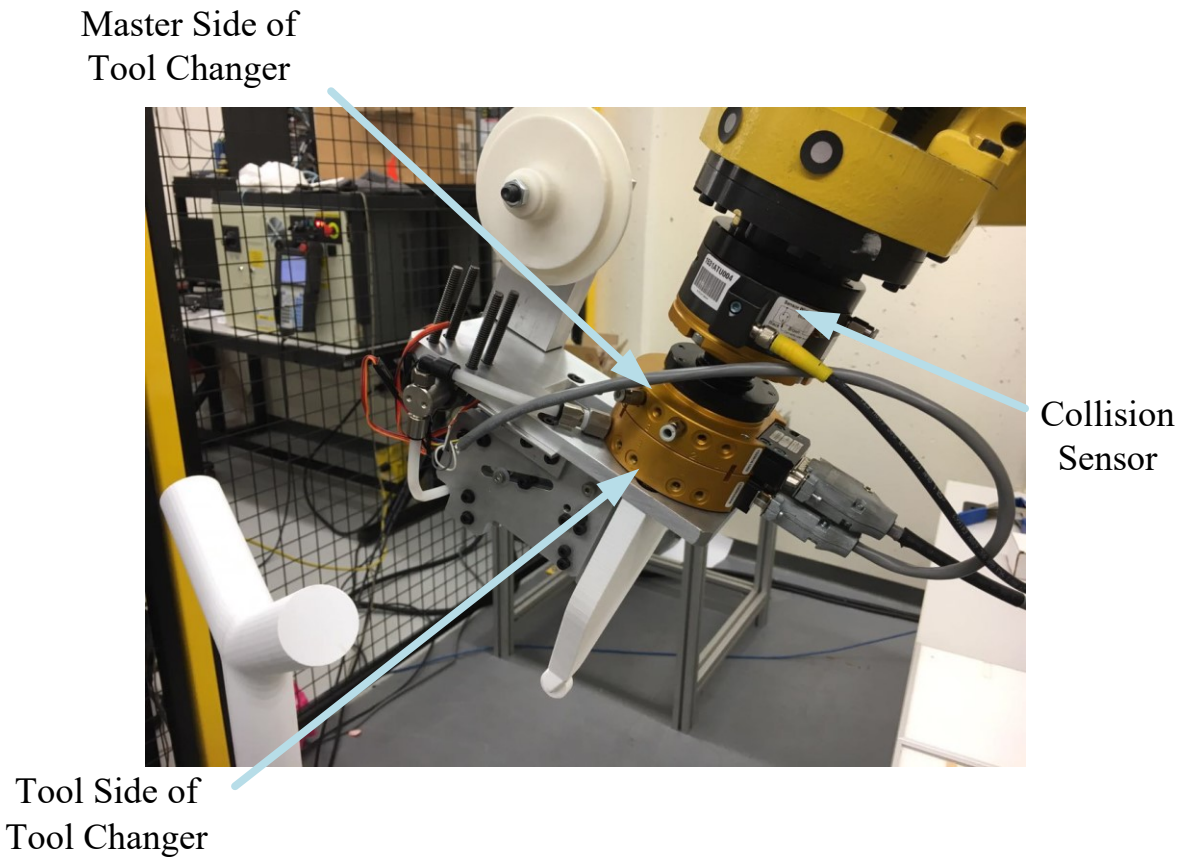

Figure 7.3. Tool Changer and Collision Sensor

The fiber processing head is attached to the tool side of a tool changer which is model QC-20 from ATI Industrial Automation. The payload of the tool changer is 55 lbs. The master side of the tool changer is attached to the collision sensor, model SR-82, provided by ATI Industrial Automation, as shown in Figure 7.3. The tool changer, controlled by a 4-ways solenoid valve, provides flexibility to robot applications by allowing the robot to change the end-effector automatically. The master plate of the tool changer locks to the tool plate with a pneumatically-driven locking mechanism. Such locking mechanism uses a multi-tapered cam with ball locking technology and a fail-safe mechanism. In operation, electrical signals, pneumatic power and fluids can be transferred to the end-effector through the master plate and the tool plate.

The collision sensor, mounted on the flange of serial manipulator, is a pneumatically pressurized device offering protection to the serial robot in the event of accidental impacts and unanticipated loads. The collision sensor works by “breaking away” from its working geometry in the event of excessive torsional, moment, or compressive axial forces, or any combination of these. The

collision sensor cannot respond to pure axial tension, which is an unlikely mode of loading. Removal of the upsetting force or moment allows the collision sensor to return to its normal working geometry. As a collision occurs, internal motion of the sensor components cause a normally-closed dry contact switch to open. The switch circuit is monitored by robotic controller to stop operations before damage to the experimental setup. The load threshold at which the collision sensor breaks away is adjustable by controlling the air pressure supplied to the sensor. Clean, dry, non-lubricated air at 25-90 psi of pressure in an environment with an ambient temperature range of 5-50 °C is required. Such air pressure is supplied and controlled by a regulator in the lab. Additionally, the amount of compliance provided by the collision sensor before the switch circuit opens is adjustable by turning a switch adjustment screw.

The solenoid valve, the collision sensor, the pneumatic actuator and the two servo motors are controlled by a micro-controller which is Arduino, as shown in Figure 7.4. The mechanical component to for installing the valve to the Fanuc is shown in appendix C.

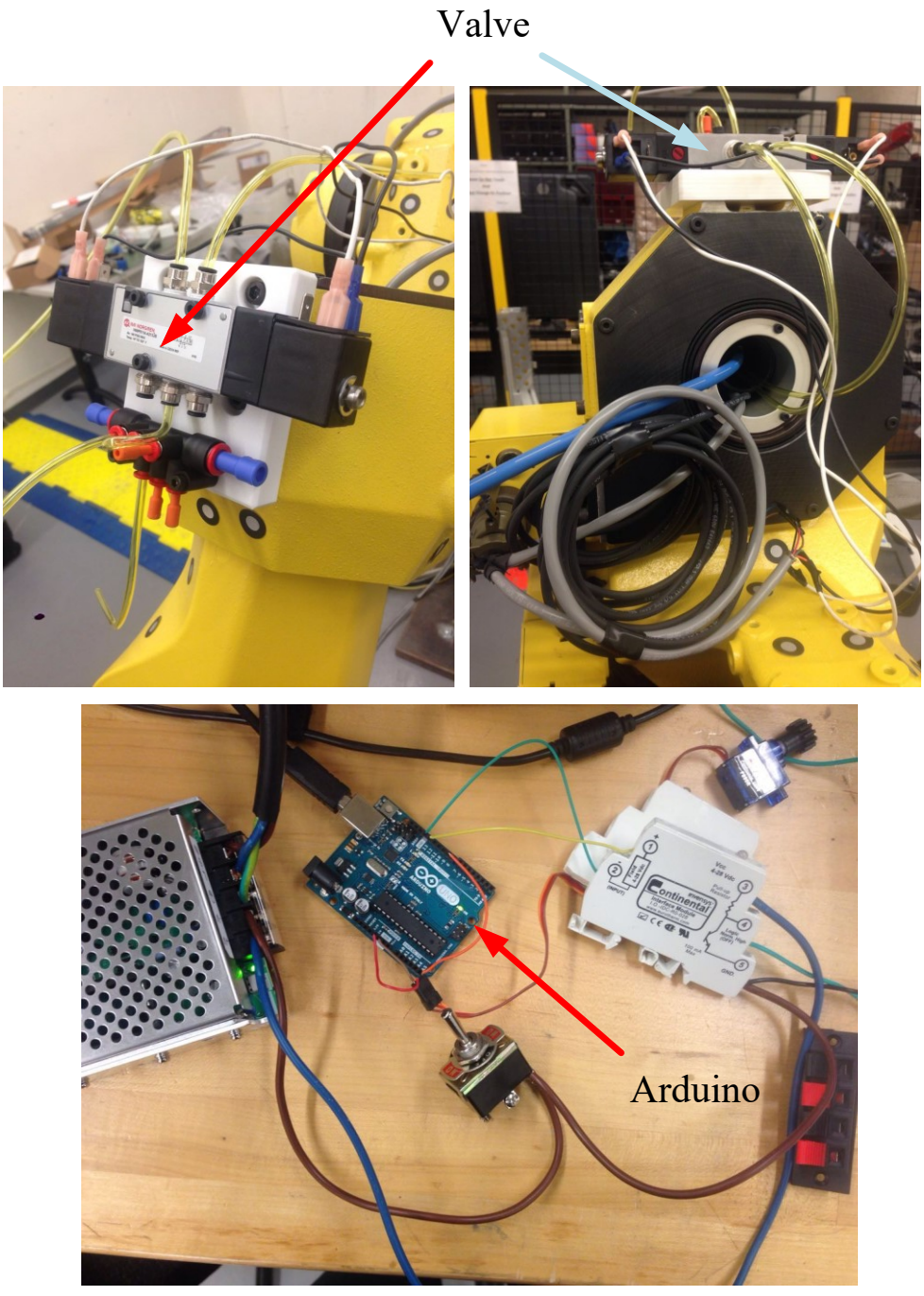

Figure 7.4. 4-ways Solenoid Valve and Arduino

The 6-RSS parallel robot used in the cooperative AFP system is Electric Motion System, model 710LP-6-500-220, provided by Servo & Simulation Inc., which contains six identical kinematic chains connecting the base and the moving platform. Each connecting chain is composed of one horizontal revolute joint mounted on the base and two spherical joints. In the identical kinematic

chain, one end of the proximal link is connected to the base by revolute joint and the other end of the proximal link is connected to the distal link by spherical joint. The other end of the distal link in the kinematic chain is connected to the upper platform by spherical joint. The motors and encoders are located at the revolute joints on the base.

The one degree-of-freedom spindle consists of one rotary stage and one three-jaw chuck, as shown in Figure 7.5. The rotary stage used in the cooperative AFP system is AGR75-NC-9DU-BMS-R-3 with soloist CP controller from Aerotech Inc., which is mounted on the upper platform of the parallel robot. The rotary stage is designed with two high-precision angular contact bearings, brushless servomotor, and direct encoder mounted to the stage shaft. The accuracy of the rotary stage with direct encoder is $20\ arc\ sec$, uni-directional repeatability is $5\ arc\ sec$, and bi-directional repeatability is $8\ arc\ sec$. The axial load capacity of the rotary stage can reach to $100\ kg$, and the radial load capacity is $50\ kg$. The maximum torque load to the stage shaft is $3.5\ N \cdot m$. The three-jaw chuck is attached to the rotary stage to hold the mandrel, as shown in Figure 7.6. The pose of the mandrel can be controlled by the parallel robot. The mechanical components to connect the upper platform of the parallel robot, the rotary stage and the three-jaw chuck are shown in appendices A, B.

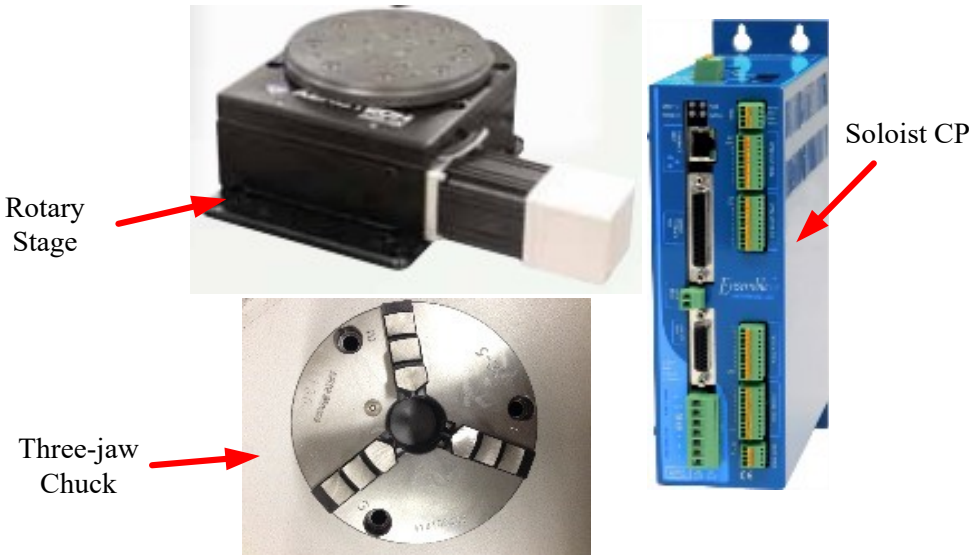

Figure 7.5. Components of Spindle

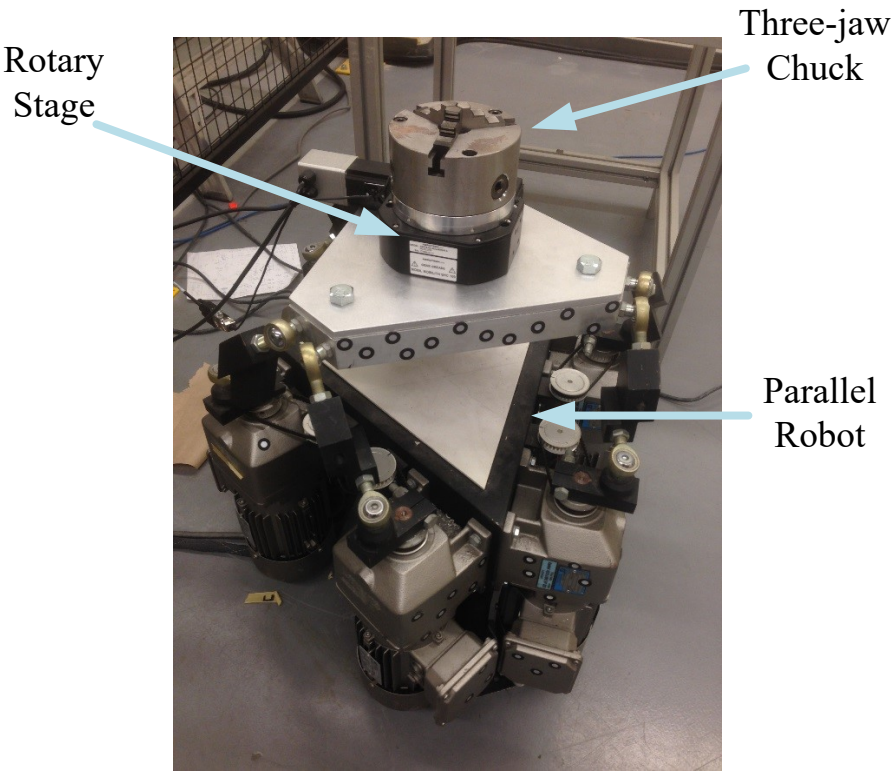

Figure 7.6. Parallel Robot with Spindle

Figure 7.7. C-Track

The photogrammetry sensor adopts a dual-camera sensor C-track 780, which can provide continuous image acquisition and transmission in real time. Handy Probe is used to detect points for visual modelling, as shown in Figure 7.7. The measurement speed is 29 Hz. The two cameras of the C-track acquire the positioning targets simultaneously, which enables the VXelementes software to determine the position as well as its environment through triangulation, shown in Figure 7.8.

Figure 7.8. Detecting Objects by Two Cameras

Matlab have been used as the control platform for computer-B. Simulink files are built under Matlab environment for the communication between two computers and the control of the parallel robot and the micro-controller.

Figure 7.9 shows the Matlab/Simulink file executed in computer-B to communicate with computer-A via serial port using COM1. “Serial Receive” block receives binary data over serial port. The data size is set as $[6 \quad 1]$, which is the six variables for the desired pose of the parallel robot. “Serial Configuration” block configures the parameters for the serial port. However, the received data from computer-A cannot import into the controller of the parallel robot directly because this Simulink file only works under “Normal mode” due to the presence of COM1 module, but Quanser open-architecture control module works under “External mode”.

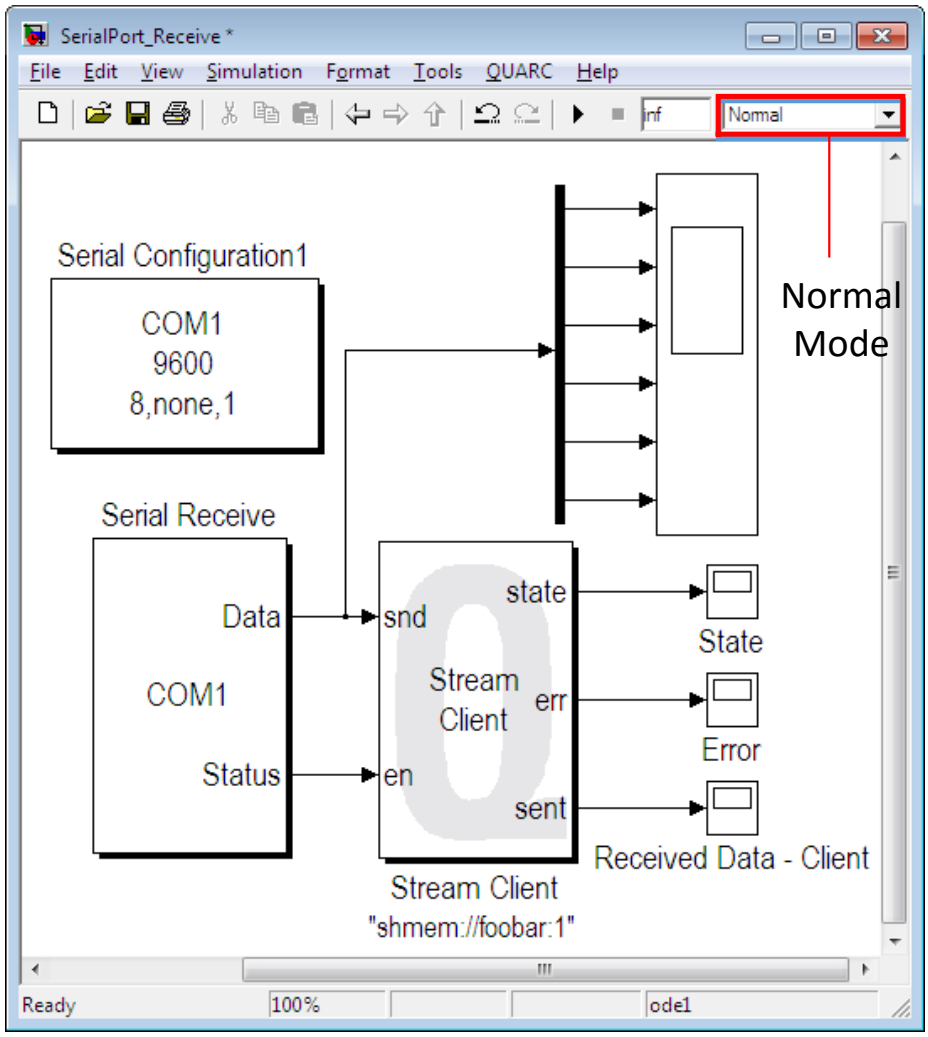

Figure 7.9. Remote Communication Diagram under Normal Mode

Another Simulink file is built in computer-*B* to control the parallel robot with the received desired pose sent by computer-*A*, as shown in Figure 7.10. Because Matlab/Simulink block diagram cannot run under two different modes at the same time, these two Simulink files need to be executed simultaneously. In order to communicate between the two Simulink files, “Stream Client” and “Stream Server” modules which can work under both normal and external mode are applied. “Stream Client” module in Figure 7.9 can connect to a remote host and sends and/or receives data from that host. “Stream Server” module in Figure 7.10 accepts the connection from “Stream Client” module in another Simulink file and sends and/or receives data from that host, which realizes the communication between two Simulink files under “Normal mode” and “External mode”.

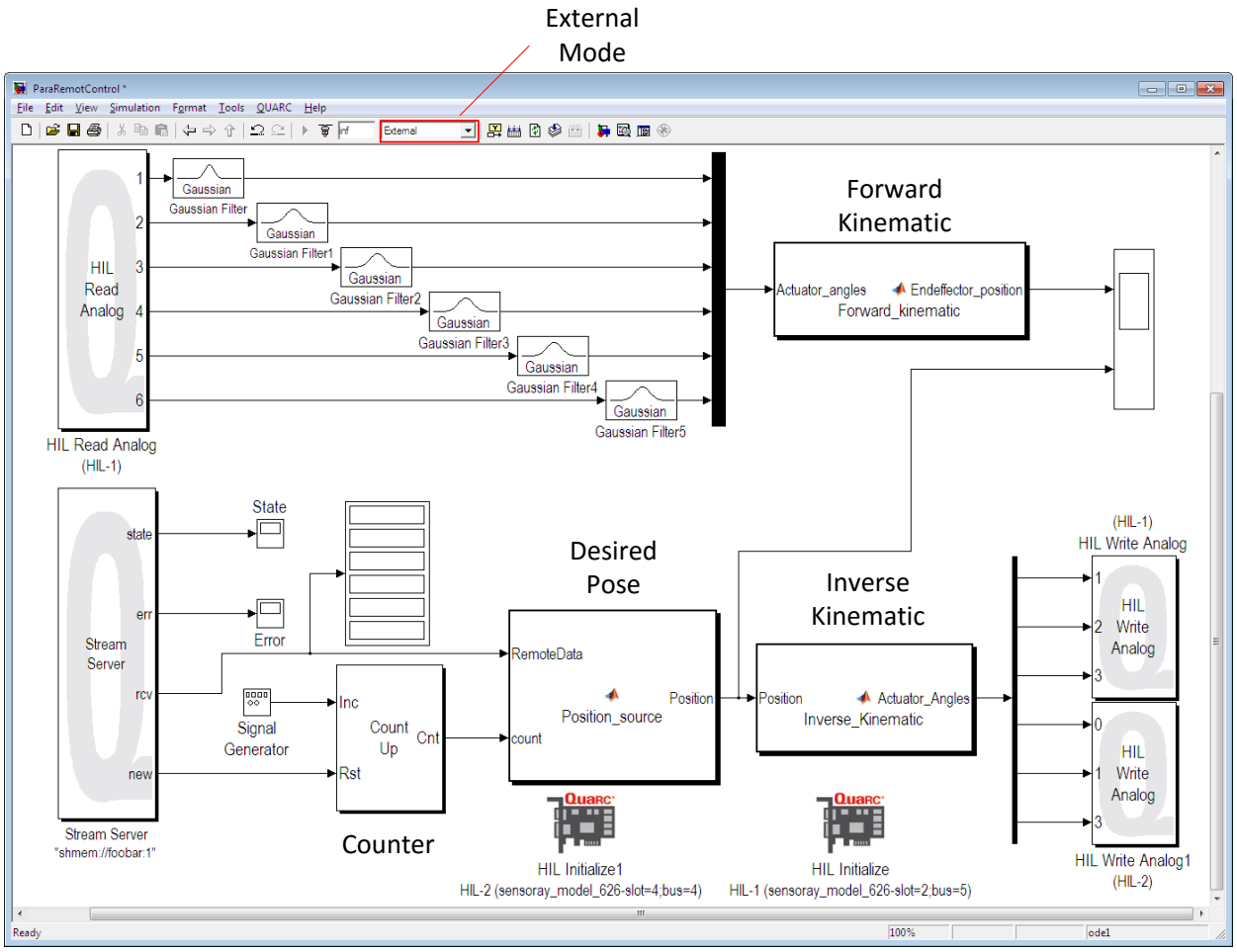

Figure 7.10. Controlling the Parallel Robot

In the bottom part of the control diagram in Figure 7.10, “Stream Server” module receives the desired pose calculated by the semi-offline trajectory synchronized algorithm from the other Simulink “Normal mode” file. “Desired Pose” block calculates the path from the initial pose to the desired pose in Cartesian coordinate frame based on the interpolation using the number generated by the “Counter” block. “Inverse Kinematic” block transfers the desired poses in Cartesian coordinate frame to six actuator signals for the motors. “HIL Write Analog” blocks write drive inputs to analog output channels of a hardware-in-the-loop card. Inputs are the analog output voltages. Each “HIL Write Analog” block can write inputs to maximum four channels. Thus, two “HIL Write Analog” blocks are used to drive 6-DOF parallel robot. In the top part of the control diagram of Figure 7.10, “HIL Read Analog” block reads analog input channels of a hardware-in-the-loop card. Outputs are the voltages read from the six analog channels. “Forward Kinematic”

block can transfer the angles of the six motors read by “HIL Read Analog” block to the pose of the parallel robot. Hence, the remote control of the parallel robot from different computer using Simulink with different modes is realized in real-time.

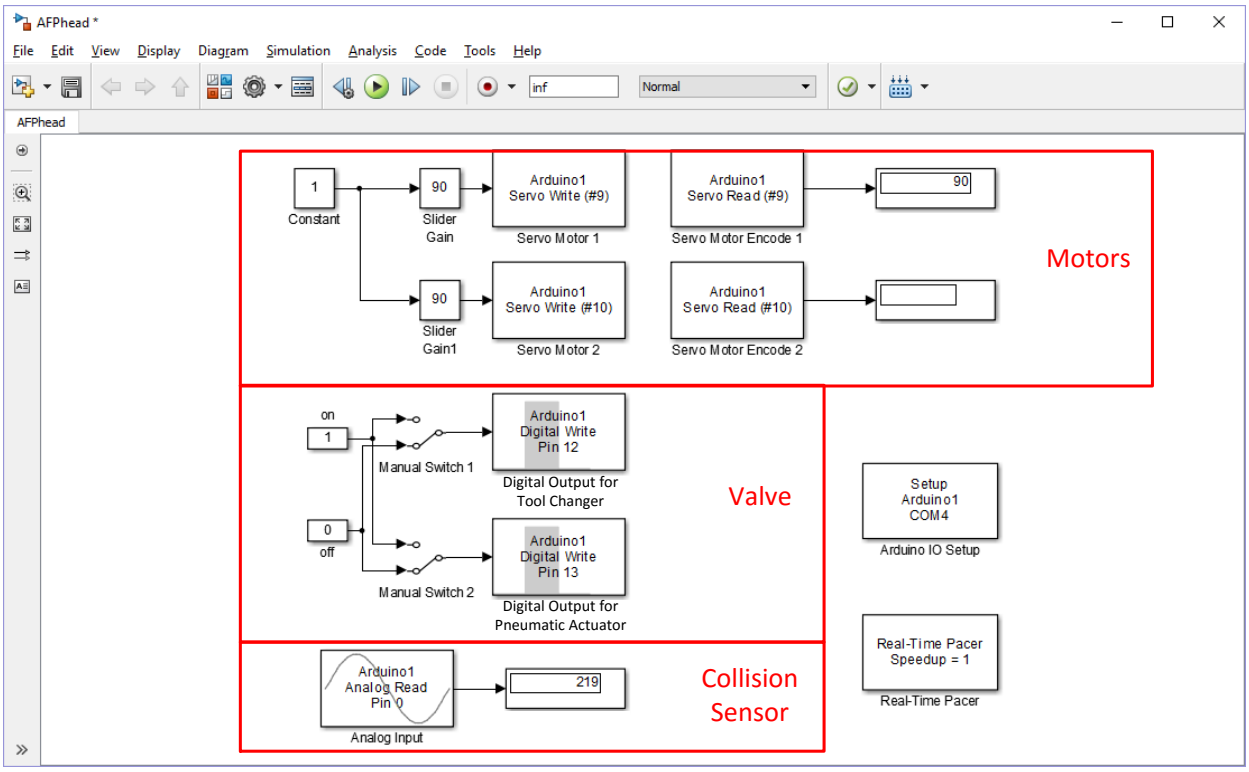

Figure 7.11. Control Diagram of the Micro-controller

Figure 7.11 shows the Simulink control diagram of Micro-controller. It controls two servo motors by using two “Arduino Servo Write” ports and receives feedback by reading the encodes of the servo motors via two “Arduino Servo Read” blocks. The solenoid valve is driven by two “Arduino Digital Write” pins. One is used to control the tool changer, and the other one is for controlling the pneumatic actuator to cut the fiber tows. The feedback signal of the collision sensor is received through “Arduino Analog Read” pin for the safety consideration. This signal will send to the controllers of the serial robot and the parallel robot to stop the cooperative AFP system immediately once the collision occurs.

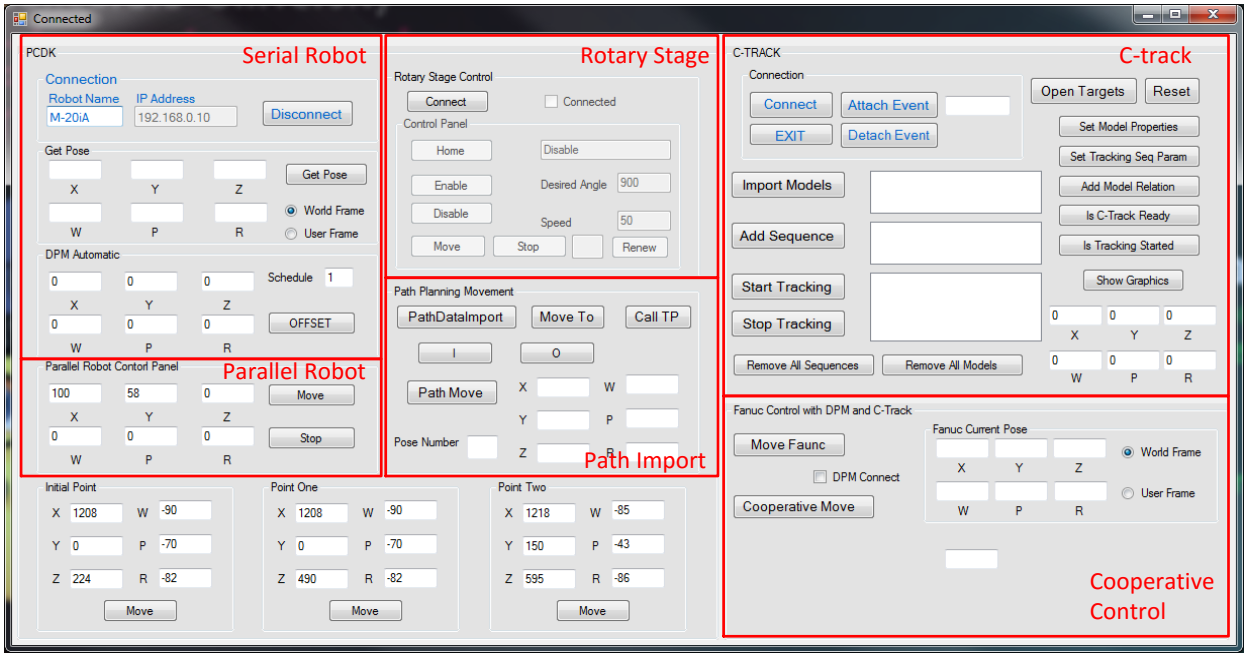

Figure 7.12. User Interface of VB

Figure 7.12 shows the control panel of the cooperative AFP system programmed by VB. It consists of six parts and the detail functions of these parts are explained as following.

1) “Serial Robot”:

   Computer-*A* connects to the controller of the Fanuc M20-iA using Ethernet connections which provides file transfer protocol (FTP) functions. And PCDK is applied for the communication of information and instructions. The current pose of the serial robot’s tool frame with respect to the world frame or the user frame is shown in the panel.

2) “Parallel Robot”:

   This panel transfers the six variables of the desired pose for the parallel robot, which consists of three variables of translation movement and three variables of orientation movement, to computer-*B* through the serial communication port.

3) “Rotary Stage”:

   It contains the control functions for the rotary stage using API provided by the Aerotech Inc.

4) “Path Import”:

Two ways of importing trajectory planning are applied in this control panel. One way is calling TP file, which is teach pendant program files that can be shared among Fanuc robots and edited using the teach pendant editor. It can either generated by programing via teach pendant manually or converting from .LS file created using the third party software off-line. The .LS file extension can be opened and edited in notepad on the PC. The other way is creating path file which contains the nodes of the desired pose off-line at first, then reading every node from the file and importing it into the controller of the serial robot in sequence. PCDK function ".MoveTo" is used to drive the serial robot to the desired pose.

5) "C-track":

   The controller of the C-track is connected through VXelements API in this control panel. The models which define the tool frames of the parallel robot and the serial robot as long as the base frame of the cooperative AFP system can imported into the control panel. Poses of the both tool frames of the serial robot and the parallel robot with respect to the base frame of the cooperative AFP system can be track simultaneously on-line.

6) "Cooperative Control":

   Based on the poses tracked by the C-track, the cooperative control which employs the semi-offline trajectory synchronized algorithm can be conducted in this control panel. Dynamic path modification (DPM) is applied to adding the correction to the pre-planned trajectory of the serial robot. It supports both modal DPM instruction and inline DPM instruction. The modal DPM is designed for the application that requires real time path modification along the entire motion path. While the inline DPM is designed for the application that requires real time modification on the destination position for each motion segment [160]. The control for the cooperative AFP system requires the certain kinematic relationship between the two robots, which means that the entire trajectory is needed to be modified. Thus, the modal DPM is used for the cooperative control. The path update rate is $8\ ms$.

The working principle of the cooperative AFP system mimics the process of two hands lay-up. In one hand, the tows are fed from the fiber processing head which is mounted on the end-effector of serial robot. The mandrel is held by the three-jaw chuck by the other hand. The rotary axis of three-jaw chuck is perpendicular to the upper platform of parallel robot. The pose of the mandrel can be adjusted by the parallel robot. During the fiber placement process, the end-effector of serial robot

must be orientated in such a way that the pressure of fiber processing head's compression roller always be normal to the surface of mandrel.

7.3 Experimental Tests

The experimental tests demonstrate the Y-shape AFP manufacturing process with joint limit and wrist singularity in the pre-planned path. The serial robot successfully passes the joint limit and singularity points by adding the compensation generated by parallel robot to the pre-planned path online.

7.3.1 Test One

Fanuc robot stops automatically when the joints reach to their limits. The quantitative definition of closeness has considered the balance between the workspace and constraint avoidance. If the threshold is chosen too large, the workspace of the serial robot will be reduced. On the other hand, if the threshold is chosen too small, the controller cannot avoid limit constraint points successfully due to the delay caused by the dynamic response of the whole system. After a lot of tests, it is found that $0.2°$ is an ideal threshold for the joint limits.

Figure 7.13 (a) illustrates the comparison of the actual trajectories of joint 5 with and without the correction at the joint limit point. The solid line indicates that the 5^{th} joint trajectory of the serial robot reaches to its limit, $120°$, and stops at the limit point without using the algorithm to generate the correction. The dotted line shows that the correction is added to the same pre-planned trajectory online when the 5^{th} joint reaches to $119.8°$, the 5^{th} joint passes the limit point and finishes the rest of the pre-planned path. Figure 7.13 (b) illustrates the actual trajectory of the Euler angle about axis Y of the parallel robot. The dotted line shows the offset movement when the 5^{th} joint of the serial robot reaches to $119.8°$.

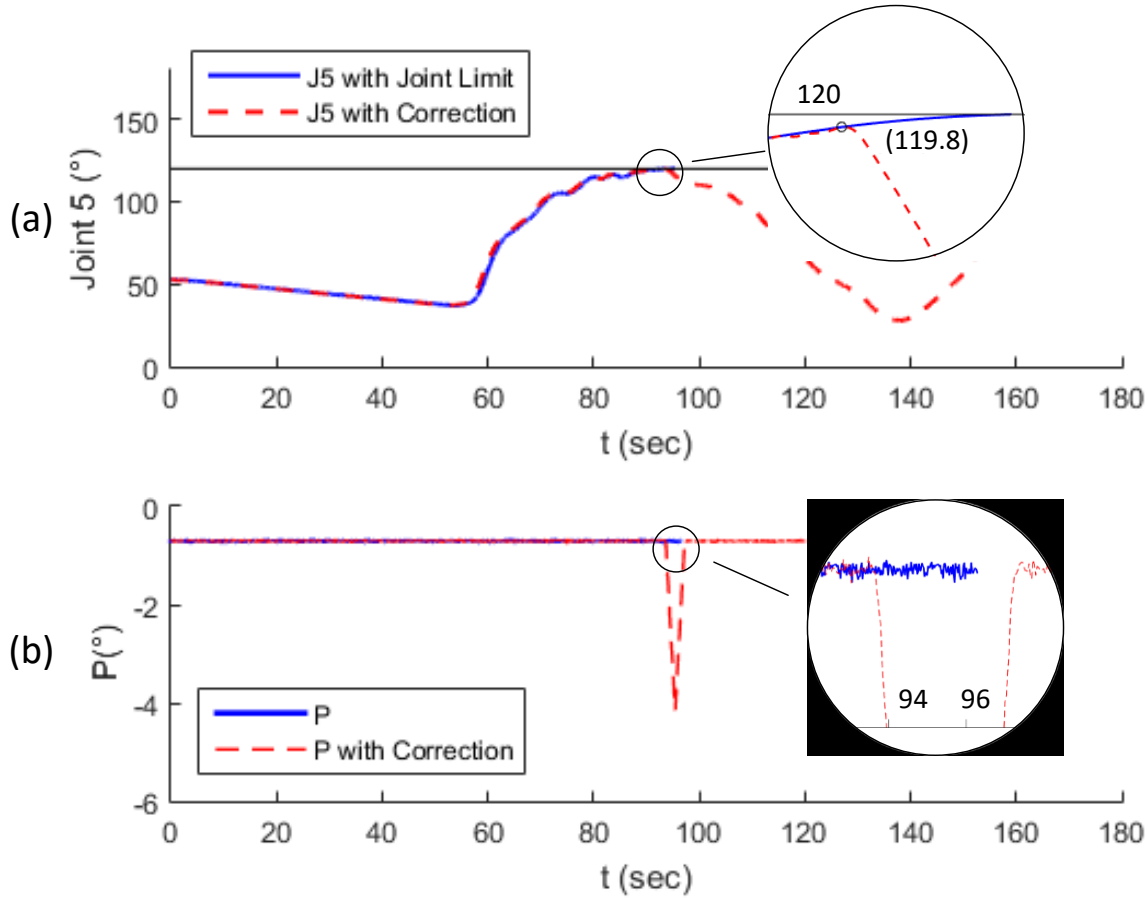

Figure 7.13. Trajectory with Joint Limit and Correction

a) Joint 5 of Serial Robot, b) Euler Angle of Parallel Robot

Figure 7.14. shows the comparison of the actual trajectories of the serial robot with and without the correction at the joint limit point. The blue line indicates that the serial robot stops when the 5^{th} joint reached the its limit when $J5 = 120°$. Using the same trajectory, the red line illustrates that the serial robot passes the limit point by adding the correction and finishes the trajectory.

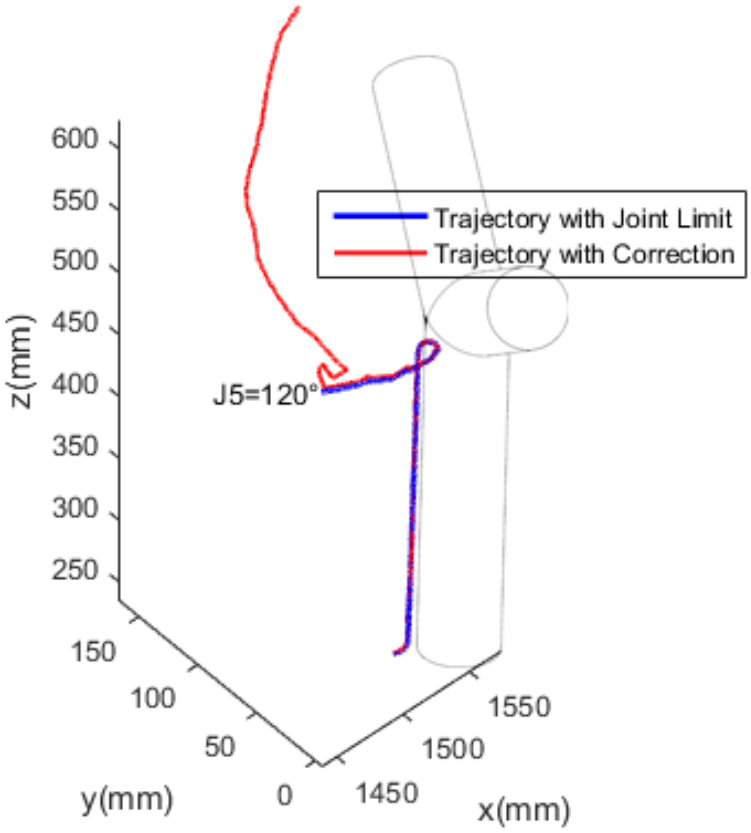

Figure 7.14. Trajectory of Serial Robot with Joint Limit and Correction

7.3.2 Test Two

For the safety consideration, Fanuc robot stops automatically when the 5th joint reaches to $\pm 3.5°$ due to the wrist singularity. Considering the balance between the workspace and singularity avoidance, it is found that 4.0° is an ideal threshold of the $\Delta\theta_{5min}$ for the wrist singularity after a lot of tests.

Figure 7.15. (a) illustrates the comparison of the actual trajectories of joint 5 with and without the correction at the wrist singularity point. The solid line indicates that the 5^{th} joint trajectory of the serial robot moves into its singularity area which is when $-3.5° \leq J5 \leq 3.5°$ and stops without using the algorithm to generate the correction. The dotted line shows that the correction is added to the same pre-planned trajectory online when the 5^{th} joint reaches to 4.0°, and the serial robot bypasses the wrist singularity and finishes the rest of the pre-planned path. Figure 7.15. (b)

illustrates the actual trajectory of the Euler angle about axis Y of the parallel robot. The dotted line shows the offset movement when the 5^{th} joint of the serial robot reaches to 4.0°.

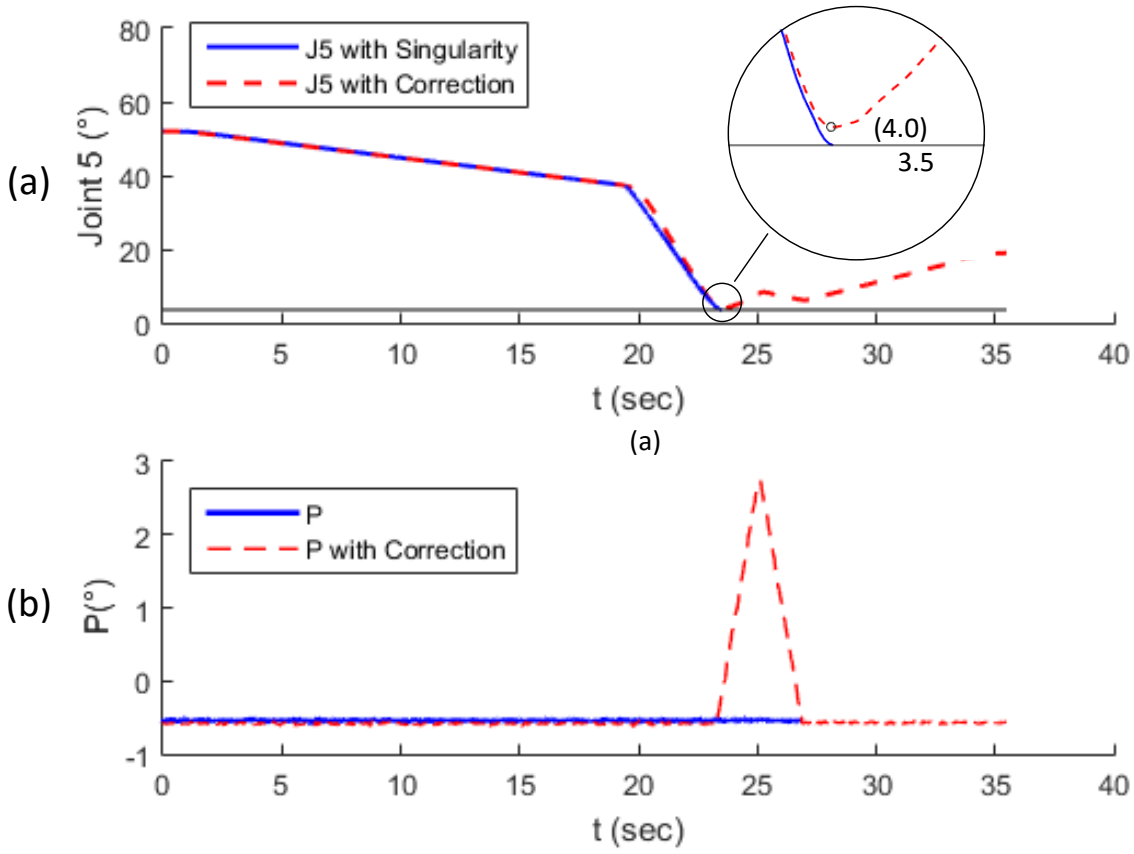

Figure 7.15. Trajectory with wrist singularity and Correction

a) Joint 5 of Serial Robot, b) Euler Angle of Parallel Robot

Figure 7.16. shows the comparison of the actual trajectories of the serial robot with and without the correction when the pre-planned path contains a wrist singularity.

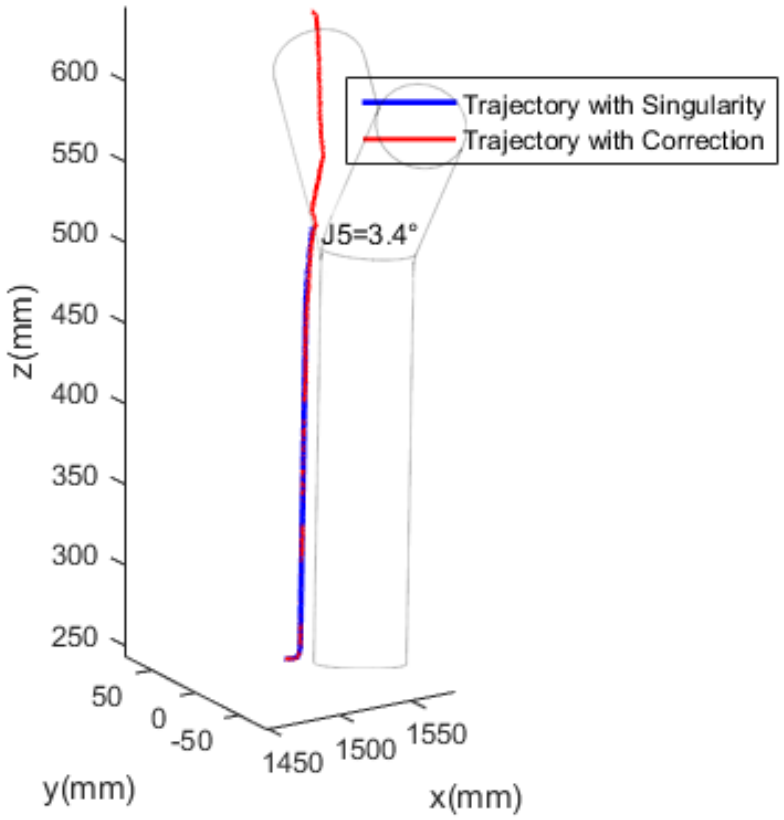

Figure 7.16. Trajectory of Serial Robot with wrist singularity and Correction

The experiment results demonstrate the successful avoidance of singularities and joint limits during manufacturing process. The pre-planned trajectory with joint limits and singularities is still feasible by using the proposed synchronized algorithm.

Videos of the cooperative AFP system using the proposed algorithm to avoid the limitation and singularity can be found at

Joint 5 Limit Avoidance: https://www.youtube.com/watch?v=EB51E2pBkqI

Wrist Singularity Avoidance: https://www.youtube.com/watch?v=Cezt3a2vlq8

For the safety consideration, a gap between the press point of the compression roller and the surface of the mandrel is kept in the experiments to avoid the collision.

7.4 Summary

In this chapter, the experimental setup of the cooperative AFP system is introduced at first. The cooperative AFP systems consists of one 6 RSS parallel robot, one 6 DOF serial manipulator, a fiber processing head, a spindle which is mounted on the platform. A photogrammetry sensor is applied for the visual feedback. The hardware structure of the cooperative AFP system is illustrated. Additionally, the control scheme of the cooperative AFP system is presented, which includes the control panel for computer-A programmed by VB, the Simulink files for computer-B to control the parallel robot and the fiber processing head and other components. Moreover, experimental tests demonstrate the cooperative AFP manufacturing process for Y-shape mandrel with joint limit and wrist singularity in the pre-planned trajectory using the proposed semi-offline trajectory synchronized algorithm. The serial robot successfully passes the joint limit and singularity points by adding the correction generated by semi-offline trajectory synchronized algorithm to the pre-planned trajectory online.

CHPATER 8

8 CONCLUSIONS AND RECOMMENDATIONS FOR FUTURE WORKS

8.1 Summary

Composite materials are being used widely in many industry areas such as aerospace, automobiles, wind turbines, civil infrastructures, medical devices etc. However, most of the current AFP machines are designed for the manufacture of airframe components, which are usually shallow shells or tubes, and are not capable of manufacturing more complex shapes.

To address this issue, a cooperative AFP system has been designed to manufacture composite material components with intrinsic shapes and to improve the production efficiency in this thesis. In order to fulfill the objectives, the modeling and control of the designed system has been carried out. The system includes a 6 DOF serial robot holding the fiber placement head, a 6-RSS parallel robot on which a one DOF mandrel holder is installed and a photogrammetry sensor to detect the poses of both end-effectors on parallel robot and serial robot. Since the AFP system has 13 DOF and owns the flexibility of manufacturing intrinsic composite structures, it poses great challenges for the overall control system design, trajectories planning, path tracking for laying up fibers on the mandrel etc.

The traditional way of trajectory planning is strictly subject to constraints of the robot, collision-free and singularity-free. Moreover, as to the trajectory planning of fiber placement, more requirements need to be satisfied, such as the limitation of minimum turning radius, defects resulted from gaps and overlaps, multiple layers, continuous laying without cutting tows to keep the consistent stress, and the roller of the fiber process head should be perpendicular to the surface

of the mold all the time. In the multiple robot machines such as the cooperative AFP system, the trajectories should be generated for each robot. When the manufactured composite part is of complicated shape, the trajectory generation for both robots free from collision and singularities and meanwhile satisfying the above requirements becomes increasing difficulty. In certain cases, no feasible trajectory can be generated for the continuous fiber placement. The traditional practice, namely, off-line generating path and inputting the generated path to robot controller for on-line fiber placement, cannot fulfil the task of manufacturing complicated composite components.

To meet the challenge, a semi-offline trajectory synchronized algorithm is proposed to incorporate the on-line robot control in following the paths generated off-line especially when the generated paths are infeasible for the current multiple robots to realize due to the constraints and singularities. By adding a correction to the paths of the robots at the points where the collision and singularity occur, the fiber can be laid up continuously without interruption. The correction is calculated based on the pose tracking data of the parallel robot detected by the photogrammetry sensor on-line. Due to the flexibility of the 6 DOF of the parallel robot, the optimized offsets with varying orientation and translation movements are generated based on the different singularities and constraints. To my best knowledge, this is the first time to consider the manipulation of both robots in the path tracking of AFP machine.

The procedure of manufacturing a particular composite material component with complex structure is shown as following. Before the procedure, the Denso robot in the simulator of SimMechanics need to be replaced by Fanuc M-20iA and the semi-offline trajectory synchronized algorithm need to be applied to the simulator.

- Generate off-line trajectories for the complex component. There might be singularity and constraint points existed in these trajectories.
- Input these off-line trajectories into the simulator to identify the collision points if there are any, and verify workspace of the whole system for the pre-planned trajectories after employing the synchronized algorithm.
- Apply these off-line trajectories to the cooperative AFP system. The singularity and constraint points in these trajectories would be avoided by using the semi-offline trajectory synchronized algorithm automatically. There is no need to identify the specific locations of the singularity or constraint points in the off-line trajectories.

8.2 Conclusions

This dissertation proposes a cooperative AFP system to manufacture more complicated structures of composite material components and presents an innovative semi-offline trajectory synchronized algorithm for the cooperative AFP system to free the planned trajectory from strictly subjecting to the constraints and singularities. The conclusions of the research work are listed as follows:

- The mathematical model of the cooperative AFP system including the forward and the inverse kinematics of the serial robot and the parallel robot is built. A numerical forward kinematic method, quasi-Gough forward kinematic algorithm, is presented to determine the uniqueness of forward kinematic solution of the 6-RSS parallel robot. The process of calculating the inverse kinematic of the serial robot based on Denso robot is given. To deal with the multiple solutions, the shortest distance rule is used to choose a solution closest to the current robot.
- A comprehensive analysis on constraints and singularities of the cooperative AFP system is given. Kinematic constraint consists of the workspace constraint and the joints space constraint. Three types of singularities for the wrist-partitioned serial robot, which are elbow singularity, shoulder singularity and wrist singularity, are derived.
- The pose estimation using a photogrammetry sensor is introduced, and the processes of the frame definitions for both the parallel robot and the serial robot are presented. In order to refine the kinematic model and the CAD model of the 6-RSS parallel robot, some parameters in parallel robot's kinematic model are calibrated using the photogrammetry sensor, i.e. C-track.
- The semi-offline trajectory synchronized algorithm for the cooperative AFP system is developed to calculate the pose correction based on the measured poses and add the correction to the pre-planned trajectory for avoiding singularities, optimizing joint limits and expanding the workspace on-line. The off-line trajectory planning and the decomposition processes for the cooperative AFP system is illustrated. The generated offsets for the parallel robot are calculated based on different conditions including singularity avoidance and joints constraints avoidance.

- Simulation on the proposed cooperative AFP system including a 6-DOF RSS parallel and a 6-DOF Denso robot is conducted in SimMechanics for fiber placement of the bowl shape mandrel.
- Experimental tests of the cooperative AFP manufacturing process have been conducted on fiber placement of a Y-shape mandrel with joint limit and wrist singularity in the pre-planned trajectory. The test results show that the proposed semi-offline trajectory synchronized algorithm succeeds in avoiding the singularities and joint limits during the manufacturing process.

To sum up, the designed multi-robot system poses high demand for trajectory planning than those by the current APF machine. The semi-offline trajectory synchronized algorithm for the cooperative AFP system presented in this dissertation could avoid singularities, optimize joint limits and expand the workspace on-line by fully using the flexibility of the 13-DOF system. Thus, for the fiber placement cases with infeasible path for continuous laying up the fiber due to the requirement of free from collisions, and singularities, the proposed cooperative AFP system can still be operated by using the control algorithm. The experimental tests demonstrate that the proposed cooperative AFP system is capable of perform the motion of manufacturing more complex composite components.

8.3 Future Works

There are some recommended studies that need further investigations, which are listed below:

- The gaps and overlaps on the intersection part of the Y-shape mandrel need to be analyzed.
- Off-line trajectories for the cooperative AFP system, including the pre-planned trajectories of the serial robot, the parallel robot and the rotary stage, to manufacture more complicated shapes are required.
- Filter need to be applied for the C-track measurement,
- The accuracy of the coordination control for the cooperative AFP system need to be increased by implementing closed-loop pose correction controller.

- Apply the developed cooperative AFP system to the current AFP in Concordia University lab and manufacture the actual composite structure.

REFERENCES

[1] D. Groppe, “Robots Improve the Quality and Cost-effectiveness of Composite Structures”, *Industrial Robot*, 27 (2000), 96-102.

[2] M. Ahrens, V. Mallick, K. Parfrey, “Robotic Based Thermoplastic Fibre Placement Process”, *IEEE International Conference on Robotics and Automation*, 2 (1998) 1148-1153.

[3] I. Shyha, S.L. Soo, D. Aspinwall, S. Bradley, “Effect of laminate configuration and feed rate on cutting performance when drilling holes in carbon fibre reinforced plastic composites”, *Journal of Materials Processing Technology*, 210 (2010) 1023-1034.

[4] H. Hocheng, C.C. Tsao, “The path towards delamination-free drilling of composite materials”, *Journal of Materials Processing Technology*, 167 (2005) 251-264.

[5] A.P. Singh, M. Sharma, I. Singh, “A review of modeling and control during drilling of fiber reinforced plastic composites”, *Composites: Part B*, 47 (2013) 118 – 125.

[6] S. Bijan, C. Gary, O. Denny, G. Alici, M.H. Ang, “Trajectory generation for open-contoured structures in robotic fibre placement”, *Robotics and Computer-Integrated Manufacturing*, 23 (2007) 380-394.

[7] S. Bijan, W.F. Chee, H.T. Boon, “Robotic fibre placement process planning and control”, *Assembly Automation*, 20 (2000) 313-320.

[8] P. Debout, H. Chanal, E. Duc, “Tool path smoothing of a redundant machine: Application to Automated Fiber Placement”, *Computer-Aided Design,* 43 (2011) 122-132.

[9] S. Bijan, A. Gursel, W.F. Chee, C. Gary, “Fabrication process of open surfaces by robotic fibre placement”, *Robotics and Computer Integrated Manufacturing,* 20 (2004) 17-28.

[10] D.H.-J.A. Lukaszewicz, C. Ward, K.D. Potter, “The engineering aspects of automated prepreg layup: History, present and future”, *Composites: Part B,* 43 (2012) 997-1009.

[11] H.B. Olsen, J.J. Craig, “Automated composite tape-lay-up using robotic devices”, *Proceedings IEEE International Conference on Robotics and Automation,* 3 (1993) 291-297.

[12] R. Costen, J. Marchello, “Tape-drop transient model for in-situ automated tape placement of thermoplastic composites”, *Proceedings of the International SAMPE symposium and exhibition*, 44 (1990) 1820-1830.

[13] J. Tierney, J.W. Gillespie, “Modeling of Heat Transfer and Void Dynamics for the Thermoplastic Composite Tow-placement Process”, *Journal of Composite Materials*, 37 (2003) 1745-1768.

[14] B. Dasgupta, T.S. Muthyunjaya, “The Stewart platform manipulator: a review”, *Mechanism and Machine Theory*, 35 (2000) 15-40.

[15] E.K. Zanganeh, R. Sinatra, J. Angeles, “Kinematics and dynamics of a six-degree-of-freedom parallel manipulator with revolute legs”, *Robotics*, 15 (1997) 285-294.

[16] X.M. Zhang, W.F. Xie, S.V. Hoa, R. Zeng, “Design and Analysis of Collaborative Automated Fiber Placement Machine”, *International Journal of Advanced Robotics and Automation*, 1 (2016) 1-14.

[17] A.N. Mahdi, F. Kazem, P. Damiano, L. Larry, “Optimization of variable stiffness composites with embedded defects induced by Automated Fiber Placement”, *Composite Structures*, 107 (2014) 160-166.

[18] K. Kozaczuk, “Automated Fiber Placement Systems Overview”, *Transactions of the institute of aviation*, 4 (2016) 52-59.

[19] Coriolis, https://www.coriolis-composites.com/sector-solutions/aerospace.html, (2017).

[20] Electroimpact, https://www.electroimpact.com/Products/Composites/Overview.aspx, (2017).

[21] MTorres, http://www.mtorres.es/en/aeronautics/products/carbon-fiber/torresfiberlayup, (2017).

[22] Ingersoll, http://www.camozzimachinetools.com/en/camozzigroup/machine-tools/products/composite-technology/automated-fiber-placement-lynx-series, (2017).

[23] D. Stewart, "A platform with six degrees of freedom", *in Proc. Inst. Mech. Engr.*, 180 (1965) 371-386.

[24] V.E. Gough, S.G. Whitehall, "Universal tyre test machine", *in: Proc. 9th Int. Tech. Congr. F.I.S.I.T.A,* (1965) 117-137.

[25] K. Liu, J.M. Fitzgerald, F.L. Lewis, "Kinematic Analysis of a Stewart Platform Manipulator", *IEEE Transactions on Industrial Electronics*, 40 (1993) 282-293.

[26] B.Y. Ding, B.S. Cazzolato, R.M Stanley, S. Grainger, J.J. Costi, "Stiffness analysis and control of a Stewart platform-based manipulator with decoupled sensor-actuator locations for ultrahigh accuracy positioning under large external loads", *Journal of Dynamic Systems, Measurement and Control, Transactions of the ASME,* 136 (2014).

[27] V. Nabat, M. De La O Rodriguez, O. Company, S. Krut, F. Pierrot, "Par4: Very high speed parallel robot for pick-and-place", *IEEE/RSJ International Conference on Intelligent Robots and Systems,* (2005) 1202-1207.

[28] J. Hesselbach, J. Wrege, A. Raatz, O. Becker, "Aspects on design of high precision parallel robots", *Assembly Automation*, 24 (2004) 49-57.

[29] H. Gonzalez, M.S. Dutra, O. Lengerke, "Direct and inverse kinematics of Stewart platform applied to offshore cargo transfer simulation", *13th world congress in Mechanism and Machine Science*, (2011) 19-25.

[30] J. Pieper, "Design of a Stewart Platform for General Machining Using Magnetic Bearings" (2004).

[31] J.S. Albus, R. Bostelman, and N.G. Dagalakis, “The NIST ROBOCRANE”, *Journal of Robotic Systems*, 10 (1993) 709-724.

[32] M. Ceccarelli, E. Ottaviano, “A workspace evaluation of an eclipse robot”, *Robotica*, 20 (2002) 299-313.

[33] P. Nanua, K.J. Waldron, “Direct Kinematic Solution of a Stewart Platform”, *IEEE Transactions on Robotics and Automations*, 6 (1989) 438-444.

[34] J.P. Merlet, 2004. “Solving the Forward Kinematics of a Gough-Type Parallel Manipulator with Interval Analysis”, *The International Journal of Robotics Research*, 23 (2004) 221-235.

[35] L. Baron, J. Angeles, “The Direct Kinematics of Parallel Manipulators under Joint-Sensor Redundancy”, *IEEE Transactions on Robotics and Automation*, 16 (2000) 12-19.

[36] E.F. Fichter, E.D. McDowell, “Determining the motions of joints on a parallel connection manipulators”, *Theory Mac. Mech.,* (1984) 1003-1006.

[37] M.G. Mohamed, J. Sanger, J. Duffy, “Instantaneous kinematics of fully-parallel devices”, *Theory Mac. Mech.,* (1984) 77-80.

[38] M.H. Perng, L. Hsiao, “Inverse Kinematic Solutions for a Fully Parallel Robot with Singularity Robustness”, *The International Journal of Robotics Research*, 18 (1999) 575-583.

[39] F.A. DeWitt, “An inverse kinematics approach to hexapod design and control”, *Proceedings of the SPIE - The International Society for Optical Engineering,* 7424 (2009) 74240O1-9.

[40] R. Nair, J.H. Maddocks, “On the forward kinematics of parallel manipulators”, *International Journal Robotics Research*, 13 (1994) 171-188.

[41] B. Dasgupta, T.S. Mruthyunjaya, “A Constructive Predictor-Corrector Algorithm for the Direct Position Kinematics Problem for a General 6-6 Stewart Platform”, *Mech. Mach. Theory*, 31 (1996) 799-811.

[42] F. Wen, C. Liang, “Displacement Analysis of the 6-6 Stewart Platform Mechanism”, *Mech. Mach. Theory*, 29 (1994) 547-557.

[43] Z. Geng, L. Haynes, "Neural network solution for the forward kinematics problem of a Stewart platform", *Proc. IEEE Int. Conf. Robotics and Automation*, (1991) 2650-2655.

[44] S. Kucuk, Z. Bingul, "Robot workspace optimization based on a novel local and global performance indices", *IEEE International Symposium on Industrial Electronics*, (2005) 1593-1598.

[45] J.P. Merlet, "Determination of the Orientation Workspace of Parallel Manipulators", *Journal of Intelligent and Robotic Systems*, 13 (1995) 143-160.

[46] I.A. Bonev, J. Ryu, "A new Approach to Orientation Workspace Analysis of 6-DOF Parallel Manipulators", *Mechanism and Machine Theory*, 36 (2001) 15-28.

[47] B. Monsarrat, C.M. Gosselin, "Workspace Analysis and Optimal Design of a 3-Leg 6-DOF Parallel Platform Mechanism", *IEEE Transactions on Robotics and Automation*, 19 (2003) 954-966.

[48] Q.M. Jiang, C.M. Gosselin, "The Maximal Singularity-Free Workspace of the Gough-Stewart Platform for a Given Orientation", *Journal of Mechanical Design*, 130 (2008) 1123041-1123048.

[49] I.A. Bonev, C.M. Gosselin, "Geometrical algorithms for the computation of the constant-orientation workspace and singularity surfaces of a special 6-RUS parallel manipulator", *Proceedings of the ASME Design Engineering Technical Conferences*, 5 (2002) 505-514.

[50] J. Blaise, I. Bonev, B. Monsarrat, S. Briot, J.M. Lambert, C. Perron, "Kinematic characterisation of hexapods for industry", *Industrial Robot*, 37 (2010) 79-88.

[51] M.M. Stanisic, O. Duta, "Symmetrically Actuated Double Pointing Systems: The Basis of Singularity-Free Robot Wrists", *IEEE TRANSACTIONS ON ROBOTICS AND AUTOMATION*, 6 (1990) 562-569.

[52] P.S. Donelan, "Singularity-theoretic methods in robot kinematics", *Robotica*, 25 (2007) 641-659.

[53] G.L. Yang, I.M. Chen, W. Lin, J. Angeles, “Singularity Analysis of Three-Legged Parallel Robots Based on Passive-Joint Velocities”, *IEEE Transactions on Robotics and Automation*, 17 (2001) 413-422.

[54] J.P. Merlet, D. Daney, “A Formal-Numerical Approach to Determine the Presence of Singularity Within the Workspace of a Parallel Robot”, *Proceedings of the International Workshop on Computational Kinematics*, 20 (2001) 167-176.

[55] S. Sen, B. Dasgupta, A.K. Mallik, “Variational Approach for Singularity-Free Path-Planning of Parallel Manipulators”, *Mech. Mach. Theory*, 38 (2003) 1165-1183.

[56] S. Amine, S. Caro, P. Wenger, D. Kanaan, “Singularity analysis of the H4 robot using Grassmann-Cayley algebra”, *Robotica,* 30 (2012) 1109-1118.

[57] D. E. Whitney, “Resolved motion rate control of manipulators and human prostheses”, *IEEE Trans. Man. Mach. Syst.*, 10 (1969) 47-53.

[58] R. Featherstone, “Position and velocity transformations between robot end-effector coordinates and joint angles”, *Int. J. Robot. Res*., 2 (1983) 35-45.

[59] K. H. Hunt, “Kinematic Geometry of Mechanisms”, *Clarendon Press*, (1978).

[60] K. Sugimoto, J. Duffy, K. H. Hunt, “Special configurations of spatial mechanisms and robot arms”, *Mech. Mach. Theory,* 17 (1982) 119-132.

[61] K. H. Hunt, “Special configurations of robot arms via screw theory-Part I: The Jacobian and its matrix cofactors,” *Robotica,* 4 (1986) 171-179.

[62] K. H. Hunt, “Special configurations of robot arms via screw theory-Part II: Available end-effector displacements”, *Robotica*, 5 (1987) 17-22.

[63] F. L. Litvin, V. Parenti-Castelli, “Configurations of robot manipulators and their identification and the execution of prescribed trajectories”, *Trans. ASME J. Mech., Transm. Autom. Design,* 107 (1985) 170-188.

[64] F. L. Litvin, Z. Yi, V. Parenti-Castelli, C. Innocenti, "Singularities, configurations and displacement functions for manipulators", *Int. J. Robot. Res.,* 5 (1986) 66-74.

[65] S. L. Wang and K. J. Waldron, "A study of the singular configurations of serial manipulators", *Trans. ASME J. Mech. Transm. Autom. Design,* 109 (1987) 14-20.

[66] M. Zribi, M. Karkoub, L.L. Huang, "Modelling and control of two robotic manipulators handling a constrained object", *Applied Mathematical Modelling*, 24 (2000) 881-898.

[67] W. Gueaieb, F. Karray, "A Robust Hybrid Intelligent Position/Force Control Scheme for Cooperative Manipulators", *IEEE/ASME Transactions on Mechatronics*, 12 (2007) 109-125.

[68] M. Zribi, L.L. Huang, S.P. Chan, "Position and Force Control of Two Constrained Robotic Manipulators", *Journal of Intelligent and Robotic Systems*, 24 (1999) 1-22.

[69] P. Hsu, "Coordinated Control of Multiple Manipulator Systems", *IEEE Transactions on Robotics and Automation*, 9 (1993) 400-410.

[70] M.A. Unseren, "A rigid body model and decoupled control architecture for two manipulators holding a complex object", *Robotics and Autonomous Systems*, 10 (1992) 115-31.

[71] C.O. Alford, S.M. Belyeu, "Coordinated control of two robot arms", *Proc. of IEEE Int. Conf. on Robotics and Automation*, (1984) 468-473.

[72] Y. Nakamura, K. Nagai, T. Yoshikawa, "Mechanics of coordinative manipulation by multiple robotic mechanisms", *Proc. IEEE Int. Con & Robotics Auto.,* (1987) 991-998.

[73] T.J. Tarn, A.K. Bejczy, X. Yun, "Control of two coordinated robots", *Proc. IEEE Int. Con& Robotics Auto.*, (1986) 1193-1202.

[74] P. Hsu, "Coordinated control of multiple manipulator systems", *IEEE Trans. Robotics Auto*., 9 (1993) 400–410.

[75] J. Wen, K. Kreutz, "Motion and force control for multiple cooperative manipulators", *Proc. IEEE Int. Con & Robotics Auto.,* (1989) 1246-1251.

[76] Y.F. Zheng, J.Y.S. Luh, "Optimal load distribution for two industrial robots handling a single object", *Transactions of the ASME. Journal of Dynamic Systems, Measurement and Control*, 111 (1989) 232-237.

[77] E. Samiei, M. Shafiee, "Descriptor Modeling and Response Analysis of Two Rigid-Flexible Cooperative Arms", *Int. Conf. Control, Automation, Robotics and Vision*, (2010) 149-156.

[78] N.H. McClamroch, D.W. Wang, "Feedback stabilization and tracking of constrained robots", *IEEE Trans. Automat. Control*, 33 (1988) 419-426.

[79] R.K. Kankaanranta, H.N. Koivo, "Dynamics and simulation of complaint motion of a manipulator", *IEEE J. of Robotics Automat*. 4 (1988) 163–173.

[80] M. Zribi, S. Ahmad, "Adaptive control for multiple cooperative robot arms", *Proc. of the 31st Conf. on Decision and Control*, 2 (1992) 1392-1398.

[81] M.W. Walker, D. Kim, J. Dionise, 1989. "Adaptive coordinated control of two manipulator Arms", *Proc. IEEE Int. Conf. on Robotics and Auto.*, 2 (1989) 1084-1090.

[82] S.S. Ge, L. Huang, T.H. Lee, "Model-based and neural-network-based adaptive control of two robotic arms manipulating an object with relative motion", *International Journal of Systems Science*, 32 (2001) 9-23.

[83] C.S. Chiu, K.Y. Lian, T.C. Wu, "Robust adaptive motion/force tracking control design for uncertain constrained robot manipulators," *Automatic*, 40 (2004) 2111-2119.

[84] E. Kim, "Output feedback tracking control of robot manipulators with model uncertainty via adaptive fuzzy logic," *IEEE Trans. Fuzzy Syst.*, 12 (2004) 368–378.

[85] K. Burn, M. Short, R. Bicker, "Adaptive and nonlinear fuzzy force control techniques applied to robots operating in uncertain environments", *J. Robot. Syst.*, 20 (2003) 391-400.

[86] P.G. Ranky, "Collaborative, synchronous robots serving machines and cells", *Industrial Robot: An International Journal*, 30 (2003) 213–217.

[87] J. Minguez, L. Montano, "Nearness Diagram (ND) Navigation: Collision Avoidance in Troublesome Scenarios", *IEEE Transactions on Robotics and Automation*, 20 (2004) 45-59.

[88] C.T. Cai, C.S. Yang, Q.D. Zhu, Y.H. Liang, "A Fuzzy-based Collision Avoidance Approach for Multi-robot Systems", *Proceedings IEEE International Conference on Robotics and Biomimetics*, (2007) 1012-1017.

[89] J. Cascio, M. Karpenko, Q. Gong, P. Sekhavat, I.M. Ross, "Smooth Proximity Computation for Collision-Free Optimal Control of Multiple Robotic Manipulators", *IEEE/RSJ International Conference on Intelligent Robots and Systems*, (2009) 2452-2457.

[90] E.A. Merchán-Cruz, A.S. Morris, "Fuzzy-GA-Based Trajectory Planner for Robot Manipulators Sharing a Common Workspace," *IEEE TRANSACTIONS ON ROBOTICS*, 22 (2006) 613-624.

[91] S. Lee, H. Moradi, "A Real-Time Dual-Arm Collision Avoidance Algorithm for Assembly", *Journal of Robotic Systems*, 18 (2001) 477-486.

[92] M. Mediavilla, J.L. González, J.C. Fraile, J.R. Perán, "Reactive approach to on-line path planning for robot manipulators in dynamic environments", *Robotica*, 20 (2002) 375-384.

[93] Y.S. Shen, K. Hüper, Optimal trajectory planning of manipulators subject to motion constraints, International Conference on Advanced Robotics. (2005) 9-16.

[94] S.S. Parsa, H.M. Daniali, R. Ghaderi, "Optimization of parallel manipulator trajectory for obstacle and singularity avoidances based on neural network", *International Journal of Advanced Manufacturing Technology*, 51 (2010) 811-816.

[95] J.E. Lloyd, V. Hayward, "Singularity-Robust Trajectory Generation", *International Journal of Robotics Research*, 20 (2001) 38-56.

[96] R. Saravanan, S. Ramabalan, C. Balamurugan, "Evolutionary optimal trajectory planning for industrial robot with payload constraints", *International Journal of Advanced Manufacturing Technology*, 38 (2008) 1213-1226.

[97] A.W. Blom, B.F. Tatting, J. Hol, Z. Gürdal, "Fiber path definitions for elastically tailored conical shells", *Composites Part B: Engineering*, 40 (2009) 77-84.

[98] F. Kazem, A.N. Mahdi, P. Damiano, L. Larry, "Defect layer method to capture effect of gaps and overlaps in variable stiffness laminates made by Automated Fiber Placement", *Composite Structures*, 97 (2013) 245-251.

[99] A. Alhajahmad, M.M. Abdalla, Z. Gürdal. "Optimal design of tow-placed fuselage panels for maximum strength with buckling considerations", *J Aircraft*, 47 (2010) 775–82.

[100] A.J. Sawicki, P.J. Minguet, "The Effect of intraply overlaps and gaps upon the compression strength of composite laminates", *In: 39th AIAA structural, dynamics, & materials conference*, 1 (1998) 744-754.

[101] D.S. Cairns, L.B. Licewicz, T. Walker, "Response of automated tow-placed laminates to stress concentrations", *Comput Eng*., (1993) 649–663.

[102] K. Croft, L. Lessard, D. Pasini, M. Hojjati, J. Chen, A. Yousefpour, "Experimental study of the effect of Automated Fiber Placement induced defects on the performance of composite laminates", *Computer Part A*, 42 (2011) 484–491.

[103] A.W. Blom, C.S. Lopes, P.J. Kromwijk, Z. Gürdal, "A theoretical model to study the influence of tow-drop areas on the stiffness and strength of variable stiffness laminates", *Comput. Mater.,* 43 (2009) 403-425.

[104] C.S. Lopes, P.P. Camanho, Z. Gürdal, B.F. Tatting, "Progressive failure analysis of tow-placed, variable-stiffness composite panels", *Int. J Solids Struct.,* 44 (2007) 8493–8516.

[105] M. Bruyneel, S. Zein, "A modified Fast Marching Method for defining fiber placement trajectories over meshes", *Computers & Structures*, 125 (2013) 45-52.

[106] C.J. Brampton, K.C. Wu, H.A. Kim, "New optimization method for steered fiber composites using the level set method", *Structural and Multidisciplinary Optimization,* 52 (2015) 493-505.

[107] L. Parnas, S. Oral, U. Ceyhan, “Optimum design of composite structures with curved fiber courses”, *Composites Science and Technology,* 63 (2003) 1071-1082.

[108] A.W. Blom, P.B. Stickler, Z. Gürdal, “Optimization of a composite cylinder under bending by tailoring stiffness properties in circumferential direction”, *Composites: Part B*, 41 (2010) 157-165.

[109] C. Waldhart, Z. Gürdal, C. Ribbens, “Analysis of tow-placed, parallel fiber, variable stiffness laminates”, *In: Proceedings of AIAA/ASME/ASCE/ AHS/ASC Structures, Structural Dynamics, and Materials Conference*, (1996) 2210-2220.

[110] J.Y. Zhang, C. Zhao, D.W. Zhang, “Pose accuracy analysis of robot manipulators based on kinematics”, *Advanced Materials Research*, 201-203 (2011) 1867-1872.

[111] B. Shirinzadeh, P.L. Teoh, Y. Tian, M.M. Dalvand, Y. Zhong, H.C. Liaw, “Laser interferometry-based guidance methodology for high precision positioning of mechanisms and robots”, *Robotics Computer-Integrated Manuf*., 26 (2010) 74-82.

[112] M. Vincze, J.P. Prenninger, H. Gander, “A laser tracking system to measure position and orientation of robot end effectors under motion”, *Int. J. Robotics Res*., 13 (1994) 305-314.

[113] B. Liu, F.M. Zhang, X.H. Qu, “A Method for Improving the Pose Accuracy of a Robot Manipulator Based on Multi-Sensor Combined Measurement and Data Fusion”, *Sensors*, 15 (2015) 7933-7952.

[114] J. Hefele, C. Brenner, “Robot pose correction using photogrammetric tracking”, *In Proceedings of Intelligent Systems and Smart Manufacturing - International Society for Optical Engineering*, 4189 (2001) 170–178.

[115] D.R. Hans, B. Beno, “Visual-model-based, real-time 3D pose tracking for autonomous navigation: Methodology and experiments”, *Auto. Robot*, 25 (2008) 267–286.

[116] V. Kyrki, K. Schmock, “Integration methods of model-free features for 3D tracking”, *Lecture notes in computer science*, 3540 (2005) 557-566.

[117] M. Vincze, M. Schlemmer, P. Gemeiner, M. Ayromlou, “Vision for robotics: a tool for model-based object tracking”, *IEEE Robotics & Automation Magazine*, 12 (2005) 53-64.

[118] J. Hefele, C. Brenner, “Real-time photogrammetric algorithms for robot calibration”, *Int. Archives Photogramm. Remote Sens. Spat. Inf. Sci*. 34 (2002) 33-38.

[119] F. Chaumette, S. Hutchinson, “Visual servo control. Part I. Basic approaches”, *IEEE Robot. Autom. Mag*., 13 (2006) 82-90.

[120] M. Keshmiri, W.F. Xie, A. Mohebbi, “Augmented image-based visual servoing of a manipulator using acceleration command”, *IEEE Transactions on Industrial Electronics*, 61 (2014) 5444-5452.

[121] J. Feddema, O. Mitchell, “Vision-guided servoing with feature-based trajectory generation”, *IEEE Trans. Robot. Automat*., 5 (1989) 691-700.

[122] D.H. Park, J.H. Kwon, I.J. Ha, “Novel position-based visual servoing approach to robust global stability under field-of-view constraint”, *IEEE Trans. on Ind. Electron.,* 59 (2012) 4735-4752.

[123] W.J. Wilson, C.C.W. Hulls, G.S. Bell, “Relative end-effector control using Cartesian position based visual servoing”, *IEEE Transactions on Robotics and Automation*, 12 (1996) 684-696.

[124] L.F. Deng, F. Janabi-Sharifi, W.J. Wilson, “Hybrid motion control and planning strategies for visual servoing”, *IEEE Transactions on Industrial Electronics*, 52 (2005) 1024-1040.

[125] E. Malis, F. Chaumette, S. Boudet, “2-1/2-D visual servoing”, *IEEE Trans. Robot. Autom.,* 15 (1999) 238-250.

[126] F. Chaumette, “Potential problems of stability and convergence in image-based and position based visual servoing”, *Confluence of Vision and Control*, 237 (1998) 66-78.

[127] B. Espiau, “Effect of camera calibration errors on visual servoing in robotics”, *in Proc. 3rd Int. Symp. Exp. Robot.,* (1993) 182-192.

[128] M. Baumann, S. Leonard, E.A. Croft, J.J. Little, “Path planning for improved visibility using a probabilistic road map”, *IEEE Trans. Robot.,* 26 (2010) 195-200.

[129] J.F. Larue, D. Brown, M. Viala, “How Optical CMMs and 3D Scanning Will Revolutionize the 3D Metrology World”, Industrial Inspection, Advances in Computer Vision and Pattern Recognition. Springer, (2015)141-176.

[130] K.B. Atkinson, “Close range photogrammetry and machine vision”, *Whittles Publishing*, (2001).

[131] M.H. Perng, L. Hsiao, “Inverse Kinematic Solutions for a fully parallel Robot with singularity robustness”, *The International Journal of Robotics Research*, 18 (1999) 575-583.

[132] J.E. Dieudonne, R.V. Parrish, R.E. Bardusch, “An actuator extension transformation for a motion simulator and an inverse transformation applying Newton-Raphson's method”, *National Aeronautics and Space Administration Technical Reports*, (1972).

[133] B. Hyman, E.H. Connell, D. Wright, “The Jacobian conjecture: reduction of degree and formal expansion of the inverse” *Bull. Amer. Math. Soc.,* 72 (1982) 287-330.

[134] J.H. Wilkinson, “The algebraic eigenvalue problem”, *Oxford: Clarendon Press*, 87 (1965).

[135] R. Zeng, S.L. Dai, W.F. Xie, X.M. Zhang, “Determination of the proper motion range for the rotary actuators of 6-rss parallel robot”, *CCToMM Mechanisms*, *Machines and Mechatronics (M3) Symposium*, (2015).

[136] Q.J. Wang, J.J. Du, “A new solution for inverse kinematics problems of MOTOMAN robot”, *Journal of Harbin Institute of Technology,* 42 (2010) 451-454.

[137] “SimMechanics User’s Guide”, *The MathWorks.Inc.,* (2007).

[138] L.T. Yu, L.X. Zhang, N. Zhang, S. Yang, D.M. Wang, “Kinematics Simulation and Analysis of 3-RPS parallel robot on SimMechanics”, *Proceedings of IEEE International Conference on Information and Automation*, (2010) 2363-2367.

[139] M. Raghavan, “The Stewart platform of general geometry has 40 configurations”, *Journal of Mechanical Design, Transactions of the ASME*, 115 (1993) 277-280.

[140] M. Keshmiri, W.F. Xie, Image-Based Visual Servoing Using an Optimized Trajectory Planning Technique, *IEEE/ASME Transactions on Mechatronics*. 22 (2017) 359-70.

[141] C. Gosselin, J. Angeles, “Singularity Analysis of Closed-Loop Kinematic Chains”, *IEEE Transactions on Robotics and Automation*, 6 (1990) 281-290.

[142] J.P. Merlet, “Singular configurations of parallel manipulators and Grassmann geometry”, *The International Journal of Robotics Research,* 8 (1989) 45-56.

[143] R. Zeng Y.J. Zhao, S.L. Dai, “The proper motion domain for the actuators of Stewart-Gough platform”, *Guidance, Navigation and Control Conference (CGNCC)*, (2014).

[144] M.J.D. Hayes, M.L. Husty, P.J. Zsombor-Murray, “Singular Configurations of Wrist-Partitioned 6R Serial Robots a Geometric Perspective for Users”, *Transactions of the Canadian Society for Mechanical Engineering*, 26 (2002) 41-55.

[145] J. Angeles, “Fundamentals of Robotic Mechanical Systems: Theory, Methods, and Algorithms”, *Springer-Verlag,* (1997).

[146] L. Sciavicco, B. Sciliano, “Modeling and Control of Robot Manipulators”, *Springer-Verlag*, (2000).

[147] T.T. Shu, S. Gharaaty, W.F. Xie, “Dynamic path tracking of industrial robots with high accuracy by visual servoing”, *Journal of Latex,* 14 (2016).

[148] J.S. Yuan, “A general photogrammetric method for determining object position and orientation”, *IEEE Transactions on Robotics and Automation*, 5 (1989) 129-142.

[149] D. Sun, J. Mills, “Adaptive synchronized control for coordination of multi-robot assembly tasks”, *IEEE Transactions on Robotics and Automation*, 18 (2002) 498-510.

[150] X.P. Wang, L.L. An, L.Y. Zhang, L.S. Zhou, “Uniform coverage of fibres over open-contoured freeform structure based on arc-length parameter”, *Chin. J. Aeronaut.,* 21 (2008) 571-577.

[151] L. Yan, Z.C. Chen, Y.Y. Shi, R. Mo, “An accurate approach to roller path generation for robotic fibre placement of free-form surface composites”, *Robot. Comput.-Integr. Manuf.*, 30 (2014) 277–286.

[152] E. Lemaire, S. Zein, M. Bruyneel, “Optimization of composite structures with curved fiber trajectories”, *Compos. Struct*., 131 (2015) 895–904.

[153] R. Olmedo, Z. Gurdal, “Buckling response of laminates with spatially varying fiber orientations”, *Collection of Technical Papers - AIAA/ASME Structures, Structural Dynamics and Materials Conference*, 4 (1993) 2261-2269.

[154] C. Hély, L. Birglen, W.F. Xie, “Feasibility study of robotic fibre placement on intersecting multi-axial revolution surfaces”, *Robotics and Computer-Integrated Manufacturing*, 48 (2017) 73-79.

[155] H. Khakpour, L. Birglen, S.A. Tahan, “Uniform scanning path generation for abrasive waterjet polishing of free-form surfaces modeled by triangulated meshes”, *Int. J. Adv. Manuf. Technol.,* 77 (2015) 1167–1176.

[156] A.W. Blom, “Structural performance of fiber-placed, variable-stiffness composite conical and cylindrical shells”, *Delft University of Technology,* (2010).

[157] J. Kiefer, “Sequential minimax search for a maximum”, *Proc. Am. Math. Soc.,* 4 (1953) 502-506.

[158] E.S. Tzafestas, “Agentifying the process: task-based or robot-based decomposition?” *Proceedings of the IEEE International Conference on Systems, Man and Cybernetics. Humans, Information and Technology,* 1 (1994) 582-587.

[159] “FANUC Robotics SYSTEM R-30iB HandlingTool Setup and Operations Manual”, *Fanuc*. 1686-1692.

[160] “FANUC Robot series R-30iB CONTROLLER Dynamic Path Modification User’s Guide”, Fanuc, Version 8.30.

APPENDIX A

Mechanical Drawing – Chuck Bracket

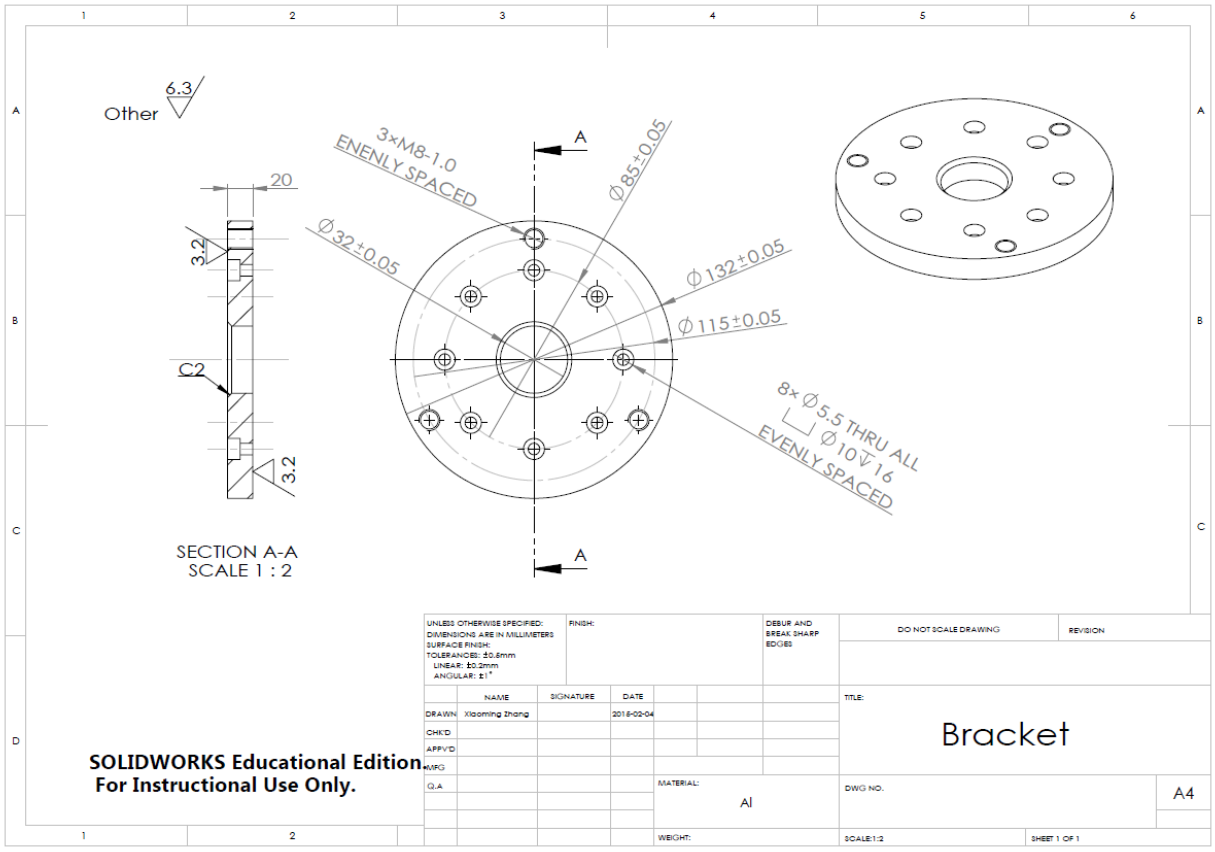

APPENDIX B

Mechanical Drawing – Stage Bracket

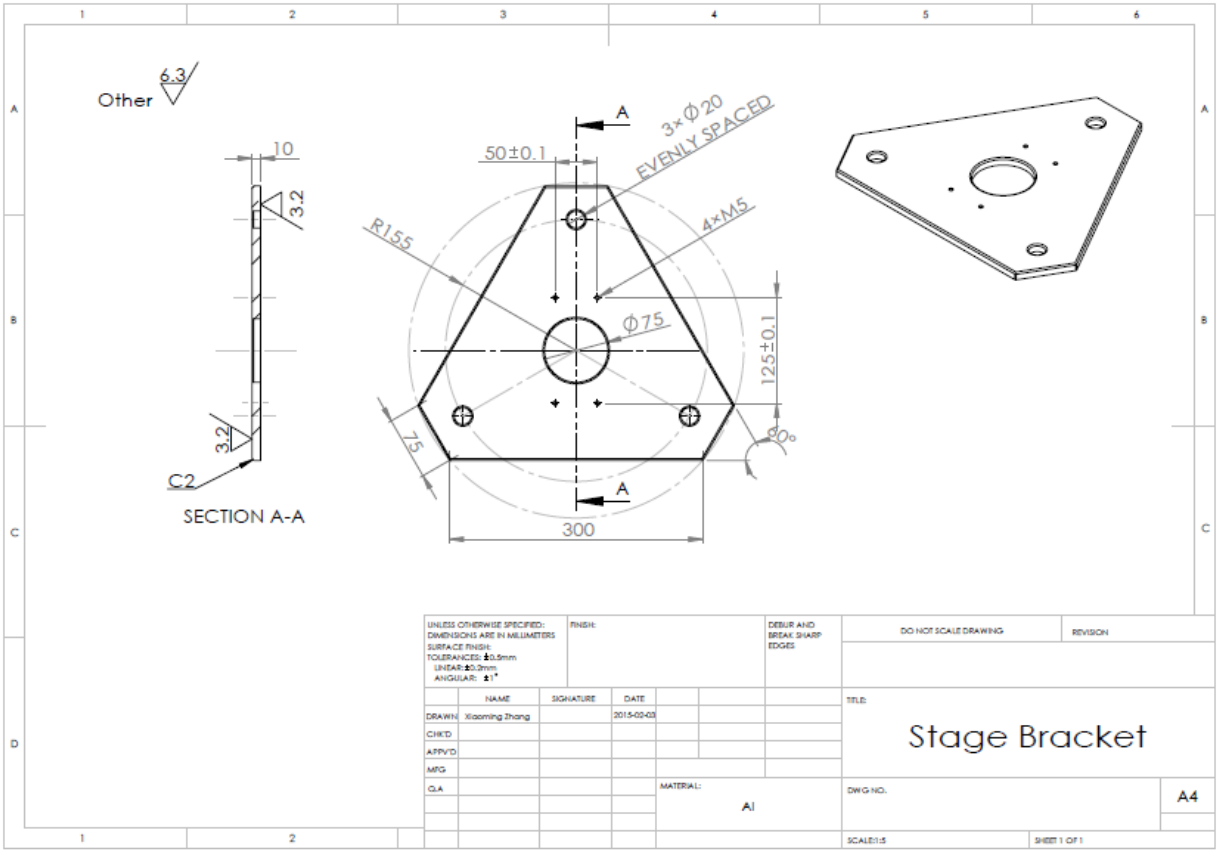

APPENDIX C

Mechanical Drawing – Valve Connector

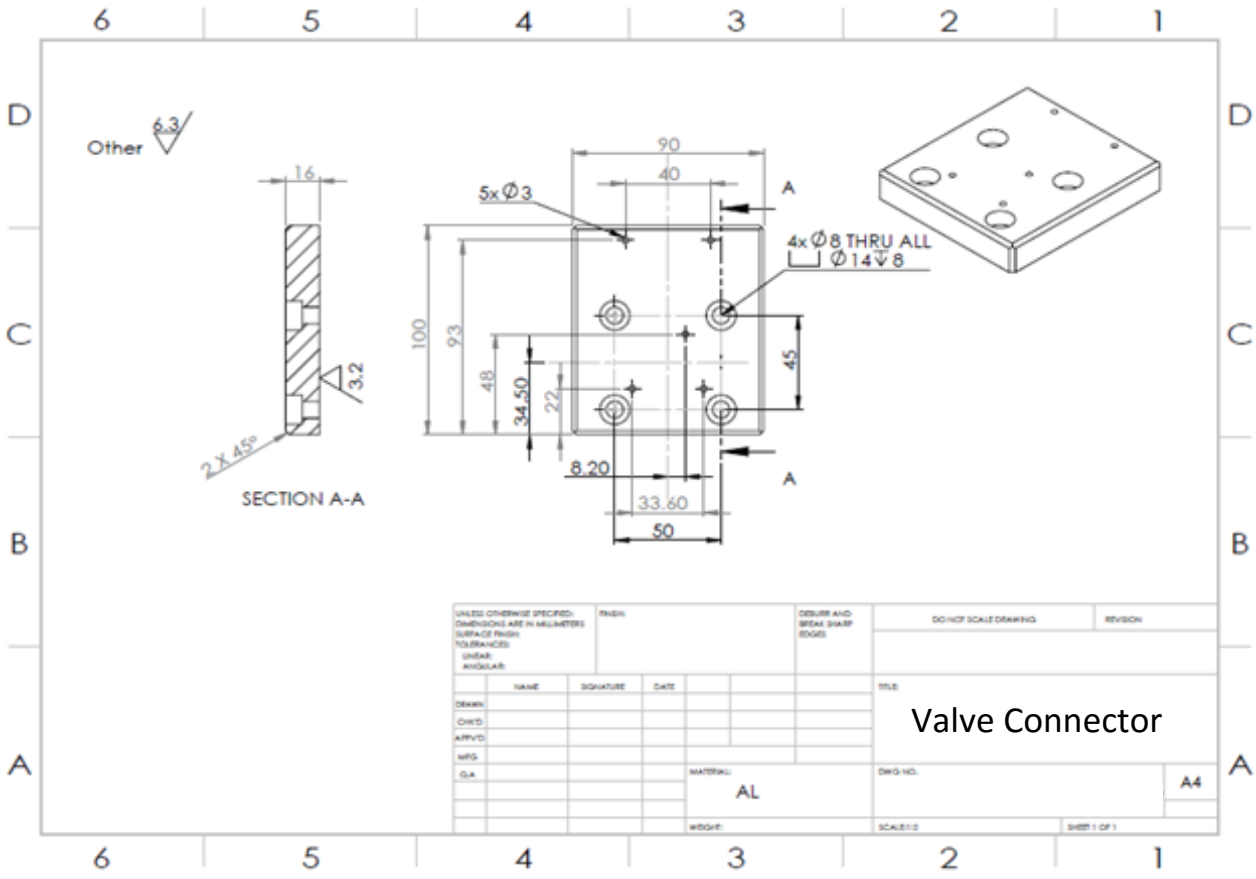

APPENDIX D

Mechanical Drawing – AFP Head

D.1. AFP Head Assembly

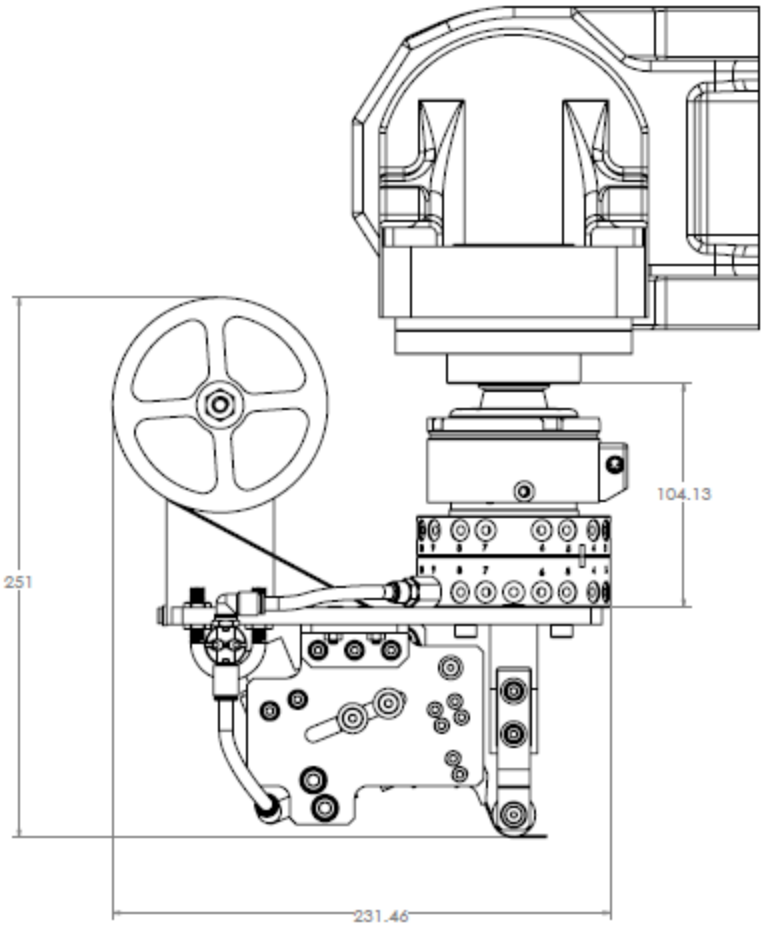

Appendix D

Mechanical Drawing – AFP Head

D.2. Servo Support

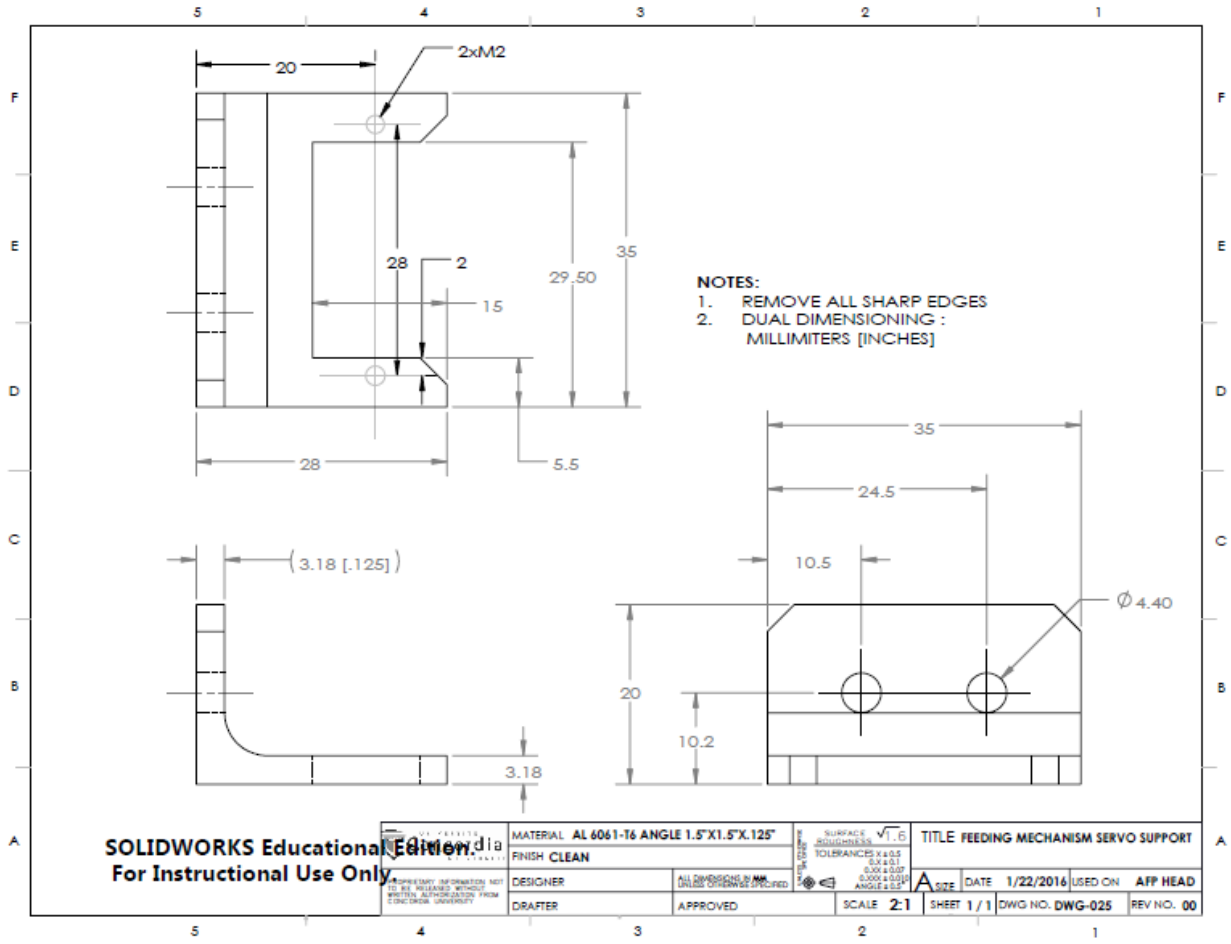

Appendix D

Mechanical Drawing – AFP Head

D.3. Feeding Mechanism - Servo Bracket

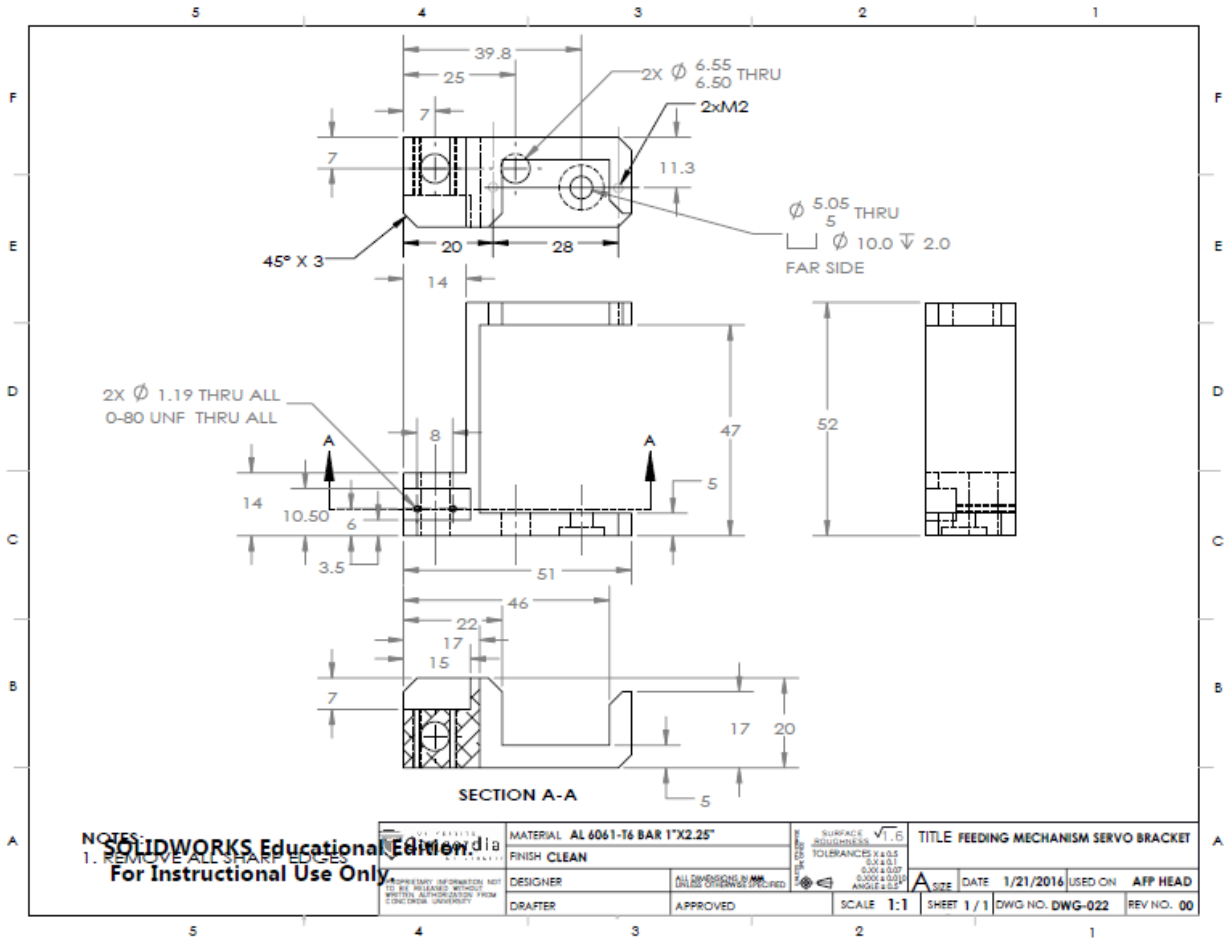

Appendix D

Mechanical Drawing – AFP Head

D.4. Fiber Dispenser

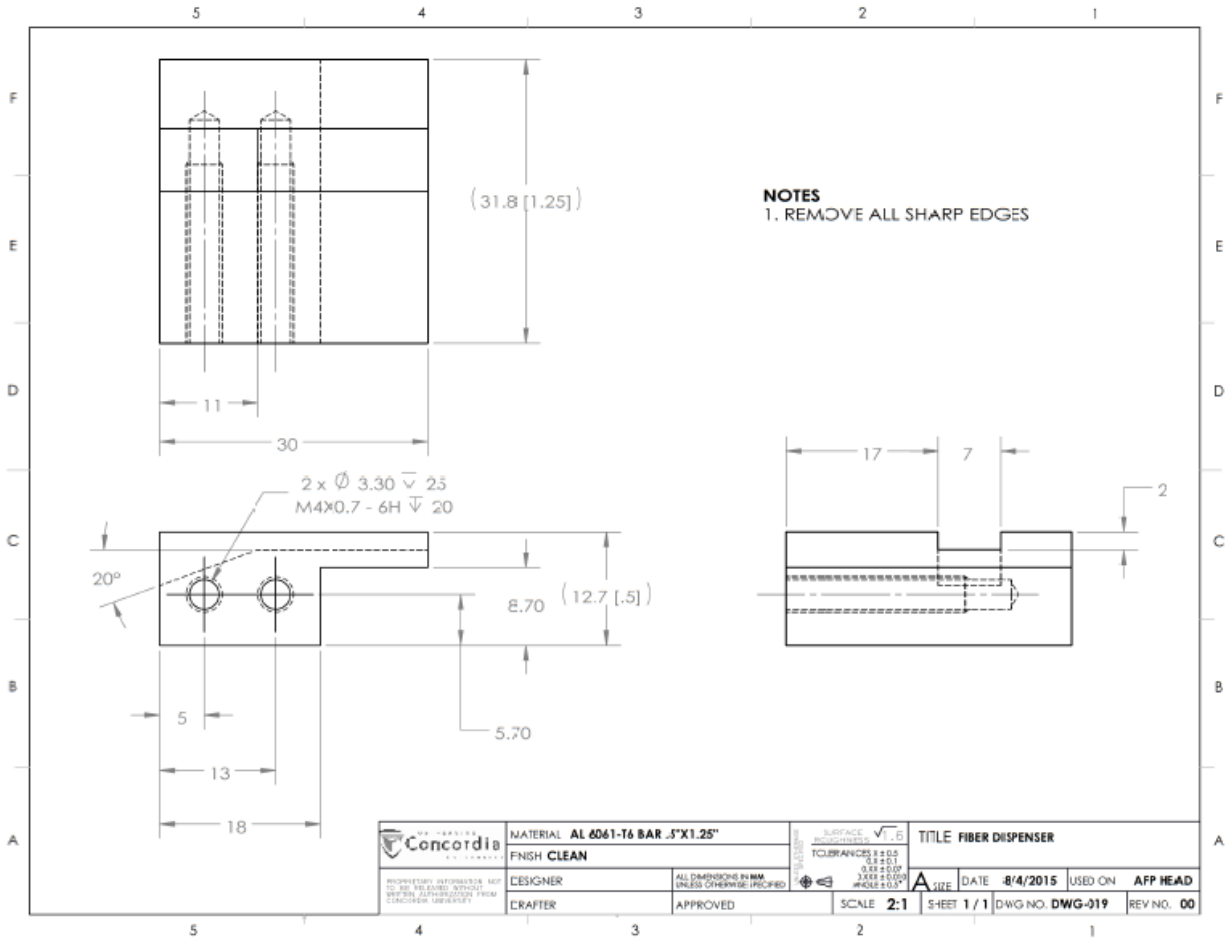

Appendix D

Mechanical Drawing – AFP Head

D.5. Cutting Blade and Pneumatic Actuator Coupler

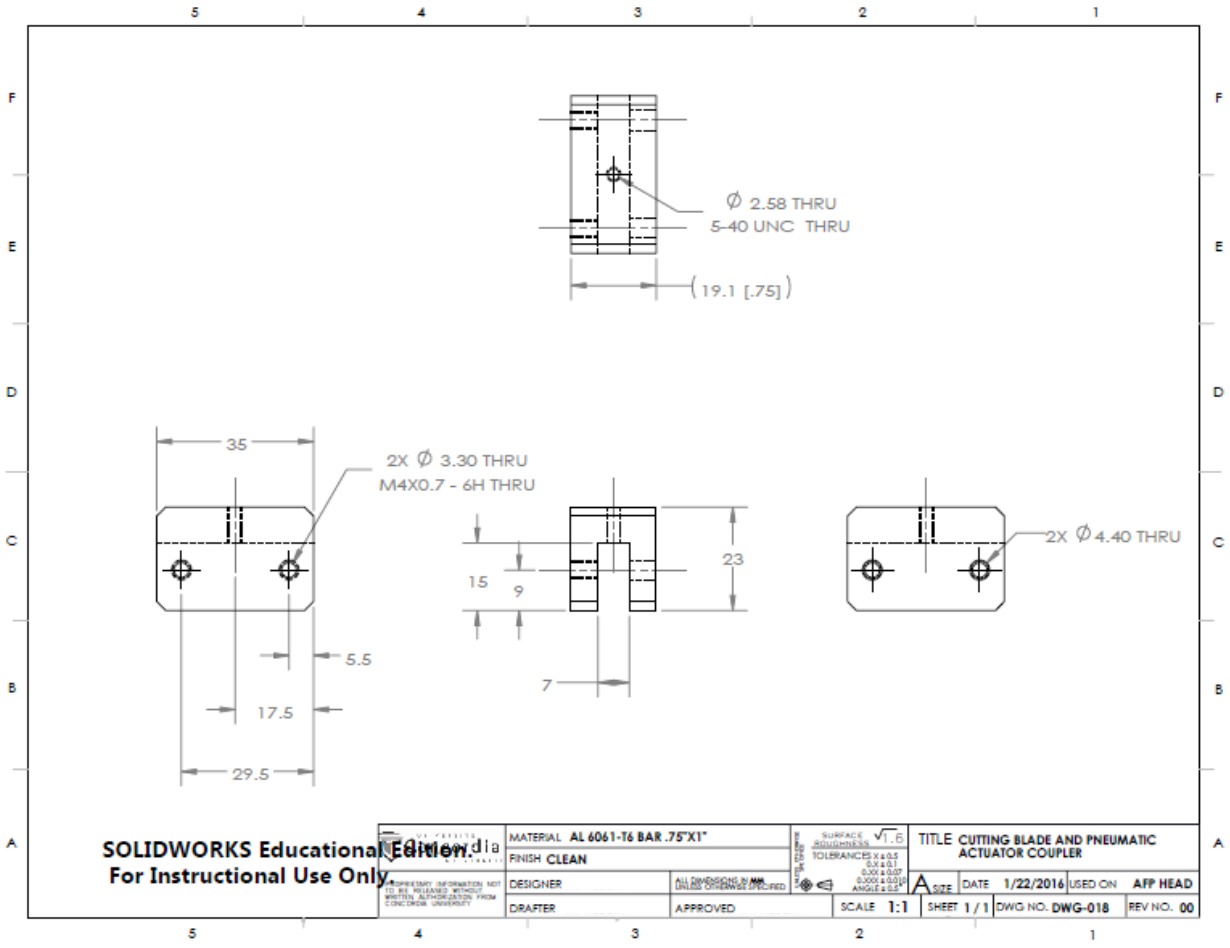

Appendix D

Mechanical Drawing – AFP Head

D.6. Cutting Blade Support

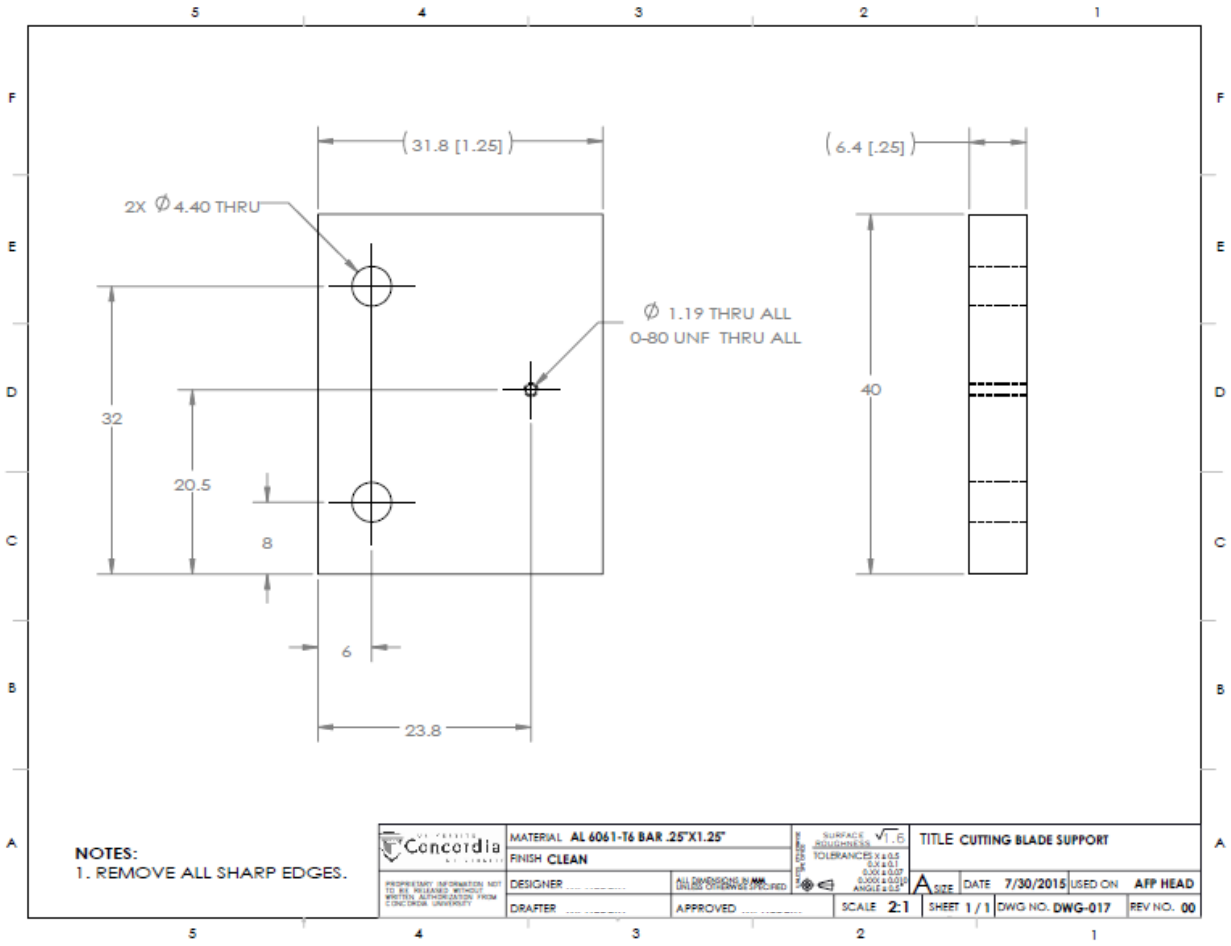

Appendix D

Mechanical Drawing – AFP Head

D.7. Linear Fiber Alignment

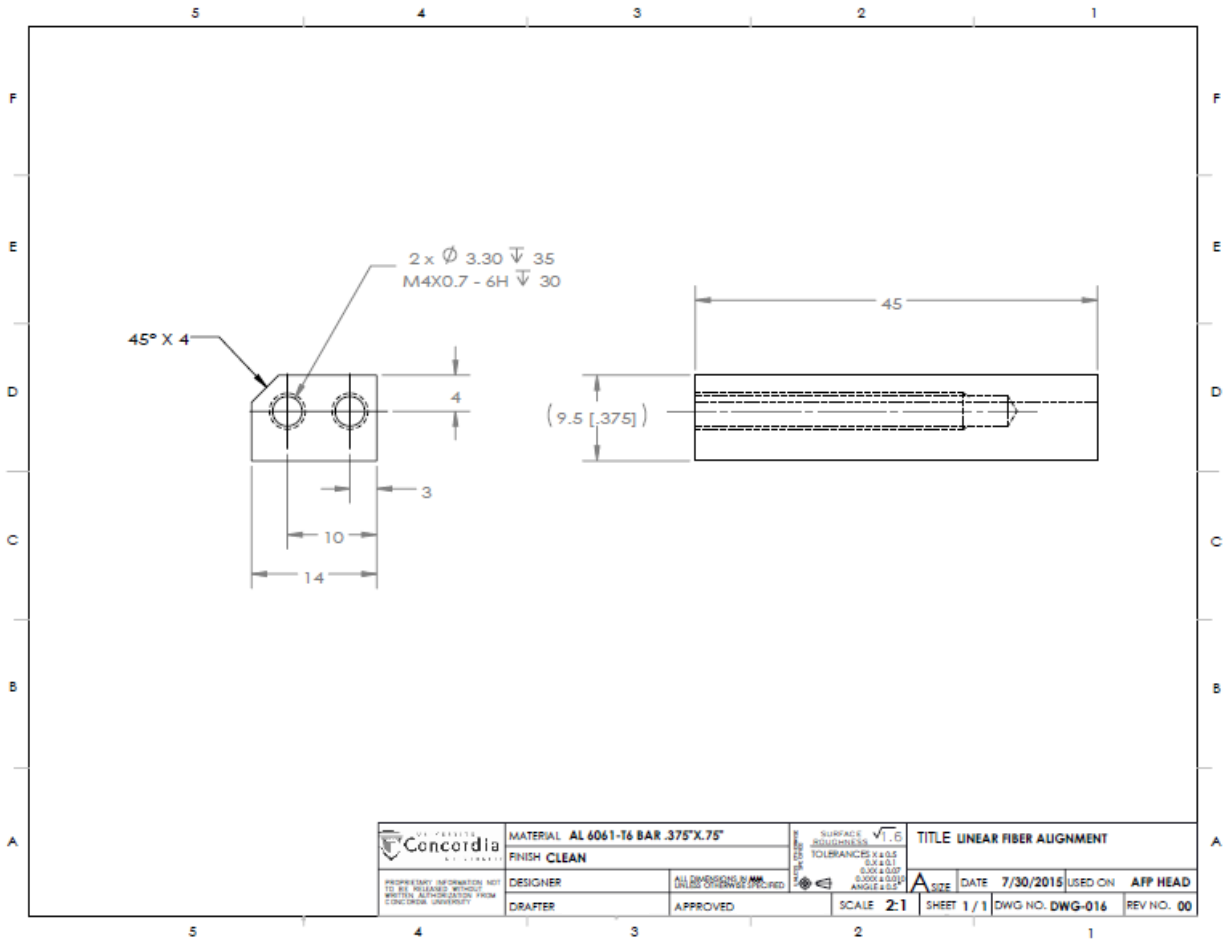

Appendix D

Mechanical Drawing – AFP Head

D.8. Stationary Blade Holder

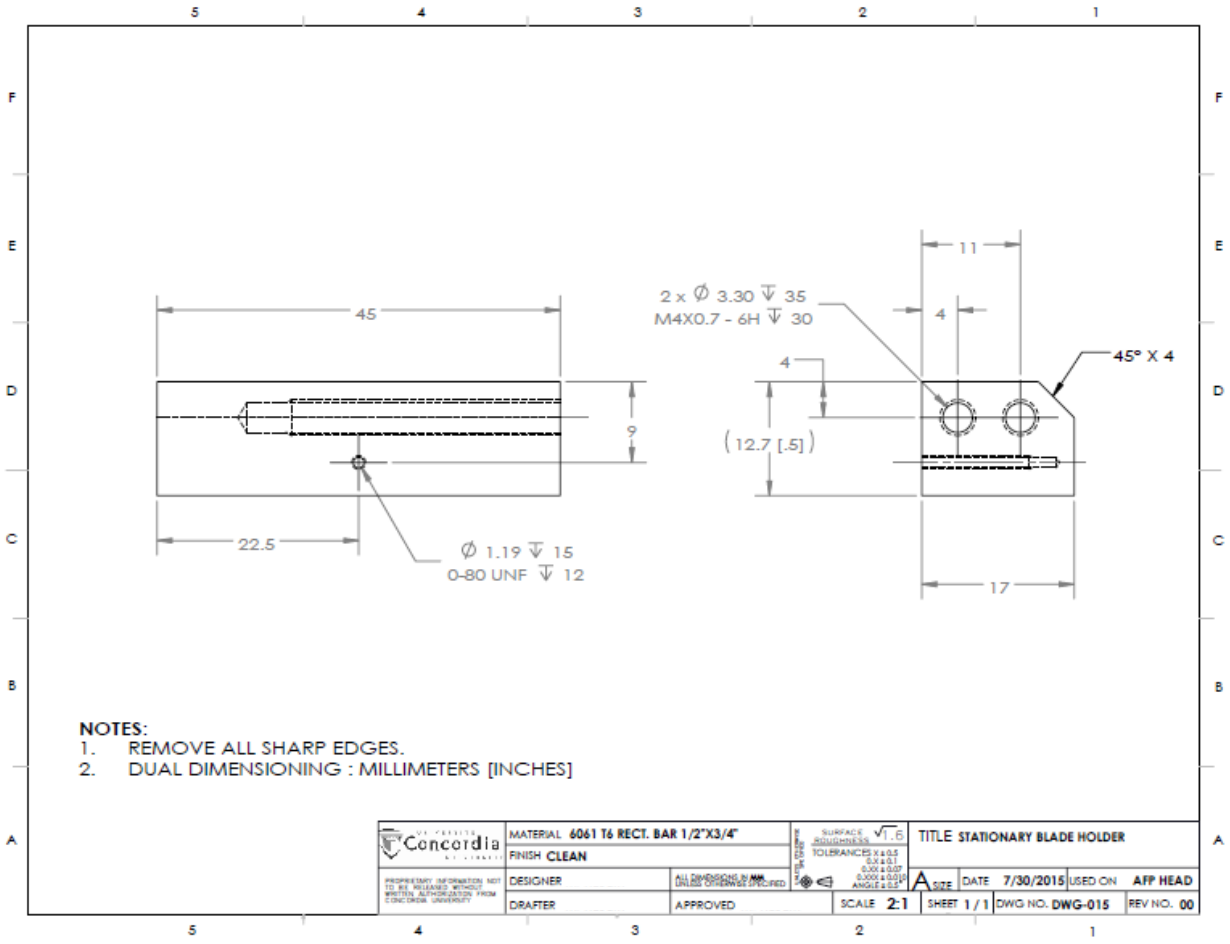

Appendix D

Mechanical Drawing – AFP Head

D.9. Side Plate

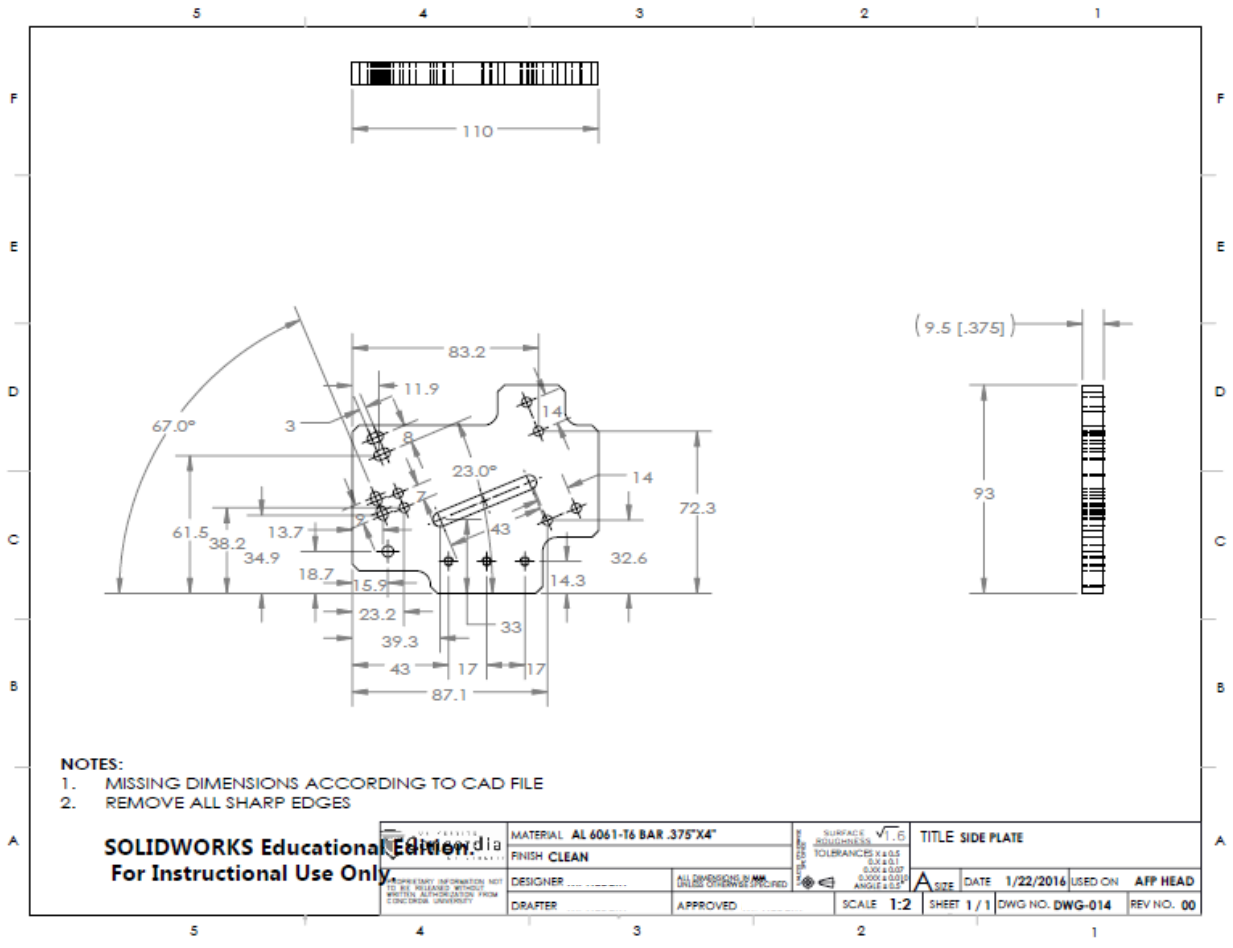

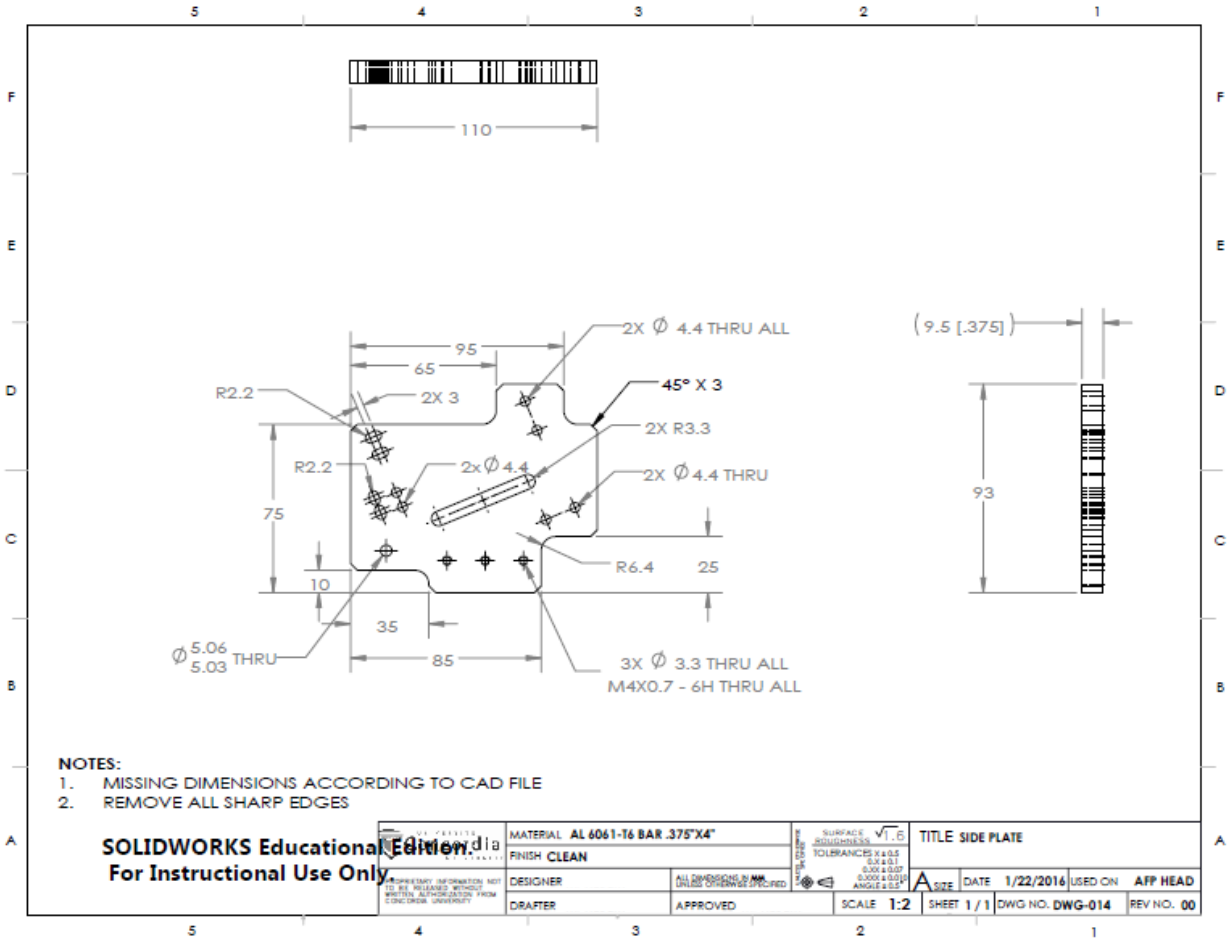
110
95
65
R2.2
2X 3
2X Ø 4.4 THRU ALL
45° X 3
2X R3.3
R2.2
2x Ø 4.4
2X Ø 4.4 THRU
75
R6.4
25
10
35
Ø 5.06 / 5.03 THRU
85
3X Ø 3.3 THRU ALL
M4X0.7 - 6H THRU ALL
(9.5 [.375])
93
NOTES:
1. MISSING DIMENSIONS ACCORDING TO CAD FILE
2. REMOVE ALL SHARP EDGES
SOLIDWORKS Educational Edition.
For Instructional Use Only
MATERIAL AL 6061-T6 BAR .375"X4"
FINISH CLEAN
DESIGNER
DRAFTER
APPROVED
SCALE 1:2
TITLE SIDE PLATE
DATE 1/22/2016
USED ON AFP HEAD
SHEET 1 / 1
DWG NO. DWG-014
REV NO. 00

Appendix D

Mechanical Drawing – AFP Head

D.10. Attachment Plate

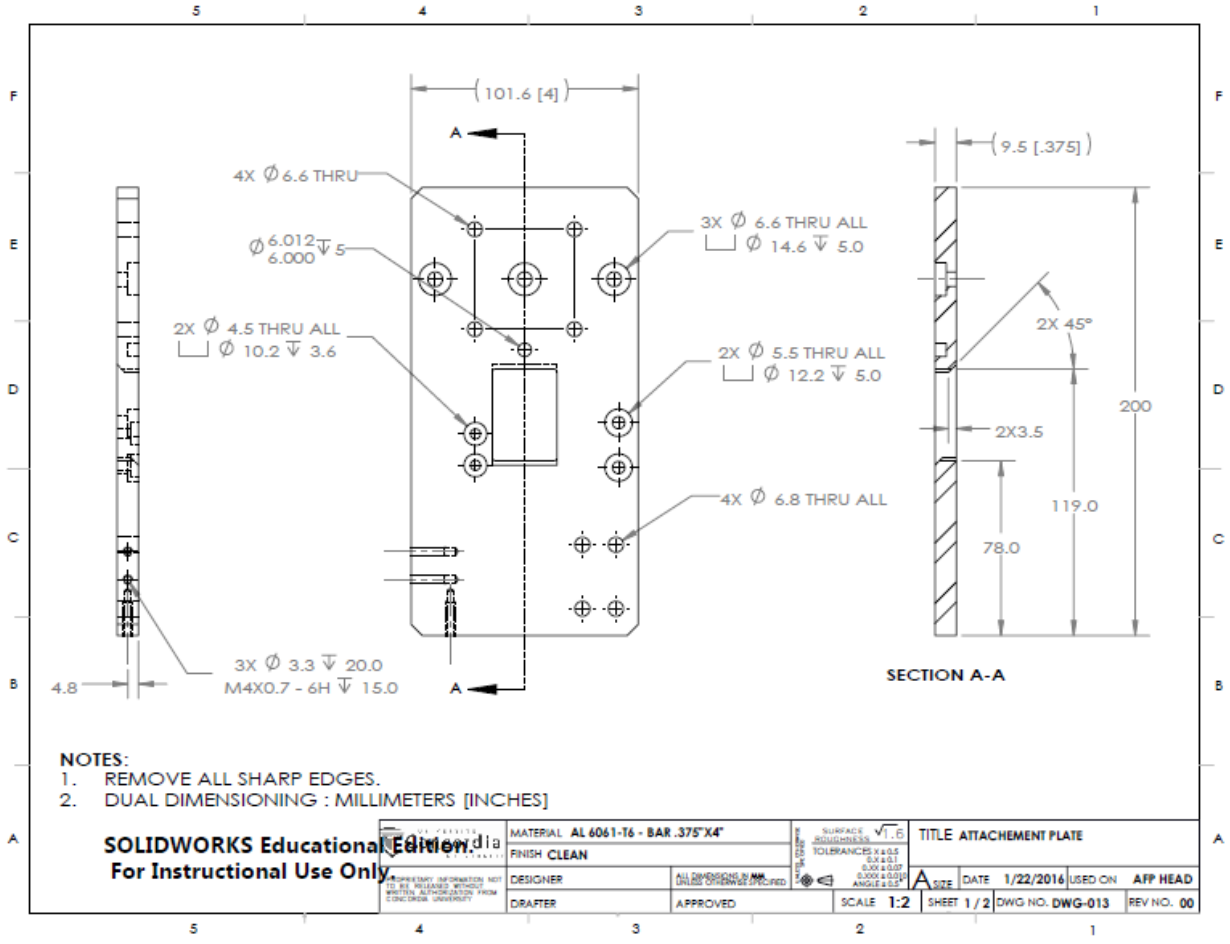

Appendix D

Mechanical Drawing – AFP Head

D.11. Alignment Roller Holder

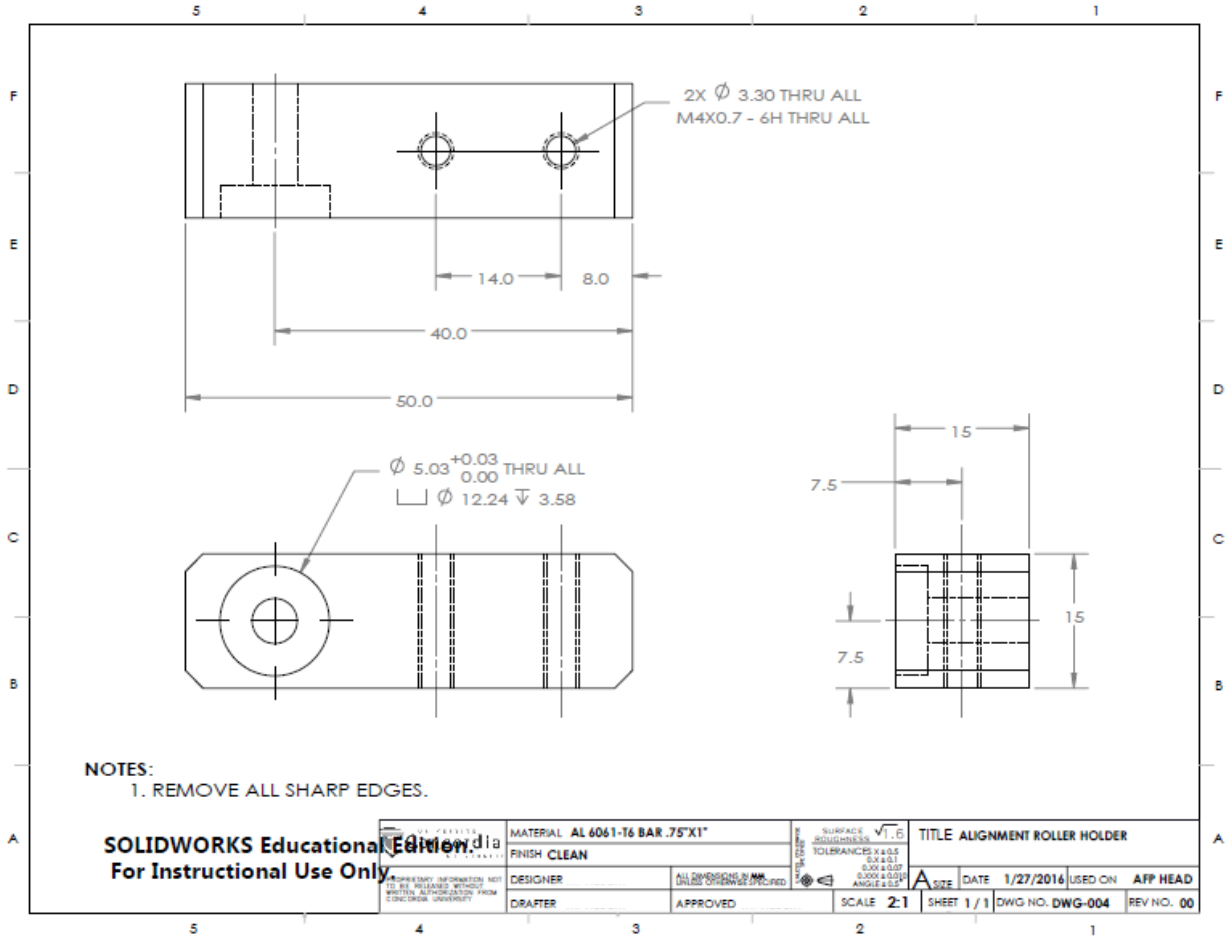

Appendix D

Mechanical Drawing – AFP Head

D.12. Compression Roller Bracket